Sigurd Wenner

Transmission Electron Microscopy and Muon Spin Relaxation Studies of Precipitation in Al-Mg-Si Alloys

Thesis for the degree of Philosophiae Doctor

Trondheim, January 2014

Norwegian University of Science and Technology
Faculty of Natural Sciences and Technology
Department of Physics

NTNU – Trondheim
Norwegian University of
Science and Technology

Abstract

The Al–Mg–Si system is a heat-treatable class of aluminium alloys that gain their mechanical strength via precipitation hardening. The main hardening phases are precipitated as needle-shaped nano-sized particles from a solid solution of Mg, Si and other added elements. Transmission electron microscopy and muon spin relaxation was used to study precipitation and clustering in Al–Mg–Si alloys, varying the heat treatment and chemical composition in order to understand the kinetics of precipitation and the morphology, distribution, and atomic structure of hardening precipitates.

Muons were found to form bonds with vacancies, atoms in solid solution, and clusters of solute atoms, which are the defects we can gain information from by applying muon spin relaxation to Al alloys. In binary Al–Mg and Al–Si alloys, we discovered very different vacancy behaviours after cooling from high temperatures: Si–vacancy clusters are quickly formed at room temperature in Al–Si, while Al–Mg keeps a much higher vacancy content than pure Al and Al–Si despite a lack of solute clustering. A high muon trapping in a specific temperature range was found in a 1.6% Mg_2Si alloy annealed for 16 hours at 70–150 °C. These conditions contain clusters and Guinier–Preston-zones preceding the main hardening phase β'' in the precipitation sequence. Density functional theory calculations support that the relevant muon trapping site is vacancies inside these structures, suggesting that the structures are stabilised by absorbing vacancies during annealing.

The roles of the elements Cu and Ca on precipitation during artificial ageing were investigated. Room temperature storage gives a negative effect on the strength of aged high-solute Al–Mg–Si alloys, in particular when the Mg/Si ratio is high. The negative effect was found to be diminished and delayed by adding 0.14 at.% Cu to alloys with Mg+Si = 1.3 at.%, in addition to giving an overall strength increase. Transmission electron microscopy investigations revealed that the fraction of Cu-containing precipitates increased with room temperature storage before ageing. The Cu addition is believed to help the formation of clusters that can act as nucleation sites for hardening precipitates and/or prevent the formation of clusters that can not. Various amounts of Ca was added to an alloy with 0.53% Mg and 0.40% Si. The Ca accumulated in large particles with composition $CaAl_2Si_2$, as determined by X-ray energy dispersive spectroscopy. The presence of Si in the particles causes a reduction of the available Si for precipitation and an increase in the effective Mg/Si ratio. The result is a coarser microstructure with a higher fraction of over-aged precipitates and a lower mechanical strength.

Aberration-corrected scanning transmission electron microscopy coupled with electron energy loss spectroscopy was conducted on an over-aged Al–Mg–Si–Cu–Ag alloy. The microstructure consisted of mostly disordered L and Q′ precipitates. After applying principle component analysis to the acquired spectrum images, atomic columns containing Cu and Ag could be clearly distinguished. Cu and Ag were seen to prefer different atomic configurations, and were not observed occupying the same columns. While Cu columns mostly resided in ordered parts of precipitates and along precipitate–matrix interfaces, Ag was diluted in several nearby columns in disordered parts, and at precipitate–matrix interfaces of high misfit.

Figure 1: Word cloud of all text in this thesis.

Preface

This thesis is submitted in partial fulfilment of the requirements for the degree of philosophiae doctor (Ph.D.) at the Norwegian University of Science and Technology (NTNU). The work has been carried out at the Department of Physics in collaboration with the TEM Gemini Centre from 2010 through 2013. The original project title was "Vacancies in aluminium alloys in a context of trace elements and recycling", in the Norwegian–Japanese Al–Mg–Si Alloy Precipitation Project. Apart from facilities at NTNU, experimental results published in this thesis were obtained at the RIKEN-RAL muon facility in Oxfordshire, UK and the SuperSTEM facility in Daresbury, UK.

This thesis is divided into three parts. Part I introduces the reader to aluminium alloys, with an emphasis on Al–Mg–Si alloys, and presents the experimental methods and data analysis used to obtain all results in the included papers. Part II contains a collection of papers which represent the scientific contributions of the Ph.D. project. Part III summarizes and discusses the results of the papers and provides an outlook of possible continuations to the studies.

Papers included in this thesis

- Paper 1: S. Wenner, R. Holmestad, K. Matsuda, K. Nishimura, T. Matsuzaki, D. Tomono, F. L. Pratt and C. D. Marioara, "Probing defects in Al–Mg–Si alloys using muon spin relaxation", *Phys. Rev. B.* **86** 104201 (2012).

- Paper 2: S. Wenner, K. Nishimura, K. Matsuda, T. Matsuzaki, D. Tomono, F. L. Pratt, C. D. Marioara and R. Holmestad, "Muon kinetics in heat treated Al(–Mg)(–Si) alloys", *Acta mater.* **61** 6082–6092 (2013).

- Paper 3: S. Wenner, C. D. Marioara, S. J. Andersen and R. Holmestad, "Effect of room temperature storage time on precipitation in Al–Mg–Si(–Cu) alloys with different Mg/Si ratios", *Int. J. Mater. Res.* **103**, 948–954 (2012). Figure 3(f) in this paper was chosen as the cover image of the journal issue.

- Paper 4: S. Wenner, C. D. Marioara , S. J. Andersen and R. Holmestad, "How calcium prevents precipitation hardening in Al–Mg–Si alloys", *Mater. Sci. Eng. A* **575**, 241–247 (2013).

- Paper 5: S. Wenner, C. D. Marioara, Q. M. Ramasse, D.-M. Kepaptso-glou, F. S. Hage and R. Holmestad, "Aberration-corrected STEM–

EELS studies of precipitates in an Al–Mg–Si–Cu–Ag alloy", *Scripta Materialia* (in press).

For papers 1 and 2, K. Matsuda and K. Nishimura supplied and prepared the material, T. Matsuzaki, D. Tomono and F. L. Pratt operated the µSR spectrometer and did preliminary analysis, while the majority of the analysis and the simulations were performed by myself. C. D. Marioara obtained some of the TEM results in papers 3 and 4, and Q. M. Ramasse, D.-M. Kepaptsoglou and F. S. Hage obtained all the TEM results in paper 5. All TEM specimen preparation, data analysis and most of the BF–TEM and SEM imaging were done by myself. The remaining co-authors have supervised my work and contributed to writing the paper manuscripts.

Contributions to other publications

- S. Wenner, K. Matsuda, K. Nishimura, J. Banhart, T. Matsuzaki, D. Tomono, F. L. Pratt, M. Liu, Y. Yan, C. D. Marioara and R. Holmestad, "Muon spin relaxation and positron annihilation spectroscopy studies of natural aging in Al–Mg–Si alloys", *Proceedings of the 13th International Conference on Aluminium Alloys (ICAA13)*, edited by W. Heiland, A. D. Rollett, and W. Cassada, 37–42 (Wiley, 2012).

- F. J. H. Ehlers, S. Wenner, S. J. Andersen, C. D. Marioara and R. Holmestad, "The role of the Si network to the stabilization of hardening precipitates in the Al–Mg–Si(–Cu) alloy system", *Proceedings of the 13th International Conference on Aluminium Alloys (ICAA13)*, edited by W. Heiland, A. D. Rollett, and W. Cassada, 279–284 (Wiley, 2012).

- S. Wenner, K. Matsuda, K. Nishimura, T. Matsuzaki, D. Tomono, F. L. Pratt, C. D. Marioara and R. Holmestad, "µSR experiments on Al–Mg–Si alloys", *RIKEN Accelerator Progress Report* **46** (in press). 1-page summary of paper 1.

- F. J. H. Ehlers, S. Wenner, S. J. Andersen, C. D. Marioara and R. Holmestad, "Phase stabilization principle and precipitate-host lattice influences for Al–Mg–Si–Cu alloy precipitates", submitted to *Acta Materialia*.

- T. Saito, S. Wenner, E. Osmundsen, C. D. Marioara, S. J. Andersen, J. Røyset, W. Lefebvre and R. Holmestad, "The effect of Zn on precipitation in Al-Mg-Si alloys", submitted to *Philosophical Magazine*.

Presentations

- "Computing for stronger aluminium alloys", talk at Fysikermøtet, Oslo, Norway, 20–22.06.2011.

- "The Role of Copper in Clustering and Precipitation in Al–Mg–Si–Cu Alloys", talk at the European Conference on Aluminium Alloys (ECAA2011), Bremen, Germany, 05–07.10.2011.

- "Muon spin relaxation and positron annihilation spectroscopy studies of solute clustering in Al–Mg–Si alloys", talk at the 13th International Conference on Aluminium Alloys (ICAA13), Pittsburgh, USA, 03–07.06.2012.

- "Muon spin relaxation and positron annihilation spectroscopy studies of solute clustering in Al–Mg–Si alloys", poster at the 7th International Conference on the Physical Properties and Application of Advanced MATerials (ICPMAT2012), Trondheim, Norway, 17–20.06.2012.

- "Precipitation in Al–Mg–Si alloys with Ca additions", poster at the International Conference on Processing & Manufacturing of Advanced Materials (THERMEC2013), Las Vegas, USA, 02–06.12.2013.

Acknowledgements

List of common abbreviations

AA	Artificial ageing
APT	Atom-probe tomography
BF	Bright-field (TEM)
CBED	Convergent-beam electron diffraction
DFT	Density functional theory
DSC	Differential scanning calorimetry
EDS	Energy-dispersive (X-ray) spectroscopy
EELS	Electron energy loss spectroscopy
fcc	Face-centered cubic
FEG	Field emission gun
GP	Guinier–Preston (-zone)
HAADF	High angle annular dark-field
KT	Kubo–Toyabe (function)
µSR	Muon spin relaxation
NA	Natural ageing
NBD	Nanobeam diffraction
PA(L)S	Positron annihilation (lifetime) spectroscopy
PCA	Principal component analysis
RT	Room temperature
TEM	Transmission electron microscopy
SHT	Solution heat treatment
SEM	Scanning electron microscopy
STEM	Scanning transmission electron microscopy
SSSS	Supersaturated solid solution
XRD	X-ray diffraction

Contents

II   Papers

III   Concluding remarks

Part I

Introduction

Chapter 1

Motivation

Aluminium is the third most important export product of Norway, after crude oil and fish. The reason is the availability of cheap energy, which is required in huge amounts for electrolysis of pure aluminium from bauxite. The troublesome refining process also explains why aluminium is a young material. Not before the start of the last century, aluminium started to come into wide use as a structural material. Since then, it has reached the position of being the second most used metal in the world, with only steel beating it to the throne [1]. Although aluminium is not good for making everything, using it instead of steel has several advantages in many cases: low weight (and high strength-to-weight ratio), good formability and machinability, excellent corrosion resistance, high thermal and electrical conductivity, and infinite recyclability are some of them.

Of special interest are Al–Mg–Si (or $6xxx$) alloys, being the alloys of choice for medium-strength architectural and transportation applications, most prominently in the automotive industry [2, 3]. The purpose of adding the two main alloying elements Mg and Si in small amounts ($\approx 1\%$) is to form hardening *precipitates*, which typically contribute with a fivefold strength increase from pure aluminium. Understanding the process of precipitation and how it affects mechanical properties have been important subjects of research for a hundred years [4]. Only in the last decades have we begun to understand the structure and formation of the different phases during heat treatment. There is a handful of discovered metastable phases in the Al–Mg–Si system alone. The number of possible phases increases when other elements are brought into the mixture, for example Ge, Cu, and Ag. Varying the chemical composition of an alloy and parameters of the heat treatment (heating/cooling rates, times and temperatures) gives a lot of room to play around, create different microstructures and observe what properties they

give the end product. We are nowhere near a complete understanding of any alloy system, and researchers in metallurgy and condensed matter science may be occupied another hundred years in answering questions (and finding new ones) about the optimisation of alloy properties.

The most important tool for structure determination of precipitate phases has without any doubt been the transmission electron microscope (TEM). Since electron microscopes were first developed in the 1930s, the resolution of this imaging technique has been increased beyond limits no-one thought were surpassable, several times. Today, aberration corrected microscopes are able to resolve all known precipitate structures in Al alloys (see e.g. [5–7]). Various TEM methods also enable compositional determination of the observed structures, with a spatial resolution approaching that of the microscope itself. These are used to make still better atomic models of all imaginable structures, motivating research groups for an arms race to obtain state-of-the-art microscopes, which are surpassed in performance few years after. New possibilities such as atomic resolution STEM–EELS mapping have yet to see applications in precipitate structure determination, which motivates parts of this thesis.

While TEM is an established technique in alloy science, there exists several condensed matter techniques that have not been tried out sufficiently for the purpose of investigating nano-precipitation. We found such a technique, muon spin relaxation (µSR), which had previously been shown to detect trace amounts of elements in aluminium [8, 9]. It is a spectroscopy technique, making it unable to produce beautiful images. Yet its working principle is built on an elegant exploitation of fundamental particle physics. Muons, elementary particles found naturally in cosmic radiation, are used to probe the smallest entities in materials science: atoms and the spaces in between them [10]. Industrial aluminium alloys have not been investigated using µSR before, although their intricate age hardening processes call for such a powerful method being tried out. We have therefore studied how the method can be applied to Al–Mg–Si alloys, with particular emphasis on detecting solute clusters, the nuclei of precipitate particles.

This thesis describes subprojects with slightly different approaches to understanding precipitation in Al–Mg–Si alloys. Some of them are metallurgical: investigating the effect of trace elements and heat treatment on precipitation and mechanical properties. Others are methodological: trying out techniques, determining what they can tell us and if relevant quantitative information can be found, and developing methods for data analysis. The common goal is to figure out the kinetics of precipitation and the structure of precipitates in Al–Mg–Si alloys, and how these can be controlled

and optimised to improve certain properties of the material, enabling the tailoring of alloy properties to specific applications by *alloy design*.

This first part of the thesis gives an introduction to the physical theory of aluminium alloys and in particular to precipitation in Al–Mg–Si alloys. It also includes a chapter about the experimental methods that were used, explaining them in general and providing methodologies for extracting information about precipitation, both during experiments and later data analysis. This serves as an introduction to the second part, which contains the five scientific papers I have published as a first author. Further, I created a third part to discuss some of the results while thinking of what insight future research may bring into the discussion.

Chapter 2

Aluminium and aluminium alloys

Aluminium as a pure substance was first produced in 1827 by the German chemist Friedrich Wöhler [11]. The metal has its name from a class of chemical compounds known as *alums*, which were and still are being used in water purification, medicine and even food. Aluminium is a paramagnetic metal with face-centered cubic (fcc) crystal structure[1]. Today, its uses are many, for instance automobile engines, soda cans (Fig. 2.1), window frames, foil and electrical cables in its pure and alloy forms. The element is also used as a reactant in many chemical processes for producing other substances. Solid aluminium has a density of 2.7 g/cm^3, which makes it as a light metal, a characteristic it shares with titanium and magnesium. Steel is three times denser, and have a similar strength-to-weight ratio (specific strength) to medium-strength aluminium alloys [14].

2.1   Modern production

Aluminium is the third most abundant element in the Earth's crust, after oxygen and silicon [15]. It is found mainly in bauxite rock in the form of aluminium oxide. After extracting the oxide from rocks, aluminium is reduced by electrolysis using a carbon anode, releasing carbon dioxide in the process. One may remove unwanted impurities, which are introduced primarily through the raw materials and during the electrolysis process. The pure aluminium melt is then alloyed with other elements, a selection of which is presented in the next section. For complex shapes such as car engines, alu-

---

[1]For elementary solid state physics references, see e.g. [12, 13].

Figure 2.1: My motivational aluminium can, from Hydro aluminium. Beverage cans are made using 3004 and 5182 alloys for the body and lid, respectively [14].

minium alloys are cast directly into its final shape. However, most products (85% [1]) come from *wrought* (synonym of worked) aluminium alloys, which implies casting to billets and forming them to their final shape under an elevated temperature. This has many advantages, including producing a more homogenous microstructure and a finer grain structure. Wrought alloys are most commonly either extruded or rolled. While rolling always produces plates/sheets, extruded profiles can have a multitude of complex shapes, decided by the shape of the extrusion die. In 2012, 1.2 million tonnes of primary aluminium was produced in Norway [16], and 45.9 million tonnes worldwide [17].

2.2   Types of alloys

Aluminium in its pure form is very weak, having a yield strength of 7–11 MPa [1]. It is also prone to oxidation. Although it may be counterintuitive, a way to improve the durability of any pure metal is to introduce defects into its crystal lattice. The commonly used alloying element atoms (or *solute atoms*) in Al alloys are all substitutional. The details of how solute atoms behave inside the Al host fcc lattice (henceforth called the *matrix*) are explained in more detail in later sections.

Table 2.1 shows the classes of wrought aluminium alloys, grouped by their main alloying elements. Four digits, such as 6082, specify an alloy composition range and upper tolerances for trace elements. All elements

Table 2.1: Wrought alloys in the international aluminium alloy designation system.

Alloy class	Main alloying elements	Heat-treatable?
$1xxx$	—	—
$2xxx$	Cu (Mg) (Li)	Yes
$3xxx$	Mn (Mg)	—
$4xxx$	Si	—
$5xxx$	Mg	—
$6xxx$	Mg, Si (Cu)	Yes
$7xxx$	Zn, Mg (Cu)	Yes
$8xxx$	Various	(Yes)

have different effects. Some are added for strength, some for corrosion resistance, ductility, grain refinement, etc. Certain elements are detrimental to one or more of these properties and should be avoided. Micro-alloying elements (not listed as main alloying elements) that have been added for some purpose in industrial alloys encompass about half the periodic table. An alloy is denoted heat-treatable if its mechanical strength improves significantly during heat treatment at temperatures well below the eutectic (melting) temperature. All main alloying elements listed have good solid solubilities (> 1 wt.%) in Al [14], which prevents them from forming stable phases at solution heat treatment (SHT) temperatures (see section 2.5).

2.3 Recycling

Secondary production of aluminium products from scrap metal constitutes a steadily growing fraction of the total industry. The excellent recyclability of aluminium arises from its low melting point. It requires merely a few percent of the electrolysis energy to remelt and recycle the material [14]. Aluminium is thus referred to as an "energy bank": one can put huge amounts of energy into primary production in order to save energy later. Consequently, 75% of all aluminium ever produced is still in use [14], in beverage cans, airplanes, cars, skyscrapers and so on.

As the alloy classes in Table 2.1 have quite different properties, sorting the scrap metal into roughly homogeneous compositions is important. The major alloy designations are usually created with a high tolerance in

compositional variation, so that their scrap metal, and whatever may come with them into the remelting plant, can be reused with the same designation. Still, some chemical elements are unwanted in even trace amounts, and many separation and composition adjustment procedures have been devised to account for this. Examples of coarse processes are delaquering, removal of rubber and wood and rotary furnaces that evaporate paint and plastic from the melt [14]. Some dissolved elements are reactive and can be removed by adding certain chemicals for them to form compounds [18, 19]. Solid particles that are heavier or lighter than molten aluminium settle at the top or bottom parts in a furnace, and are otherwise removed by filtration [18, 20, 21]. Hydrogen is removed by degassing, using argon bubbles to trap hydrogen gas and transport it out of the melt [22].

To find the tolerance limits of certain trace elements in an alloy, systematic investigations of alloys with the element of interest added in increasing amounts must be performed. This is the motivation for parts of this thesis and the funding body of a large part of the work.

2.4   Strength

When compared to pure Al, the most important feature of Al alloys is their mechanical strength. All nano-scale crystallographical defects relevant for
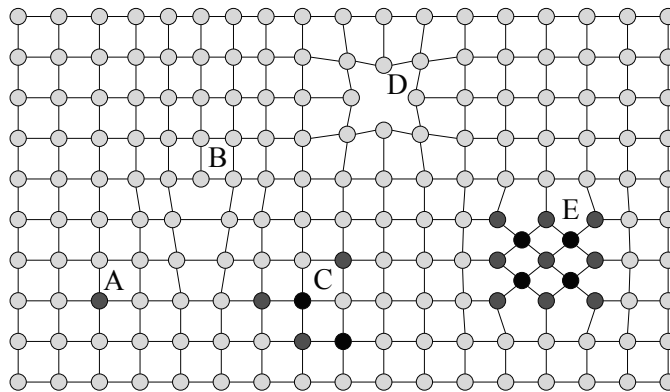

Figure 2.2: Lattice defects in a generic crystalline solid. A: Substitutional solute atom, B: Dislocation, C: Cluster of solute atoms, D: Vacancy, E: Precipitated phase.

hardening are shown in Fig. 2.2. The general theory of these defects can be found in the literature, e.g. [23, 24].

There are several possible measures of the mechanical strength of a ma-

terial. To understand these, one should look at a typical stress–strain curve (Fig. 2.3), which is measured experimentally by stretching a sample of a material and recording the value of the tensile stress (force per area) corresponding to the strain (relative elongation of the sample). The maximum stress required for the material to fracture into two parts is called the *ultimate strength*. A more interesting value is the *yield strength*, signifying the stress that takes the material from an elastic to a plastic deformation regime. Once a structural element has experienced a stress above the yield strength, the material is deformed and will not relax back to zero strain when relieved of its stress.
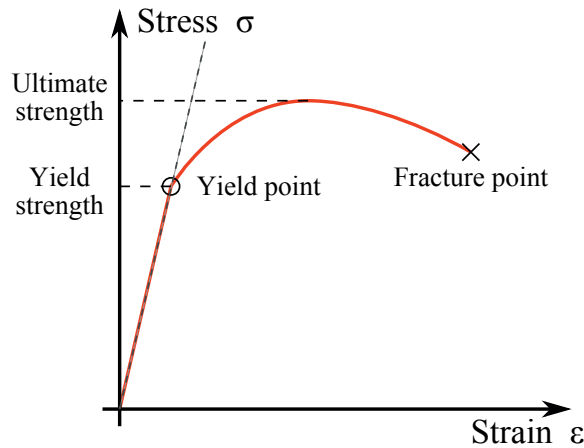
Figure 2.3: Stress–strain curve of a ductile material.

The chemical bonds between the atoms in a material are very strong, and fracture does not happen by breaking them off at some plane at the same time. Rather, stress-induced deformations and fracture happen via the motion of dislocations. In aluminium, {111} plane dislocations are the most common, and the most energetically favourable directions of movement are along ⟨110⟩ [25]. It is easiest to view a dislocation as a simple edge dislocation, that is, an inserted {111} plane, but the reality is more complicated than this, which can be seen on TEM images of complex dislocations curling about (see e.g. Fig. 2.4). Stress in a material lowers the energy barrier for dislocation movement and also creates new dislocations. Dislocations moving will gradually ensure the slip of lattice planes, which ultimately rips the material apart. For a pure monocrystalline material, fracture theory can therefore be reduced to understanding dislocations and the interactions between them [26].
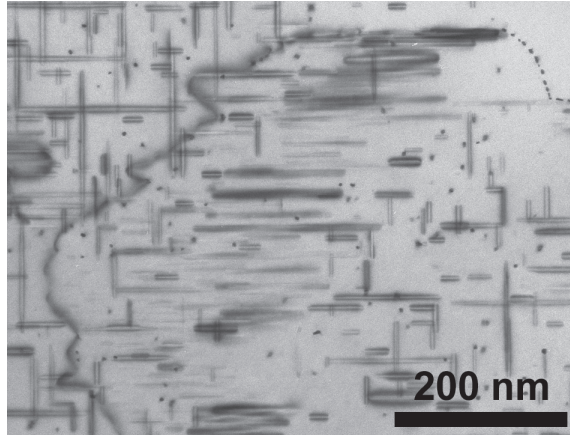
Figure 2.4: BF-TEM image of a complex dislocation (left side) among the precipitate microstructure of the LCa3 alloy in paper 4. The viewing direction is $\langle 001 \rangle_{Al}$.

After thermomechanical treatment, there are five main properties of the microstructure which contribute to the mechanical properties:

- Grain structure
- Dislocations
- Atoms in solid solution
- Solute clusters
- Precipitates

Pure aluminium has a yield strength of around 10 MPa [14]. Real-world materials are polycrystalline, so the most important reason for variations in this number is differing grain structure, as the grain size and texture depend on the casting method and post-casting treatment. Generally, a small grain size will give a slightly higher strength, as the increased grain boundary area prevents dislocation movement.

I do not want any parts of my bike to be deformed beyond reversibility, but plastic deformations were actually used to form parts of the aluminium frame when it was constructed. Paradoxically, dislocations introduced through deformation can slow each other down and cause *work hardening* through the effects of dislocation–dislocation interactions [26]. This contributes with $\sim$ 90 MPa to the total strength[2] for a 6060 alloy with

---

[2]Bear in mind that strength contributions from different defects are not necessarily additive

a 10% tensile deformation before ageing [27]. Atoms in solid solution give
an additional strength increase of ~ 30 MPa in the same alloy as they in-
duce a (very local) strain in the matrix [27]. Dispersoids are stable pre-
cipitates, incoherent and larger than the ones discussed below. They are
typically composed of Al, Fe, Mn and Si, which are all present in industrial
$6xxx$ alloys. Due to their incoherency, they do not improve the mechan-
ical properties much by themselves, but they restrict grain growth during
high-temperature treatments, resulting in a finer grain structure (see e.g.
[28]). Some elements, like Ti and B are added to create particles that help
to nucleate Al grains during solidification, so that fewer, smaller grains are
produced [29].

Nano-scale metastable precipitates, the topic of the rest of this chapter,
give a strength increase of 100-200 MPa in industrial $6xxx$ alloys [14]. These
precipitates are particles rich in Mg and Si, with a crystal structure different
from that of the Al matrix. They precipitate by diffusional phase transform-
ations during heat treatment. Like the other defects, precipitates prevent
fracture by preventing dislocations from moving. Dislocation–precipitate
interactions are complicated, and depend mainly on the morphology and
coherency of precipitates. The results of the interactions are commonly
split into two classifications, looping and shearing (shown in Fig. 2.5). The
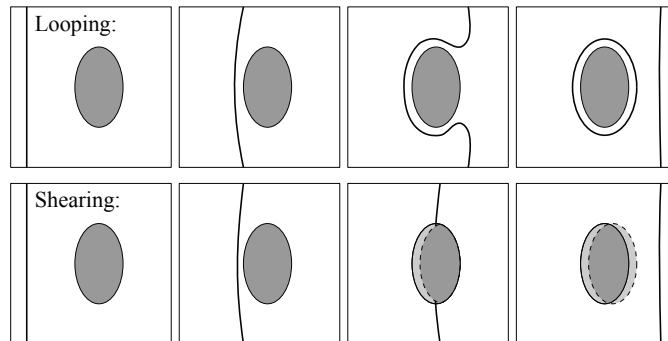
Figure 2.5: Cartoon depicting two modes of interaction between a moving disloca-
tion and a precipitate.

names describe the mechanisms well: looping leaves a closed dislocation loop
around the precipitate, while shearing cuts it in two parts, one of them dis-
placed a distance corresponding to the Burgers vector [12] of the dislocation.
Looping entails the splitting of a dislocation into two new ones. Shearing
requires a lot of energy since a dislocation must pass the precipitate–matrix
interface and manifest itself as a dislocation in the precipitate structure, and

happens predominately for larger, incoherent precipitates [30]. An alloy consisting of a high number density of small, shearable (coherent) precipitates is therefore the strongest.

As stated, a small grain size gives a small strength increase, but it can also reduce precipitation hardening: Solute elements and vacancies tend to diffuse toward grain boundaries during low-temperature ageing. As grain boundaries act as high-diffusivity paths for vacancies, the vacancies are annealed out of the material, leaving behind a film of solute elements along the grain boundary. The nearby material is then low in both solutes and vacancies, and precipitates are unable to form. A precipitate-free zone (PFZ) appears (see Fig. 3.8). This can also happen around large, stable particles, as observed in paper 4, Fig. 3(b).

2.5   The heat treatment and its effects

The positive effect of heat treatment on some aluminium alloys was discovered by Alfred Wilm in 1906 [31]. The first alloys used Mg and Cu as alloying elements, and relied on cluster hardening after room temperature storage [32]. Age hardening in general was later explained with the formation of microscopic precipitate phases by Merica *et al.* [33].
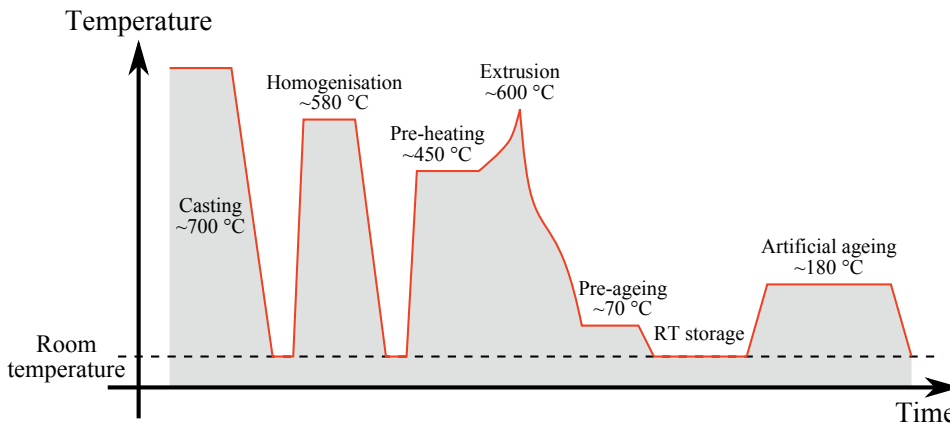
Figure 2.6: An example heat treatment for an extruded 6xxx alloy. For alloys with a scientific purpose, a solution heat treatment step with a strictly controlled temperature ($\approx 550\ ^\circ$C) is usually added after the extrusion step.

Figure 2.6 shows a generic industrial heat treatment of 6xxx alloys. The microstructure of the material will change all along the way, strongly affecting its properties. The first treatments are mainly for getting the material

into the right shape. Homogenisation and solution heat treatment (SHT) dissolves any structures rich in alloying elements, and distributes these uniformly in the matrix. Deformation introduces dislocations and artificial ageing enables precipitation.

After SHT, the material contains a high concentration of quenched-in vacancies. These are essential to the precipitation process as they enable substitutional diffusion. Vacancies diffuse about (indirectly, as it is atoms that jump into the vacancies), and tend to bind with solute atoms. This binding accelerates substitutional diffusion in the following manner: A solute atom and a vacancy can move together as a diffusion pair until they reach an area with a higher solute concentration. The vacancy may then disconnect and run off to fetch another solute atom. This is called the *vacancy pump mechanism* [24].

Some products are left in a T4 condition, meaning that they are quenched from SHT and naturally aged (see section 2.6.2) to a sufficient hardness. Industrial temper codes include T4, T6, T7, along with others including deformation and other treatments. T6 is the most desirable condition for most products. It involves bringing the material to its peak hardness through *artificial ageing* (AA) (sometimes called bake hardening) at temperatures of 150–200 °C. Pre-ageing at 70–100 °C is sometimes conducted to improve the precipitate nucleation in $6xxx$ and $7xxx$ alloys. Over-ageing to the T7 temper is done by simply continuing the AA until the material has decreased somewhat from its peak hardness. This may improve other desirable properties such as corrosion properties, electrical conductivity, thermal stability, and crash box performance in cars (see e.g. [34]).

2.6 Precipitation in Al–Mg–Si alloys

2.6.1 The precipitation sequence

The Al–Mg–Si(–Cu) alloy system has a large number of possible precipitate phases. The type of precipitates that form, their physical dimensions, and their dispersion in the matrix are heavily dependent on parameters such as alloy composition, storage time, ageing time/temperature, heating/cooling rates, and deformation before ageing. It has been found that precipitates form in a sequence: When increasing the artificial ageing time, the relative fractions of the different types of precipitates change. Each precipitate type has a preferred alloy composition and heat treatment required to maximise its presence. One is thus able to design a heat treatment procedure where a specific type of precipitate phase dominates.

Though the understanding of the sequence has been changing throughout the years, its most established form is [35–37]

$$\text{SSSS} \rightarrow \text{Clusters} \rightarrow \text{GP-zones} \rightarrow \beta'' \rightarrow \beta', \text{U1,U2,B}' \rightarrow \beta, \text{Si}. \qquad (2.1)$$

Since papers 3 and 5 deal with Cu-containing alloys, I also show the corresponding sequence for Al–Mg–Si alloys with significant amounts of Cu [38–40]:

$$\text{SSSS} \rightarrow \text{Clusters} \rightarrow \text{GP-zones} \rightarrow \beta'', \text{C,L} \rightarrow \text{Q}' \rightarrow \text{Q}. \qquad (2.2)$$
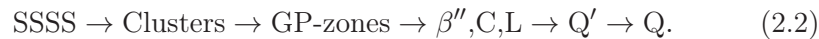
The phases shown here are the most commonly observed ones, but if the chemical composition is on the very Cu-rich side, one may find S and its precursors [41] from the Al–Mg–Cu system, θ' [42] from the Al–Cu system, and so on. The precipitates mentioned in the sequences are described in the following subsections.

2.6.2 Early precipitation

After SHT and quenching to room temperature, the configuration of evenly distributed solute atoms is energetically unfavourable. By the vacancy pump mechanism, atoms diffuse inside the material and occasionally form solute–solute bonds. This results in a slightly uneven distribution, and eventually the formation of small clusters of solute atoms. The kinetics and effects of clustering can be measured by Vickers hardness [43, 44], electrical resistivity [45, 46], differential scanning calorimetry (DSC) [46, 47], and positron annihilation spectroscopy (PAS) [48, 49], and the clusters themselves can be studied by atom probe tomography (APT) [50–52]. The phenomenon of cluster hardening during room temperature (RT) storage is called *natural ageing* (NA). The clustering process is accelerated by annealing the material at temperatures up to 100 °C [51]. Figure 2.7 shows an APT volume of a typical cluster microstructure in a pre-aged condition.
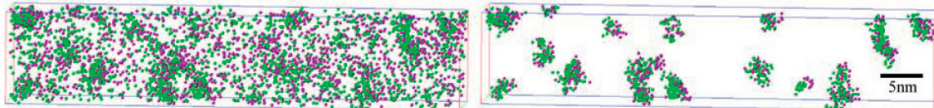

Figure 2.7: APT volume of an Al alloy with 0.95 wt.% Mg and 0.81 wt.% Si, pre-aged at 100 °C for 1 week. The left image shows all Mg (green) and Si (purple) atoms while the right image shows clusters extracted by the maximum separation method. From [51].

The definition of a Guinier–Preston-zone (GP-zone) [53] somewhat overlaps with what is called a solute cluster. It is a solute-rich area of atoms still occupying Al fcc positions, but with its own ordered structure. A GP-zone structure closely related to β'' has been found and is denoted pre-β'' [54, 55].

The methods for studying clusters mentioned above have lead to a conclusion that there are several types of solute clusters [35, 56], sometimes divided into two classes called e.g. Cluster(1) and Cluster(2) [46, 51]. There seems to be some disagreement about the composition of these clusters (as found by APT), although both clusters are quite close to Mg/Si = 1 [51, 52]. Common to the interpretations is that Cluster(1) locks up solute and remains a cluster during subsequent ageing, while Cluster(2) serves as a nucleation site for precipitates. Therefore, one naturally wants more of Cluster(2). Cluster(1) is seen as the cause of the negative effect of room temperature storage [44, 57], in dense $6xxx$ alloys. Lean alloys, on the other hand, enjoy a positive effect when stored at room temperature before later ageing [58]. Clusters in other alloy systems like $2xxx$ and $7xxx$ do not possess this "double-edged sword" behaviour [59].

Upon artificial ageing, clusters nucleate precipitate phases with non-fcc structures. Since clusters may form anywhere inside the matrix, this is called homogeneous nucleation. Its antonym, heterogeneous nucleation, refers to the formation of precipitate phases at grain boundaries, dislocations, and other (large) particles such as dispersoids. Nucleation on dislocations (seen in the upper right corner of Fig. 2.4) is of particular importance as industrial products are often deformed, causing almost all precipitates to form on dislocations. This lowers the nucleation energy barrier, so that the artificial ageing time required to achieve peak hardness is lowered [27].

2.6.3   Peak age and β''

All the non-equilibrium precipitates listed in the sequences (2.1 and 2.2) are needle- or lath-shaped and have their main growth and coherency directions along the $\langle 001 \rangle_{Al}$ directions. Figure 2.8 shows what the microstructure of a typical Al–Mg–Si alloy looks like at peak hardness. Since this particular specimen is from a non-deformed material, homogeneous precipitate nucleation dominates. Most precipitates are here of the β'' type. This is the most important precipitate for hardening in $6xxx$ alloys as it has an excellent coherency with the Al matrix. Its secondary coherency directions are along $\langle 310 \rangle_{Al}$ and $\langle 320 \rangle_{Al}$ (see the unit cell in Fig. 2.9), which together with $\langle 001 \rangle_{Al}$ usually define the precipitate–matrix interfaces. It was discovered in the 90s by TEM [60, 61]. By nanobeam diffraction (NBD) and first-principles calculations, an atomic model of its structure was created,
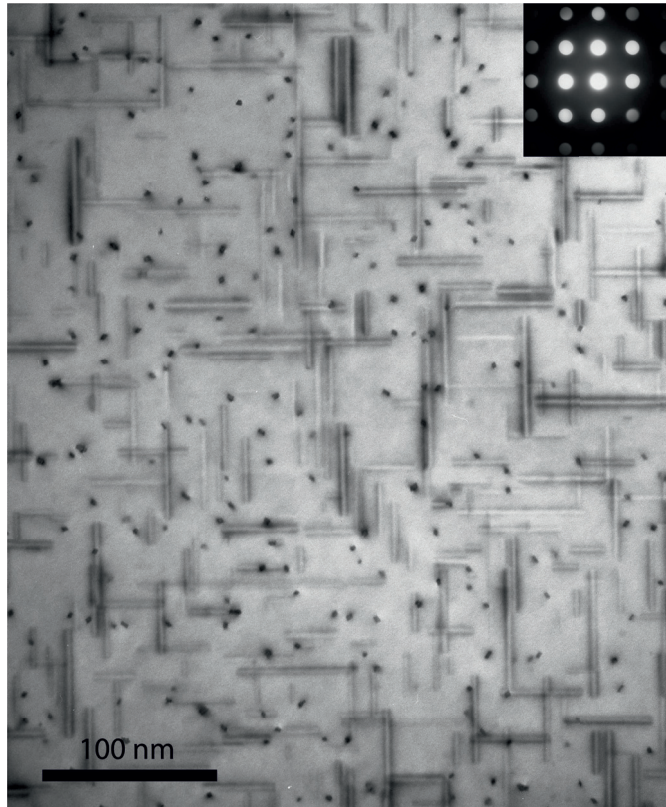
Figure 2.8: A typical TEM image of the microstructure in an Al–Mg–Si alloy (A2 NA+AA from paper 3), seen in the $\langle 001 \rangle_{Al}$ direction. β'' needles are seen in both cross-section and from the sides. The inset shows the $\langle 001 \rangle_{Al}$ zone axis pattern.

with the composition Mg_5Si_6 [62]. This composition has been the subject of later doubt, and a composition closer to $Mg_5Al_2Si_4$ was measured using APT [63].

2.6.4   Overageing phases in Al–Mg–Si

Upon overageing, new phases, generically referred to as post-β'', are generated. The most commonly appearing of these is the hexagonal phase β' [64, 65]. It precipitates as longer, thicker, and less coherent needles than the β'' phase, and usually has a rounded cross-sectional shape.

The phases U1, U2 and B' were first reported by Matsuda *et al.*, and was referred to as Type A, Type B and Type C, respectively [36]. U1 is a trigonal phase that grows in Si-rich alloys, while U2 is orthorhombic and
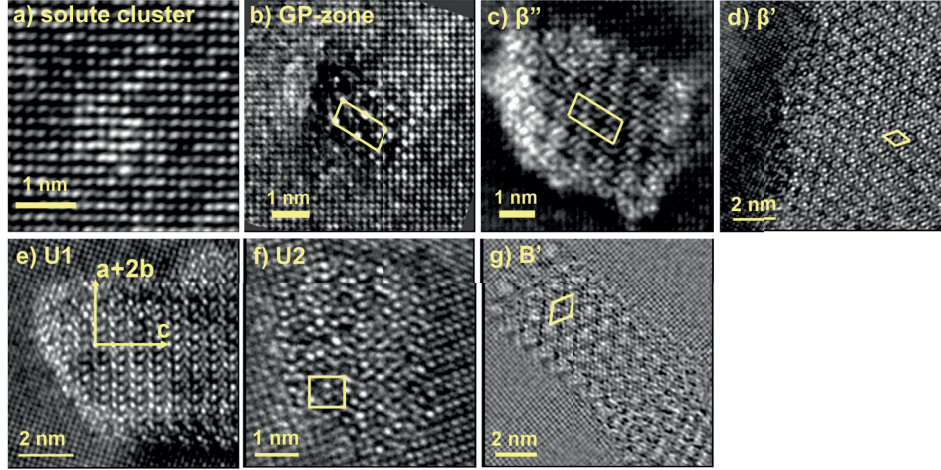
Figure 2.9: High-resolution TEM images of precipitates from (2.1), all taken on FEG microscopes by Calin D. Marioara. (g) is reconstructed from through-focus exit wave images.

has a more balanced composition [66]. Both of these grow as quite large rod-like particles with rounded cross-sections. B′ is somewhat special as it has only been found to nucleate heterogeneously. This phase often occupies regions high in dislocation density, where B′ particles appear as pearls along a string. B′ has a lath-shaped cross-section, a hexagonal structure, and a secondary growth direction along $\langle 510 \rangle_{Al}$ [67]. The full details about these structures and the others in the precipitate zoo can be seen in Table 2.2. Figure 2.9 shows example TEM images of all metastable phases in the Al–Mg–Si system.

The four phases mentioned here are all the confirmed phases following β'' in the precipitation sequence, although variations have been reported, e.g. U3 [55]. An intriguing property of the phases is that they all host the *Si network*, a Si substructure with projected approximate hexagonal symmetry along the main growth direction [68]. One can go from one phase to another by changing the heights of the atoms in the Si columns, and how columns of other atoms are arranged in between. Figure 2.10 shows this schematically for a generic structure with a perfect Si network. Precipitates hosting the Si network have unit cells with projections that coincide well with both {001} planes in fcc Al and {111} planes in diamond Si [68].

Table 2.2: Precipitate phases in the Al–Mg–Si(–Cu) system, and what is known about them. U1, U2 and B′ are also called Type A, Type B and Type C, respectively. Adapted from [40]. Most of the structures are shown in TEM images in Figs. 2.9 and 2.11.

| Phase	Composition	Space group	Lattice parameters [nm]	Sources
GP zones	Mg$_{2+x}$Al$_{7-x-y}$Si$_{2+y}$	$C2/m$	$a = 1.48, b = 0.405, c = 0.648, \beta = 105.3°$	[54, 71, 72]
β″	Mg$_5$Si$_6$ / Mg$_5$Si$_4$Al$_2$	$C2/m$	$a = 1.516, b = 0.405, c = 0.674, \beta = 105.3°$	[63, 72, 73]
β′	Mg$_{1.8}$Si	$P6_3$	$a = b = 0.715, c = 0.405, \gamma = 120°$	[64, 65]
U1	MgAl$_2$Si$_2$	$P\bar{3}m1$	$a = b = 0.405, c = 0.674, \gamma = 120°$	[36, 65, 66, 68]
U2	MgAlSi	$Pnma$	$a = 0.675, b = 0.405, c = 0.405, \gamma = 0.794$	[36, 37, 65, 66]
B′	Probably Mg$_9$Al$_3$Si$_7$	Hexagonal	$a = b = 1.04, c = 0.405, \gamma = 120°$	[36, 65, 67, 74]
β	Mg$_2$Si	$Fm\bar{3}m$	$a = 0.635$	[65, 75]
QP	Unknown	Hexagonal	$a = b = 0.393, c = 0.405$	[76]
QC	Unknown	Hexagonal	$a = b = 0.670, c = 0.405$	[76]
C	$\approx$ Mg$_4$Al$_3$Si$_{3.3}$Cu$_{0.7}$	$P2_1/m$	$a = 1.032, b = 0.81, c = 0.405, \gamma = 101°$	[40, 77]
L	Variable	(Disordered)	Variable	[39, 40, 78]
Q′	Probably Al$_3$Cu$_2$Mg$_9$Si$_7$	Probably $P\bar{6}$	$a = b = 1.032, c = 0.405, \gamma = 120°$	[38, 39, 79, 80]
Q	Probably Al$_3$Cu$_2$Mg$_9$Si$_7$	$P\bar{6}$	$a = b = 1.039, c = 0.402, \gamma = 120°$	[79, 80]
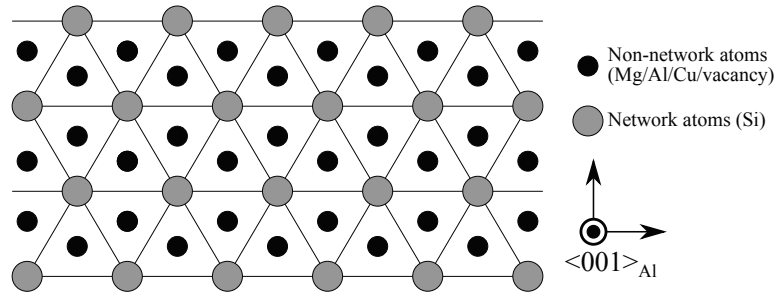
Figure 2.10: Template for a precipitate structure hosting the Si network. Specifying all the atom heights, the composition of the non-network columns and the orientation of the network with respect to the lattice gives a specific precipitate structure. A stricter scheme where the non-network atom heights are predetermined works for the U2, C and Q′ structures [69, 70].

2.6.5 Cu-containing phases

Additions of Cu to the alloy composition enables the precipitation of additional phases and a following extension of the precipitation sequence, as seen from (2.2). C is the first phase in the sequence, and forms as thin coherent plates oriented along {001} planes in Al [40, 77]. A more common variant is L, which is thicker than C and lacking a unit cell [39, 40, 78]. Areas with disorder, that can not be described by a repeating unit cell (although other forms of symmetry can be present) is occasionally seen in metastable precipitates of all types. Among disordered precipitates, L is a special case since it is common enough to have received its own name. Q′ has a beautiful hexagonal structure, and it is isostructural to B′, but can nucleate homogeneously [38, 39, 79, 80]. It appears as thick lath particles, sometimes partially disordered. STEM images of C, L and Q' are shown in Fig. 2.11. QP and QC, which are variants of the Q/Q′ structure, were reported by Cayron *et al.* [76] and may appear earlier than Q′ in the precipitation sequence [40]. All these phases contain the Si network, with Cu columns most often located at a position with a particular local symmetry [77].

U2, L, C, and Q′/Q have particularly simple structures with a 2/1 ratio of metal atoms to Si atoms [69, 70]. When viewed in the $\langle 001 \rangle_{Al}$ direction, all atoms can be simplified to occupying two heights, with a strict pattern for metal atoms. The heights of the Si network atoms also seem to follow certain rules. Thus, even though disordered precipitates such as L lack a unit cell, they have a short-range order and a partially deterministic growth [6, 70].
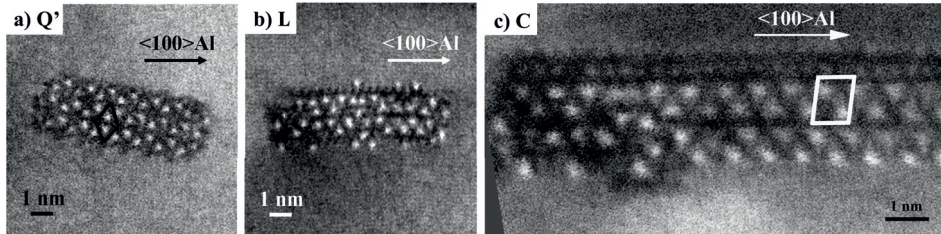
Figure 2.11: HAADF–STEM images of Cu-containing precipitates from (2.2), all taken on a Jeol JEM-2010F by Håkon Hasting and Antonius T. J. van Helvoort. Thanks to Z contrast (see section 3.1.2), Cu atomic columns are visible as bright dots.

2.6.6 Equilibrium phases

The equilibrium phase β has a cubic crystal structure, and can be either cube- or plate-shaped. The cubic particles have the orientation relationship $(001)_{Al}||(110)_\beta$, $[110]_{Al}||[001]_\beta$, while the plates have $(001)_{Al}||(110)_\beta$, $[100]_{Al}||[001]_\beta$ [81]. It is considered an incoherent phase, although the orientation relationships imply a coincident site coherency with the Al matrix. As all equilibrium phases in the $6xxx$ system, β has no significant hardening potential. Historically, its composition Mg_2Si was thought to be common for all the precipitates. This lead to widespread use of the ratio $Mg/Si = 2$ in alloy compositions, and specifications using the semi-binary composition Al–$x\%$ Mg_2Si.

In Si-rich alloys, diamond Si can also precipitate in the Al matrix. Much like β, large cubes or plates of Si form with two orientations: $(001)_{Al}||(001)_{Si}$, $[100]_{Al}||[100]_{Si}$ and $(001)_{Al}||(110)_{Si}$, $[010]_{Al}||[1\bar{1}\bar{1}]_{Si}$ [82].

Q is the main equilibrium phase of the Al–Mg–Si–Cu system. It is isostructural to the B′ and Q′ phases. Unlike the other equilibrium phases, it hosts the Si network, making its relationship to the metastable phases much more apparent than for β and Si.

2.6.7 Why is it a sequence?

Why does the microstructure go through all the metastable precipitates (which are beneficial for mechanical strength) instead of creating an equilibrium phase to begin with? The answer involves thermodynamics and precipitate–matrix interactions. The total formation energy (or enthalpy) of a precipitate can be decomposed into bulk energy (negative), interface

energy (positive), and strain energy (positive, primarily matrix strain):

$$E_{\text{total}} = E_{\text{bulk}} + E_{\text{interface}} + E_{\text{strain}}. \tag{2.3}$$

Setting E_{bulk} proportional to the precipitate volume and $E_{\text{interface}}$ proportional to the interface area gives an approximate model from which the principles of the precipitation sequence can be understood. All precipitates must start small, and this means a high ratio of interface area to volume, making interface energy the most important term. The most coherent precipitates induce a relatively high strain in the matrix, but have a low enough interface energy to still be most beneficial at early stages of precipitation. After the precipitate has grown large, the balance shifts and coherency loses importance. This favours a transition to phases of lower bulk energy but a poorer coherency with the matrix. This process is sometimes called Ostwald ripening [83].
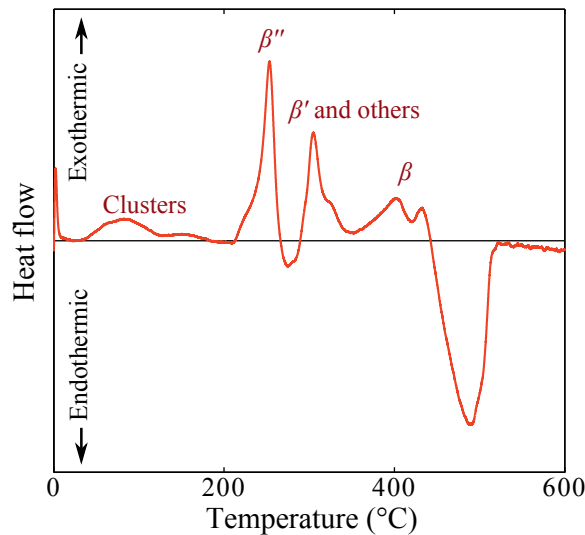
Figure 2.12: Differential scanning calorimetry measurement, using the A2 alloy from paper 3 [84]. The scanning speed is 10 °C/min. Interpretations of exothermic peaks are marked in terms of the phases formed. The endothermic peaks arise from the dissolution of phases.

Each precipitate structure represents a local minimum of energy. For the transition from a microstructure consisting mainly of one specific phase in the sequence (2.1 or 2.2) to the next phase, a sufficient temperature and ageing time is needed. This is well illustrated by differential scanning calorimetry (DSC) measurements (see Fig. 2.12 for an example) in which

the formation of each phase gives an exothermic peak, reflecting the jump from one local energy minimum (a maximum on the plot) to the next.

Exactly how overageing precipitates form out of a microstructure mainly consisting of β'' or other peak hardening phases is a mystery. There are mainly two possibilities: Internal transformations, which require that a lot of atoms change places so that a whole precipitate can change its crystal structure, and external nucleation of a new phase on the interphase of an existing precipitate. The last option seems the most likely one, as β'' particles become rounder upon over-ageing and start to include disordered parts hosting the Si network [85]. This could help the transition to later, less coherent phases.

Chapter 3

Experimental techniques

The work presented in this thesis has been mostly experimental. The objects of study have been nanometre-sized particles, and the investigation of these requires sophisticated techniques. I present here electron microscopy, which is primarily an imaging technique, and two spectroscopy-like techniques, muon spin relaxation and positron annihilation spectroscopy. In addition, hardness measurements are explained as they are used to study the most important characteristic of structural materials: mechanical strength.

3.1   Transmission electron microscopy (TEM)

From the name of the technique, one can understand its principle: Shooting electrons through a specimen to observe small objects. Most of the specimens being studied are in the solid state, but innovation in TEM design have introduced enough flexibility to also allow the study of biological materials, gases and liquids. Many different TEM techniques exist to extract structural, electronic, and chemical information from a material. Most microscopes are multi-purpose, although some are dedicated to narrow applications and excel in one specific technique.

Figure 3.1 shows how a typical TEM works. Electrons are emitted from a gun and accelerated by an electric field, most commonly to energies of 60–300 keV. The gun is either a thermal emission gun made of W or LaB_6 or a field emission gun (FEG) made of W. A FEG gives the electron beam a superior coherency, with an energy spread below 1 eV [86]. This ensures a higher spatial resolution in STEM images and a higher energy resolution in EELS (sections 3.1.2 and 3.1.3). Electrons travel through high vacuum all the way through the TEM column. Analogous to optical lenses, adjustable electromagnetic fields manipulate the electron beam, and also makes them go

Electron gun

Accelerating field

Condenser lens 1

Condenser lens 2
and cond. aperture

Upper objective lens

Specimen

Objective lens

Objective aperture

Intermediate lens
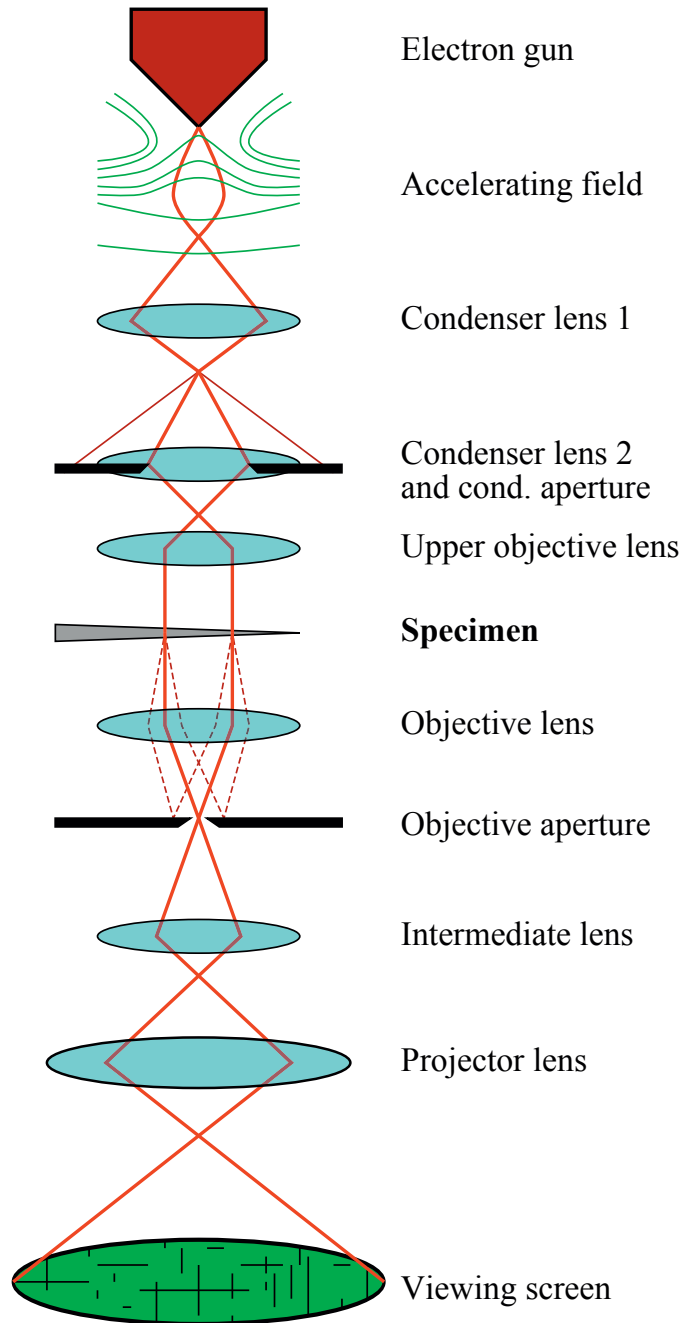
Projector lens

Viewing screen

Figure 3.1: Schematic of a typical TEM column in bright-field imaging mode. The dashed lines represent diffracted electron beams. Most microscopes have more lenses than shown to increase the flexibility in controlling the electron beam.

in spiral paths. The condenser aperture selects the most coherent part of the beam. In TEM mode (as shown), the beam is made approximately parallel when it hits the specimen, to illuminate the whole area of interest. Lenses focus the direct and diffracted beams to create either a diffraction pattern or an image of the specimen. This can be directed onto a fluorescent viewing screen, a film plate, a charge-coupled device (CCD) camera or EELS/STEM detectors.

The electromagnetic lenses in a TEM suffer from the same horror as optical lenses in a camera: aberration. While a (two-dimensional) parabolic glass lens has a single focal point, the light which hits a spherical lens will be refracted differently dependent on where on the lens it hits. Also, due to the wavelength-dependent index of refraction of glass, blue light refracts more strongly than red light. Respectively, these effects are called spherical and chromatic aberration, and both have their analogies in electron optics [87]. Spherical aberration C_s is the most important of these when it comes to imposing a limit to the resolution of TEMs. To fight this effect, aberration correctors have been devised and have become widespread in the course of the last decades [88, 89]. They come in the form of hexapole or quadrupole–octupole magnets, and can be mounted below the specimen for TEM image correction or above the specimen for STEM probe correction. The technology has improved TEM resolution below the atomic diameters of most chemical elements [89].

TEM specimens are circular discs, usually 3.05 mm in diameter. Condensed matter specimens can be in the form of particles dispersed on a grid, smaller specimens (e.g. wedge-shaped, cross-sections between materials) glued to a metal ring, or they can be self supporting foils of bulk material. At the area of interest, the thickness has to be below about 100 nm for high electron transparency. The required thickness depends on the type of material studied, the acceleration voltage, and what information one wants to obtain.

3.1.1 Electron–specimen interactions

Once an electron enters a specimen, it experiences one of many modes of interaction. These are summarised in Fig. 3.2. Elastically scattered electrons are the most useful for conventional TEM as they are the basis for diffraction contrast and phase contrast imaging in bright-field, dark-field, and high resolution TEM. Inelastic scattering means that electrons lose energy while passing through the specimen. The energy is handed over to phonons, plasmons, or ionisation of atoms. Having lost energy, the electrons can be used for EELS (section 3.1.3), while X-rays emitted by the ionised atoms can be

Incident
electron beam

Backscattered
electrons
(SEM)

Secondary
electrons
(SEM)

Characteristic
X-rays
(EDS)

Visible light

Auger electrons

Electric current

Incoherent
elastically scattered
(HAADF–STEM)

Bremsstrahlung

Inelastically
scattered
(EELS)

Direct
beam

Elastically scattered
(diffraction, imaging)
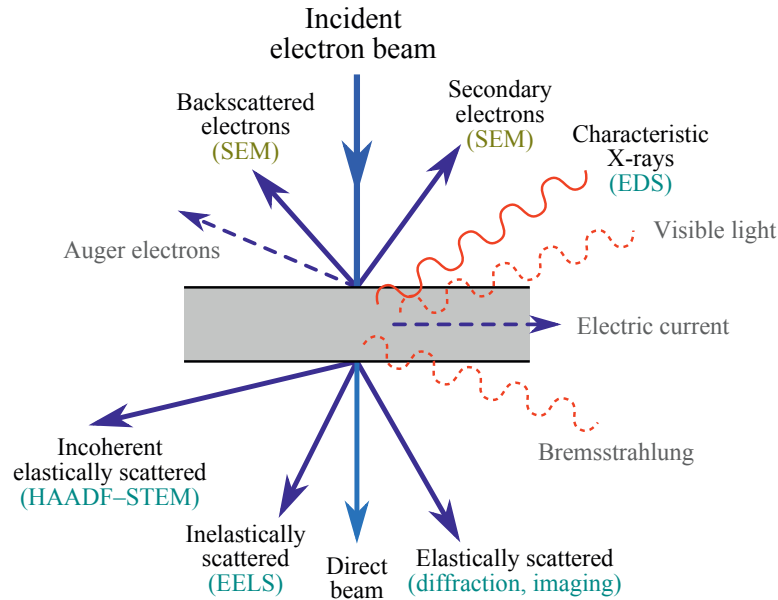
Figure 3.2: The possible ways an electron can interact with a TEM specimen. Scattered electron beams are straight lines while photon beams are curved. The angles are exaggerated: the forward scattered electron beams will for example be very close to the direct beam. Adapted from [90].

picked up by an EDS detector (section 3.1.4). High-angle scattered electrons are incoherent, which HAADF–STEM imaging takes advantage of (section 3.1.2). For backward scattering, which is relevant for SEM, see section 3.2.

Quantum mechanics dictate how electrons are scattered by different objects in the specimen (most importantly core and conduction electrons, phonons, and plasmons). A great effort has been made to understand the scattering processes mathematically, to quantitatively compare theory and experimental results [91, 92]. Specifically, STEM simulations are of great interest as the imaging conditions are easier to control in this mode than with parallel illumination TEM [93]. Quantitative comparison of experimental and simulated images is therefore feasible, and often used to help understanding the structures one looks at.

Understanding our results qualitatively can also be a challenge: what do the images we record actually show? One part of this problem is that TEM is a two-dimensional projection of a three-dimensional material, as illustrated in Fig. 3.5. It is therefore difficult to judge whether a nano-sized particle is in front of or behind another, and whether they stick together. There

are many ways to form a TEM image, and several contrast mechanisms will
contribute in all cases. The important mechanisms are explained below [90]:

- The simplest mechanism is called *mass–thickness contrast*, and should
  be familiar to anyone who has broken a bone and had an X-ray image
  taken. Like X-rays, electrons are absorbed by and otherwise interact-
  ing with the material they are going entering in a way that prevents
  them from going completely through (see the upper half of Fig. 3.2).
  This means that thick areas and areas with heavy elements appear dark
  in images. This contrast mechanism is always present in (S)TEM, and
  is predominantly exploited at low magnifications for finding a thin area
  to study.

- High-resolution TEM (HRTEM) imaging uses *phase contrast*. This can
  be explained through an analogy in light optics: a coherent ray of light
  diffracts when hitting an object, and all diffracted rays can be focused
  together to form an image of the object. Whether an area in the image
  is bright or dark depends on whether the light rays have interfered con-
  structively or destructively, that is, whether they reached the viewing
  screen or detector with the same or opposite phases. The same idea
  applies to electrons, although they have a much shorter wavelength
  than light. When observing an atomic lattice, atoms should ideally
  appear bright against a dark background in a HRTEM image. Phase
  contrast is however more complicated than this, thanks to *contrast re-
  versal*. Electron beams at high diffraction angles, which produce the
  finest details in images, can have opposite contrast from the direct
  beam. At even higher angles, the contrast can reverse several times.
  The spatial frequency (and hence resolution) at which this occurs is
  determined by the thickness of the specimen, the acceleration voltage,
  the spherical aberration, and the defocus [90].

- In imaging mode, an objective aperture can be inserted to only let one
  or a few beams through. If the direct beam is selected, we get bright-
  field (BF) imaging, while selection of a diffracted beam gives dark-field
  (DF) imaging. These techniques give contrast between different ma-
  terials and different phases of the same material. They can also help
  with orientation to a specific zone axis, which makes dark bending
  contours appear in BF mode. Similar-looking thickness fringes appear
  in wedge-shaped specimens due to oscillations between constructive
  and destructive interference [90]. These effects are often collectively
  called *diffraction contrast*. BF and DF images have a poor resolu-
  tion in comparison with HRTEM images because high-angle scattered

electrons are cut off and short spatial frequencies can not be resolved. These modes are hence used when good diffraction contrast is more important than high resolution.

- Atomic number contrast or *Z contrast* is a form of mass–thickness contrast, but relates specifically to the contrast between atomic structures or columns with different lighter/heavier elements. This is most relevant in HAADF–STEM imaging, which is described in the next section.

3.1.2 Scanning TEM

While conventional TEM images an area of interest by directing a parallel beam at it, STEM[1] uses a focused electron probe which is scanned over the area to form an image on a monitor. The beam hits one point on the specimen at the time. The size of this "point", determined by how well the electromagnetic lenses are able to focus the beam, is called the *probe size*. For high-resolution STEM imaging, a FEG source is needed. This gives a probe size of ≈ 0.2 nm for uncorrected and ≈ 0.1 nm for probe-corrected microscopes. Keeping the probe static produces a convergent beam electron diffraction (CBED) pattern. Apart from CBED imaging being its own technique for investigating crystal structure and electron orbitals (see e.g. [94]), it is used in STEM mode to tilt to a zone axis and to estimate the specimen thickness.

High-angle annular dark field STEM (HAADF–STEM) uses a donut-shaped detector. The high-angle scattered electrons are incoherent (give little or no phase contrast) and can therefore be used to form easily interpretable images. Two processes give rise to the high-angle scattering: thermal diffuse scattering by phonons and Rutherford scattering by atomic nuclei [95, 96]. The fraction of electrons which are high-angle scattered depends strongly on the atomic number of the elements contained in the specimen. There is an approximate power-law relation between the intensity I and the atomic number Z:

$$I \propto Z^{\alpha}. \tag{3.1}$$

Pure Rutherford scattering predicts $\alpha = 2$, but the addition of thermal diffuse scattering and the imaging conditions in HAADF–STEM yields $\alpha = 1.3$–1.8, depending on the specimen thickness and the thermal vibrations of each element, amongst other things [95, 96].

---

[1]STEM (and SEM) should not be confused with scanning tunnelling microscopy (STM), which uses the tunnelling current between a sharp tip and a sample to study surface morphology.

3.1.3 Electron energy loss spectroscopy (EELS)

Inelastically scattered electrons can be a nuisance in imaging and diffraction work, in particular when doing CBED experiments [97]. Energy filtered TEM (EFTEM) can be used to include only electrons with no energy-loss in images/diffraction patterns. However, effects which make the physics more complicated can often be used to our advantage, for extracting additional information from the system by experiments. Instead of being used for imaging, electrons that have interacted with a TEM specimen can be directed to an energy loss spectrometer to measure exactly *how* inelastically scattered they are, that is, how much energy they have lost by going through the specimen.

An EEL spectrometer works by deflecting the electron beam 90° onto a detector using a magnetic field. The magnetic part of the Lorentz force grows stronger with electron energy, so low-energy electrons are deflected less than electrons with no energy loss. This effect transforms energy loss to spatial positions on the detector in a linear fashion. An energy-loss spectrum can contain an amazing amount of information about the material under study. The coherency of the beam emitted from the electron source in the TEM largely determines the energy resolution of an obtained EEL spectrum, although e.g. aberrations in the spectrometer can degrade the resolution [86].

A rough explanation of the different parts of an energy loss spectrum follows [86]:

- The zero-loss peak has a width determined by the energy resolution, which is typically 0.3–3 eV. It includes the direct beam and elastically scattered beams, as well as electrons that have lost a very low amount of energy, typically from collisions with phonons.

- Semiconductor band gap transitions give weak features in the very low-loss regime. The band gap of Si, the most famous semiconductor, is 1.1 eV, so a very good energy resolution is required to distinguish it from the decaying zero-loss peak [98].

- Plasmon excitation peaks appear in the low-loss region. A plasmon is a type of quasiparticle and is an oscillation of local electric charge in a material. Aluminium has its lowest-energy plasmon peak at 15 eV [99]. Higher-energy peaks appear when electrons excite multiple plasmons.

- Core-loss peaks (called *edges*) appear for each chemical element, from 13.6 eV for hydrogen, and upwards [100]. As a core electron in an atom is ionised by a beam electron, an energy loss equal to the ionisation

energy of the respective atom will be measured. The local chemical environment around an atom varies the onset energy and appearance of an edge, and creates what is known as *fine structure* [86]. This effect can be used for determining the type of chemical bonds and the electronic density of states above the Fermi level using electron loss near-edge structure (ELNES) and extended electron loss fine structure (EXELFS) [90].

- Multiple scattering convolutes the spectrum with itself along the energy loss axis. The decay of the zero-loss peak, plasmon peaks and core loss edges disturb signals from higher energy loss, and is simply referred to as a signal background. Due to the complexity of the different scattering processes, the background is not easily modelled, but is commonly subtracted from core-loss signals by assuming an exponential or power law decay [86].

Figure 3.3 shows the typical location of EELS core-loss edges of elements that have been confirmed to accumulate inside precipitates in $6xxx$ alloys.
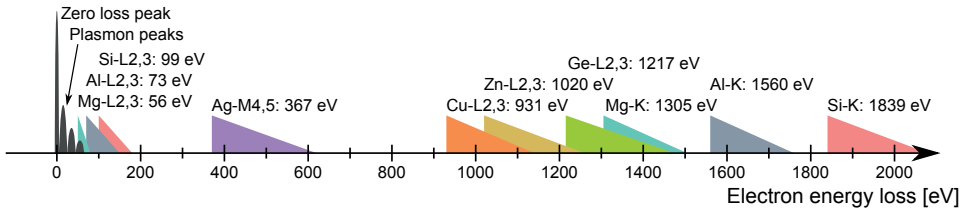
Figure 3.3: Locations of EELS edges relevant to Al–Mg–Si alloys along the energy loss axis (energies from [100]).

EELS is used in papers 3 and 4 to estimate the thickness of TEM specimens, which is required for precipitate number density measurements. This analysis relies on a simple model that assumes that an electron has a constant probability of being inelastically scattered (while exciting plasmons) per distance it travels through the specimen. The model yields the following formula for the thickness t [90]:

$$I_0 = I_{\text{total}} e^{-t/\lambda}. \tag{3.2}$$

Here, I_{total} and I_0 are the total and zero-loss intensities, respectively, and λ is the *inelastic mean free path*, equal to the inverse of the scattering probability per distance. One can calculate λ theoretically [101], and in Al alloys, $\lambda \approx 111$ nm for 150 keV electrons.

When used in tandem with STEM, the method can be used to measure spectrum images, with one EEL spectrum per pixel. Data analysis enables the creation of elemental maps, where an image is coloured by the amount of signal from each element present in the specimen. Atomic-resolution EELS mapping is the subject of paper 5, and is described in greater detail in section 3.1.5.

3.1.4 Energy-dispersive (X-ray) spectroscopy (EDS)

EDS/EDX/XEDS is a spectroscopy technique which measures the energy of X-ray photons emitted from a TEM specimen. In atoms ionised by the electron beam, an electron will quickly do a quantum leap from an outer shell to fill the hole left in one of its inner shells. This process creates an X-ray photon with energy equal to the difference in binding energy of the two electron orbitals. The photon is caught by a side-mounted detector in the backwards direction (towards the electron source). The direction of greatest X-ray intensity from a material has the emission angle (from the surface normal) equal to the incident angle of the electron beam [90], as for reflection of light rays. Specimens should therefore be tilted towards the detector to maximize the X-ray count rate.

EDS uses another result of the ionisation process which enables core-loss EELS analysis. The two techniques are also complimentary in other senses: EELS is perfect for detecting light elements (C,N,O,F) while EDS is more efficient for heavy elements, EELS gets a higher-quality signal from very thin specimens while thick specimens increase the EDS count rate, and ED spectra are straightforward to analyse while EEL spectra contain more information. As electron transmission is not required for the detection of X-ray photons, EDS detectors are also used for chemical analysis in SEMs.

An EDS detector can be used in tandem with e.g. a HAADF–STEM detector to image a specimen both by Z-contrast and by the amount of each chemical element present. Elemental maps are created from ED spectra obtained for each pixel (electron beam location) in an image. The amount of an element is quantified roughly by measuring the area of the peaks associated with that element. This method is used both with TEM and SEM in paper 4 to map the distribution of elements in a Ca-added Al–Mg–Si alloy.

3.1.5   Application to aluminium alloys

Specimen preparation

Seen at a scales above $\sim 10\,\mu m$, precipitates grow uniformly in bulk Al alloy samples. Therefore, to study both single precipitates and the statistics of an ensemble of precipitates, a TEM specimen can be made from anywhere inside the bulk of some material. Mechanical polishing is used to produce a 50–150 µm thick foil of the material, out of which specimen discs are cut. The centre of the disc can be thinned by electrolyte polishing (electropolishing) or dimpling/ion milling until a tiny hole is created. The edges around this hole are thin enough for electron transparency and are used to acquire TEM images. Electropolished and ion milled specimens with visible holes are shown in Fig. 3.4. The important characteristics of a specimen is cleanliness,
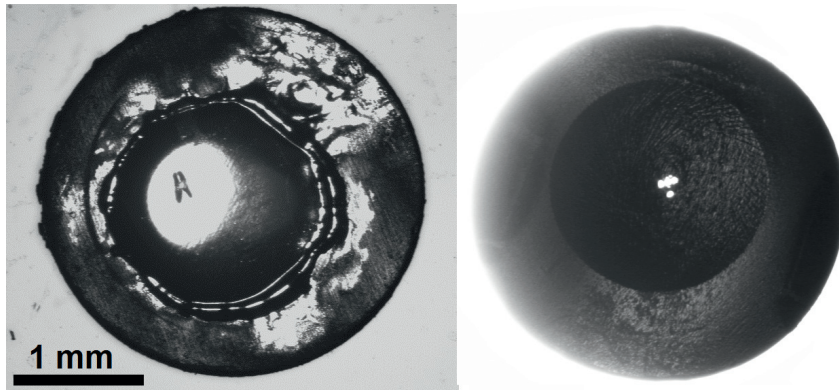
Figure 3.4: Electropolished (left) and dimpled/ion milled (right) TEM specimens of Al–Mg–Si alloys.

the presence of a thin, non-bent area and that this area has the correct crystallographic orientation. Peak-aged Al–Mg–Si alloys have needle-shaped precipitates along $\langle 001 \rangle_{Al}$, making this the relevant viewing direction in a TEM. A small grain size in the material is preferable since this increases the likelihood of observing grains where the specimen surface normal is close to being parallel to a $\langle 001 \rangle_{Al}$ direction. Grain texture may increase this likelihood, e.g. for extruded bars, where low-index zones are often oriented along the extrusion direction [102].

Electropolishing is a quick method to make many specimens, typically with one big hole surrounded by flat surfaces. In papers 3 and 4, electropolishing was conducted on a Struers TenuPol-5. A mixture of 2/3 methanol and 1/3 nitric acid has been found to work well for preparing specimens

of $6xxx$ and $7xxx$ alloys. For optimum efficiency, this electrolyte is cooled down to a temperature around $-25\,°C$, using liquid nitrogen or a built-in cooling system. The optimal voltage varies with the material, but is close to 20 V for Al alloys. This gives a current through the specimen of 50–300 mA, depending on the thickness of the disc and the composition of the alloy.

If done carefully, ion milling will create several small holes with thinner, cleaner areas around them. Although taking much more time per specimen than electropolishing, this is the preferred method for high-end microscopy of single precipitates. A flat disc of 60–90 µm is normally used for dimpling. Using diamond paste with 1–3 µm granules, dimpling to a middle thickness of 20–25 µm leaves a nice pit to shoot Ar ions into. Ion milling typically takes 4 hours if done carefully. A Gatan cold PIPS (precision ion polishing system) was used for the work in paper 5. A good starting voltage is 4.0 kV, and when a small hole has appeared, 3.0 kV is sufficient to expand it. A lower voltage of 1.5–2.0 kV should be used during the last 20 minutes to reduce the thickness of amorphous Al on the specimen surface.

Quantification of microstructure

The morphology and spatial distribution of hardening precipitates are of great interest. For the quantification of these, as well as the determination of precipitate types, a thermal emission microscope is sufficient, and in many cases better than a FEG microscope, due to its ease of use and good diffraction contrast. Knock-on damage happens at energies above ≈ 170 keV in pure Al, so the operating voltage of the TEM should be at least below this to avoid damaging the specimen. Radiation-enhanced diffusion and precipitation may also occur in Al alloys [103]. In papers 3 and 4, BF images with the electron beam along the $\langle 001 \rangle_{Al}$ direction are used to count and measure precipitates. A slight tilt away from the zone axis will make the precipitates appear darker than the Al matrix due to diffraction contrast. Three average quantities are of interest: the cross-sectional area, length and concentration (number density) of precipitates. The product of these three values gives the total precipitate volume fraction. The volume fraction is not equal to the fraction of solutes in precipitates, as precipitates may contain Al and may contain more/fewer atoms per volume than the matrix.

The two-dimensional projection of a TEM is elusive. Figure 3.5 shows how the projection of a three-dimensional material in the TEM leaves some information out. Finding out whether precipitate needles are connected to each other or simply lie below or above each other is infeasible. Effects of the sample surfaces are not apparent in images, but must be accounted for. Specifically, electropolishing or ion milling a specimen cuts precipitates
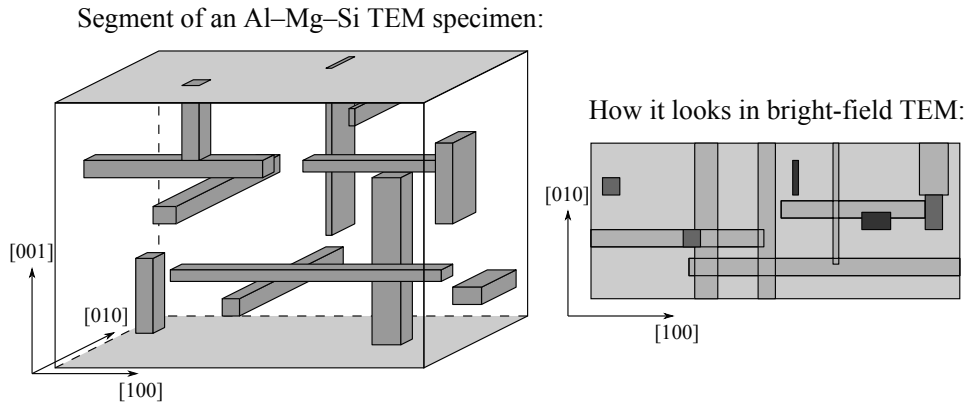
Segment of an Al–Mg–Si TEM specimen:

Figure 3.5: Schematic of a typical precipitate microstructure in a TEM specimen and how a TEM image of this would look. The specimen surface normal is oriented along [001] for simplicity.

that intersect with the surfaces [104]. Which precipitates are cut cannot be seen in a TEM, but the average length and concentration of precipitates can be corrected to account for the cutting. For this, one requires the angle between the viewing direction and the surface normal and the thickness of the specimen. There are several ways of measuring thickness. One of the most reliable methods uses EELS, as described in section 3.1.3.

In order to measure the precipitate characteristics consistently, we developed a MATLAB script for statistical analysis of precipitates in TEM images. The process is not fully automated as precipitates must be marked by hand for the following reasons:

1. Contrast may be different in different parts of the image because of variable sample orientation (bending).

2. Strain fields must be excluded from the precipitate cross-section.

3. One must separate between precipitates of in-plane and through-plane orientations.

4. It might be desirable to distinguish between different precipitate types.

For these reasons, a completely automated procedure for precipitate characterisation is infeasible and would produce misleading results. Nevertheless, the current script reduces the time needed and increases the flexibility of microstructure quantification when compared to a completely manual method.

For the papers in this thesis, about 10 high-magnification images were used in quantifying precipitate cross-sections, and about 10 low-magnification

images were used to count the number density and measure precipitate needle lengths. Although e.g. the distribution of lengths is quite broad, we include a sufficient number of precipitates in the analysis for the average numbers to be representative. The largest uncertainty ($\approx 10\%$) comes from the EELS thickness measurement, which primarily affects the uncertainties in the number density and volume fraction of precipitates.

STEM and STEM–EELS

STEM can be used to map heavy elements inside precipitates, and can even distinguish Si columns from Al and Mg columns because of their slightly higher Z contrast [105]. STEM is particularly useful when used on a probe C_s corrected microscope, making it possible to exactly locate columns of Cu, Ge, Ag, and other heavy elements. This depends on that a precipitate has the same atomic structure throughout its main growth direction, which is usually the case. The precipitate needle or plate must also extend through the specimen from top to bottom (not the case for any of the needles shown in Fig. 3.5), to avoid overlap with the Al matrix in a two-dimensional projection. The advantages of Z contrast imaging and probe correction are shown quite convincingly in Fig. 3.6. However, Nature is not keen on making pre-
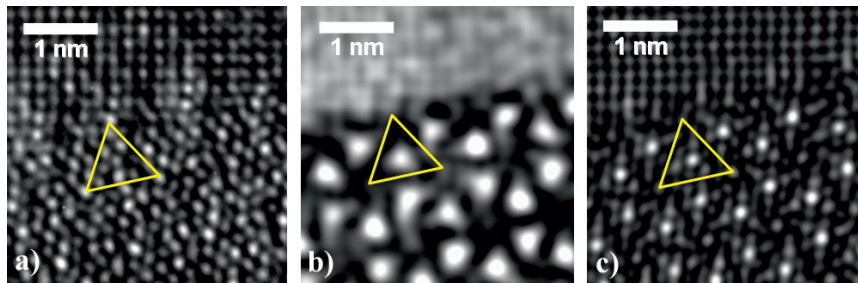
Figure 3.6: Comparison of TEM imaging modes applied to some very similar Q$'$ precipitates in an Al–Mg–Si–Cu alloy. Images are taken by Calin D. Marioara. (a) High-resolution TEM on a Jeol JEM-2010F, showing all atomic columns. (b) HAADF–STEM on the same microscope, with lower resolution, but added Z contrast. (c) Probe-corrected HAADF–STEM on a Jeol ARM, showing all atomic columns with Z contrast.

cipitate structure determination easy. When using STEM quantitatively, one often finds that columns with heavy elements are mixed with Al, Mg or Si [106]. If many elements are included in the composition of an alloy, it then becomes difficult to know exactly what kinds of elements are present

in each column, and whether the precipitate structure is rigid or has some compositional disorder.

STEM–EELS mapping can partially solve the problems mentioned, as it can determine what elements an atomic column contains. Paper 5 describes an initial study in using aberration-corrected STEM–EELS on aluminium alloy precipitates, conducted at the SuperSTEM facility [107] near the charming country village Daresbury in UK. We were able to record good data despite some difficulties: beam damage occurred in some precipitates, even with a 100 kV electron beam. A still bigger problem was carbon contamination, which is a well-known issue in STEM mode. Despite plasma cleaning, rinsing in ethanol and baking in vacuum, carbon collected easily at the electron-irradiated specimen surface. This was seen to be a bigger problem for $6xxx$ alloys than for $7xxx$ alloys, a fact confirmed by other research groups [108]. The best way to deal with the problem was giving the specimen electron beam showers for 30 minutes and acquiring spectra for 30 minutes, in a cycle. Baking in vacuum at $\approx 135\,°C$ for 12 hours is a reasonable pre-microscopy treatment. This heating was confirmed not to change the microstructure in the specimens, although it is possible that precipitate compositions were slightly altered by the increased solute diffusivity this treatment causes.
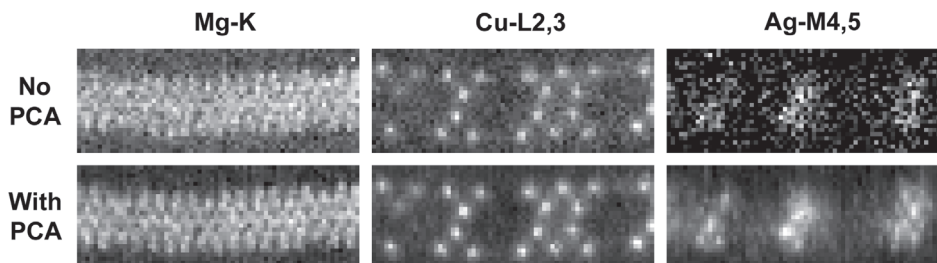
Figure 3.7: Elemental STEM–EELS maps from the "zebra" precipitate presented in paper 5. Background fitting and signal integration windows were modified to obtain the best possible images, with and without preceding noise reduction by PCA. The analysis makes a big difference in terms of resolvable features in spectrum images where the signal-to-noise ratio is low.

After STEM–EELS acquisition, spectrum images must be analysed to create elemental maps. In order to increase the signal-to-noise ratio of the spectra in an almost magical fashion, a form of multivariate statistical analysis (MSA) can be used [109]. For the elemental maps in paper 5, we used the principal component analysis (PCA) functionality of the freeware HY-

PERSPY program [110]. PCA diagonalises[2] a spectrum image and tries to separate the statistically significant features from the noise.

After this data treatment, background subtraction is needed to isolate the relevant core loss edge. A power-law fit to the signal at lower energies than the edge of interest is one of the most common approaches and was found to work well in our case. Once the background is subtracted, one can integrate the edge area and create a map of how much signal the edge contains for each spectrum in the image. The energy ranges for background fitting and edge integration can be selected manually by observing what gives the highest contrast and least noise in the elemental map. Figure 3.7 shows elemental maps from a plate-shaped precipitate, and illustrates how PCA improves spectrum images, in particular for edges with a low signal, such as the Ag-$M_{4,5}$ edge in this case.

3.2 Scanning electron microscopy (SEM)

The principle of SEM is the same as that of STEM all the way from the electron source to the specimen [111]. The difference lies in the type of detectors used, and in that the specimen can be of any shape, not necessarily electron-transparent. The two most common types of detectors are designed to pick up secondary and backscattered electrons (see Fig. 3.2).

Secondary electrons (SE) are conduction or valence band electrons that are knocked out of their orbitals by beam electrons [90]. They typically have a very low energy, and only SEs knocked out close to the surface are able to escape from the material. The SE detector makes use of an electric field to force these electrons to the side of the SEM column and into a scintillator. Obtaining topographical information is the most common use of a SE detector. Backscattered electrons (BSE) are simply reflected (elastically scattered) backwards by electrons within a specimen, and are detected with a donut-shaped detector, analogous to a HAADF detector. Like in HAADF–STEM, the signal increases with the average atomic number Z, lighting up an area with heavier elements, such as Fe- and Mn-containing phases in Al. BSE can also be used to form an electron backscatter diffraction (EBSD) image used for determining the crystallographic structure of the specimen [102]. SE and BSE detectors are included in some TEMs for surface characterisation of specimens.

For Al alloys, SEM is most commonly used to map grain orientations with EBSD or to study large equilibrium phases. Figure 3.8 shows that SEM can

---

[2]As in the linear algebra term. The spectrum image is a three-dimensional matrix (x, y, energy loss), which can be diagonalised.

provide nice low-magnification overview images of $6xxx$ alloy microstructure in certain cases. SEM is used in paper 4 to study the distribution of Ca-
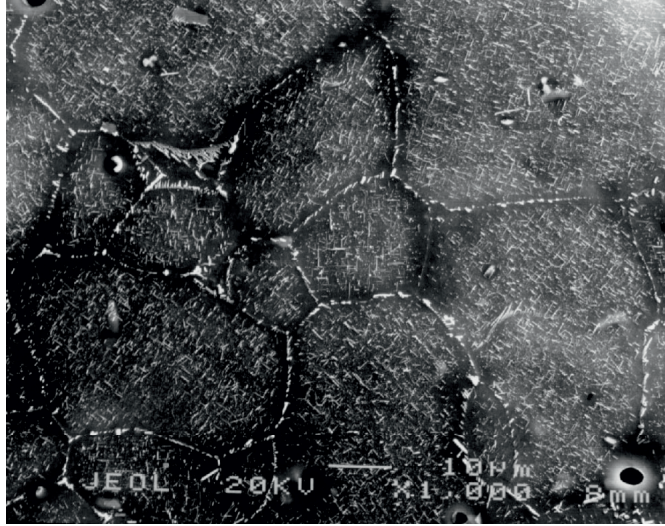
Figure 3.8: Secondary electron SEM image of an over-aged microstructure in a 6013 alloy [28]. Bulk precipitates, grain boundary precipitates (both most likely Q phases) and precipitate-free zones are visible.

containing particles which were too large and coarsely dispersed for TEM analysis. As in TEM specimen preparation, electropolishing is the main technique for making SEM specimens out of bulk metals. Other preparation techniques are available, such as tripod polishing and ion milling. Non-conducting specimens, e.g. rocks and insects, must be coated with gold or another inert metal to avoid charge build-up at their surface [112].

3.3   Muon spin relaxation (µSR)

This technique applies knowledge about elementary particle physics to the extraction of information about nanometre-scale magnetic fields inside materials. Being probes of small magnetic fields, muons find the most applications within magnetic materials [113] and superconductors [114], but they have also been used to study semiconductors, biological molecules, and so forth, as muon diffusivity [115, 116] and electronic influence on the material [117–119] can be measured. The R in the acronym µSR can stand for rotation, relaxation, resonance, or research, while the first two letters always

stand for muon spin. In this thesis, the R always means relaxation. The following statement is from a 1957 paper by µSR pioneers Garwin, Lederman and Weinrich [120], and served as an accurate prediction:

> It seems possible that polarized positive and negative muons will become a powerful tool for exploring magnetic fields in nuclei, atoms and interatomic regions.

The motivation for starting a study on Al alloys using µSR was mainly the success of the related technique PAS in probing the kinetics of vacancies and clusters in Al–Mg–Si alloys (see section 3.4). We have found strengths and weaknesses of both methods, and that µSR has much to offer for the investigation of microstructural states in Al alloys, as elaborated on in section 3.3.5. The theory in the following sections is highly condensed and not recommended for bedtime reading. For a more complete description, see e.g. [121].

3.3.1 The muon

The muon is an elementary particle in the lepton family, one generation up from electrons. It has unit charge and spin 1/2, 207 times the mass of an electron and a much smaller magnetic moment. They are produced in high-energy particle collisions, such as those occurring when cosmic radiation hits our atmosphere. Being unstable particles, they only reach the surface of Earth because of relativistic length contraction.

For scientific applications, muons are produced by proton–proton collisions. Protons are accelerated in a cyclotron/synchrotron and directed at a target consisting of an inert non-metallic solid. Pions, a type of mesons, are produced by a nuclear reaction. A pion decays into a muon and a neutrino after 26 ns:

$$\pi^+ \rightarrow \mu^+ + \nu_\mu. \tag{3.3}$$

Positive particles are displayed as muon techniques most often use positive muons. Because of CP violation[3], neutrinos are always left-handed[4]. Spin conservation necessitates the muons to also be left-handed, that is, to have their spin antiparallel to their direction of motion. From the pion decays,

---

[3]C and P refers to charge conjugation and parity symmetries. According to C, if you transform all matter into antimatter, the Universe would look the same. P says the same about inverting (mirroring) the Universe about a point. These are both untrue. The combined operation CP also does not leave the Universe unchanged, which is why µSR works. Read more in e.g. [122]

[4]Velocity vector given by your left thumb, spin direction given by curling your fingers around it.

we therefore get a spin-polarised beam of muons. This beam is directed into the material with electromagnets.

Positive muons decay to positrons after a material-independent lifetime with average value of 2.197 μs [123]:

$$\mu^+ \rightarrow e^+ + \nu_e + \bar{\nu}_\mu. \tag{3.4}$$

The decay is asymmetric, meaning that the velocity of the positron is not distributed uniformly over all directions. The probability of emission in a certain direction depends on the angle θ between this direction and the muon spin vector:

$$p(\theta) = 1 + A\cos\theta. \tag{3.5}$$

The constant A is the asymmetry of the decay, which is dependent on the energy of the positron. Its theoretical value, averaging over all possible energies, is $1/3$. The energy of the positron is continuously distributed from 0 to half of the muon rest energy, $m_\mu \approx 53$ MeV, because of energy and momentum conservation in the three-body decay. The property of asymmetric decay, also caused by CP violation, is what makes muon methods useful.

3.3.2 Theory of μSR

The raw data of μSR is the positron counts in the annular forward and backward detectors, N_f and N_b, at a certain time t after muon implantation. From this we may find the spin asymmetry $G_z(t)$, often normalised and expressed in terms of the *relaxation function*, $g_z(t)$:

$$G_z(t) = Ag_z(t) = \frac{N_\mathrm{f}(t) - \alpha N_\mathrm{b}(t)}{N_\mathrm{f}(t) + \alpha N_\mathrm{b}(t)} \tag{3.6}$$

The z is denoting that the longitudinal (parallel to the initial spin) polarisation is measured. The parameter α corrects for the sample not being positioned exactly in the middle of the two detectors.

Instead of going through the material or somehow reacting with other elementary particles, the positive muon stops in the bulk of the sample. It undergoes inelastic scattering processes and loses almost all its energy in a time that is much shorter than its lifetime. Thermalisation then occurs: The energy of the muon is determined by the sample temperature, and it diffuses interstitially in the crystal structure like a small atom would.

The spin of a muon precesses in the presence of magnetic fields. Electrons cause the strongest magnetic fields in a metal, but vary at a too high frequency to affect muon spins [124]. On the other hand, the fields set up by

atomic nuclei are measurable by μSR. The field affecting a given muon equals the sum of the fields generated by all nearby nuclei. A three-dimensional Gaussian distribution is often used as a good model of local magnetic fields in non-magnetic solids. A Gaussian is appropriate because the field is the sum of many small numbers, such that the central limit theorem (see e.g. [125]) applies. Assuming uncorrelated Gaussian fields and a static muon, we obtain as our relaxation function the Kubo–Toyabe (KT) function [126]:

$$g_z^{\mathrm{KT}}(t) = \frac{1}{3} + \frac{2}{3}(1 - \Delta^2 t^2)e^{-\frac{1}{2}\Delta^2 t^2}. \tag{3.7}$$

This equation is the standard starting point for fitting and data analysis of most longitudinal μSR data. An important parameter has been introduced: the *dipolar width* Δ, which is proportional to the strength of local magnetic fields. The static KT function is found not to fit all data for Al–Mg–Si alloys. A better fit is the dynamic KT function. It is found by solving an integral equation [127], taking into account that muons are not static, but jump between different sites. This introduces a change in the local magnetic field. The strong-collision model [124] assumes that this change is immediate and happens with a fluctuation rate ν. One then obtains

$$g_z^{\mathrm{DKT}}(t) = e^{-\nu t}g_z^{\mathrm{KT}}(t) + \nu \int_0^t g_z^{\mathrm{DKT}}(t - t')g_z^{\mathrm{KT}}(t')e^{-\nu t'}\mathrm{d}t'. \tag{3.8}$$

This integral equation can be solved by iterative methods. To summarise the KT approach, the muon may move through a material by thermally activated diffusion, and by finding how correlated the magnetic fields are in time, we can find out how fast the muon is moving (measured with ν), and thereby what kind of environment we have inside the material. Unfortunately, the dynamic KT function is also insufficient to consistently describe the kinetics in both dense and dilute Al alloys. This made us resort to numerical simulations, which are described in section 3.3.4.

3.3.3 μSR at the RIKEN-RAL muon facility

The experiments described in papers 1 and 2 were conducted at the RIKEN-RAL muon facility [128] in Oxfordshire, UK. It is an international collaboration between the RIKEN institute in Japan and Rutherford Appleton laboratory (RAL), which hosts the proton synchrotron ISIS [129]. ISIS has a circumference of 163 metres, and accelerates protons to energies of 800 MeV. The protons are divided into bunches, with 40 bunches being sent out of the synchrotron per second. The proton beamline is used for producing both

neutrons and muons, which are used for research on a wide variety of materials. A proton current of about 150 µA goes through the carbon-based muon production target, losing only 7% of the protons through collisions, and moves on to the tungsten-based neutron production target. This allows for several experiments to be carried out at the same time using only one proton beam.
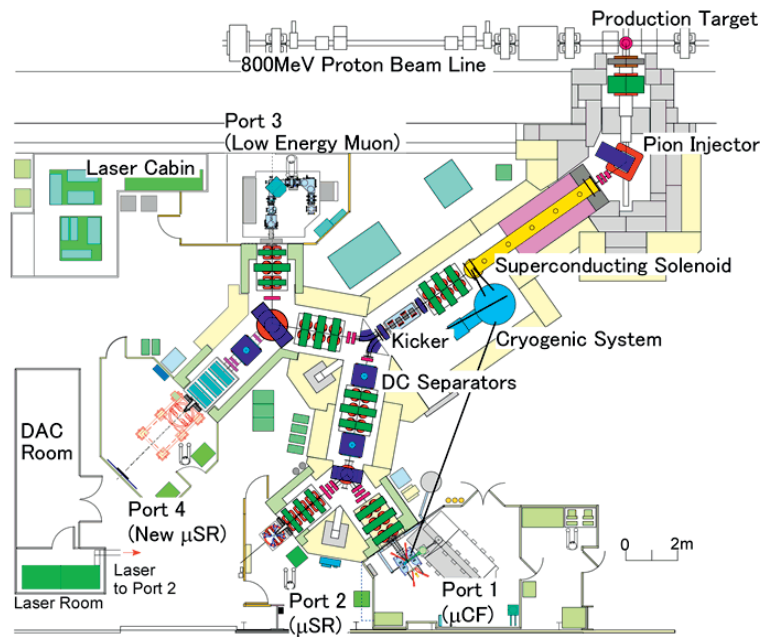
Figure 3.9: An overhead map of the RIKEN-RAL muon facility. The muon beam can be directed to four ports for different applications. The ARGUS spectrometer, seen in Fig. 3.10, is located at Port 2.

Figure 3.9 shows a map of the RIKEN-RAL facility [128]. Our data on aluminium alloys was obtained using the Advanced Riken General-purpose mUsr Spectrometer, ARGUS, depicted with the author in Fig. 3.10. Since the protons from the synchrotron are sent out in discrete bunches, the resulting muon beam is pulsed. Each pulse contains $1–2 \cdot 10^4$ muons, of which about 440 give events recorded by ARGUS. This gives roughly 60 million events per hour. One hour is the typical running time for an experiment at one fixed sample temperature. Our normally conducted experiment type involved cooling a sample down to 20 K with a helium cryostat and then heating it stepwise to 300 K. The relaxation function was measured at 10–20 temperature points to probe the muon kinetics in a wide range of
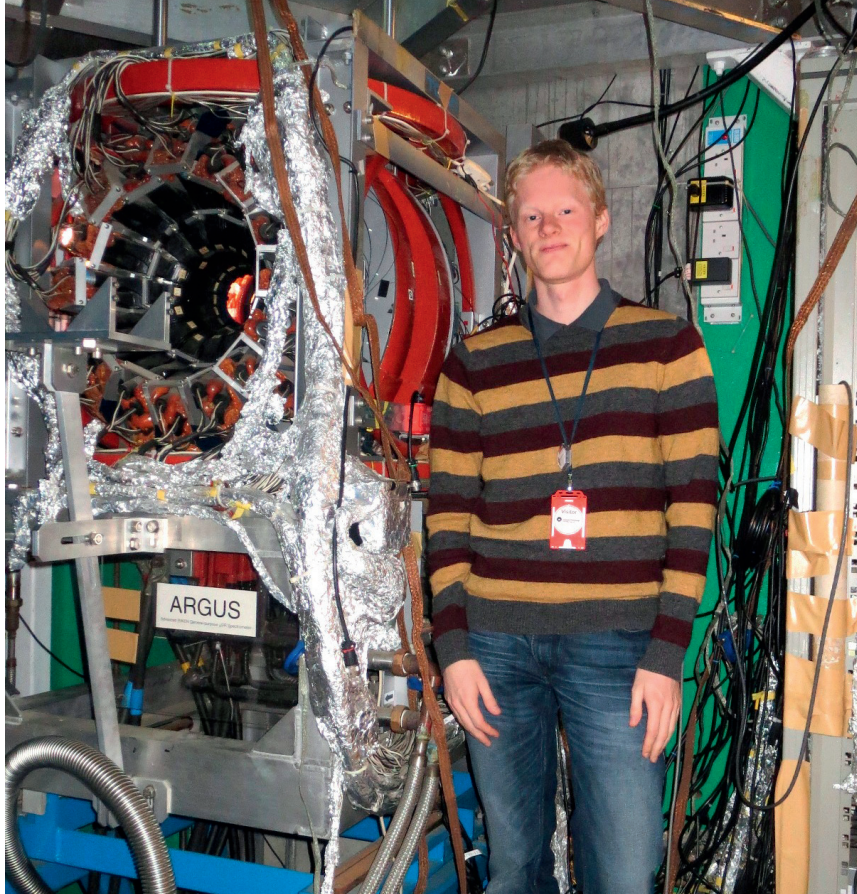
Figure 3.10: Photo of ARGUS and the author, October 2012.

temperatures.

Correction coils in the spectrometer nullify the magnetic field of the Earth and that of the nearest quadrupole magnet in the muon beamline. The resulting residual field is ~ 5 µT, which is negligible in comparison to typical local fields in Al, ~ 1000 µT.

The forward and backward positron detectors consist of 192 individual plastic scintillators. They are shaped as longitudinal sections of a hollow sphere, and have a summed solid angle coverage of 25% (a quarter-sphere). They are configured to most preferably detect high-energy positrons, as these show the highest degree of decay asymmetry A [see Eq. (3.5)]. ARGUS measures an average asymmetry of $A \approx 0.25$. The parameter α in Eq. (3.6)

is calibrated by muon spin *rotation*. This involves applying an external magnetic field perpendicular to the incident muon direction. Muon spins precess around this field with a frequency proportional to the field strength. The spin asymmetry in Eq. (3.6) now appears as a cosine function with respect to time. If there is any spin relaxation, the amplitude of this function also diminishes with time. The calibration procedure is setting α to the value which makes the cosine function oscillate about zero, and using this α value for all μSR spectra measured with the same sample. For an unknown reason, the procedure gave a faulty α value for our two very first μSR measurements. This lead to publication of erroneous results for the conditions 1.6-15d and 1.6-100C in paper 1, which were compensated for in paper 2 by assuming the initial asymmetry [$G_z(0)$ in Eq. (3.6)] to be approximately the same for all samples.

3.3.4   Simulations

The dynamics of muons can be modelled to calculate theoretical relaxation functions. We assume a two-state model, where the muon occupies either a free diffusion state or a trapped state. Transitions between these states, as well as diffusion in the Al matrix, are controlled by thermodynamics. For simplicity, we assume that a single type of trapping site dominates at a given temperature. The average diffusion rate as used in the KT model can then be decoupled into three values: the pure material jumping rate ν, the trapping rate ν_t and the detrapping rate ν_d. These rates are assumed constant throughout an experiment. However, the fraction of muons which are trapped are not necessarily constant as it may take some time to achieve equilibrium. We introduce another parameter, the initial fraction of trapped muons, p_0. The solution to the two-state model with constant transition rates can easily be obtained analytically. The fraction of trapped muons at some time after implantation t is

$$p(t) = \frac{\nu_t}{\nu_t + \nu_d} - \left(\frac{\nu_t}{\nu_t + \nu_d} - p_0 \right) e^{-(\nu_t + \nu_d)t}. \tag{3.9}$$

The spin relaxation of the ensemble of muons is more tricky to calculate, which forces us to leave the analytical approach behind.

Spin precession is calculated using matrix operations, as the spin can be represented by a three-dimensional vector $\mathbf{s}$. The operation becomes

$$\mathbf{s}_{new} = \mathbf{R}^T \mathbf{P} \mathbf{R} \mathbf{s}_{old}, \tag{3.10}$$

where $\mathbf{P}$ is the spin precession matrix and $\mathbf{R}$ makes the rotation axis parallel to the magnetic field. This operation must be performed at each muon

trapping site. As mentioned in [116], muon diffusion in the matrix is so fast that spin relaxation is negligible there, so this formula is not applied to free (non-trapped) muons. The spin precession matrix has the following form:

$$\mathbf{P} = \begin{pmatrix} \cos \omega t & \sin \omega t & 0 \\ -\sin \omega t & \cos \omega t & 0 \\ 0 & 0 & 1 \end{pmatrix}, \tag{3.11}$$

where $\omega = \gamma_\mu \|\mathbf{B}\|$ is the precession frequency. As in the KT approach, the magnetic field is generated by a Gaussian distribution with standard deviation Δ/γ_μ, where $\gamma_\mu = 8.5168 \times 10^8 \text{ T}^{-1}\text{s}^{-1}$ is the gyromagnetic ratio of the muon.

While the muon is diffusing around inside the material, there is a constant probability per time λ that it will decay to a positron which leaves the material. Consequently, the lifetime of each muon τ follows an exponential distribution:

$$P(\tau) = \lambda e^{-\lambda \tau}. \tag{3.12}$$

When the time τ is reached, the direction of positron emission is determined by Eq. (3.5). Time is split into time bins, and for the bin τ belongs to, we increment the positron count in the forward or backward hemispheres [$N_\text{f}(\tau)$ or $N_\text{b}(\tau)$] depending on the angle θ. The relaxation function is then calculated using Eq. (3.6), with $\alpha = 0$.

The changes in the relaxation function due to movement and trapping of muons are very subtle. A complicated variation with the four trapping parameters Δ, ν_t, ν_d and p_0 is observed. Information about the dynamics is thus hard to extract, and the estimated quantities will have a low accuracy. However, we currently see this as the best method for analysis. We constructed a database of simulated relaxation functions with varying simulation parameters, and calculated least square fits between simulated and experimental functions to find the parameters that best describe the experimental data.

3.3.5 Application to Al alloys

Some μSR research on aluminium alloys were conducted in the late 1970s and early 1980s. They considered mostly ultra-pure Al with very small amount of some common alloying element, such as Mg, Si, Cu, Mn and Ag [8, 9]. Powerful cryostats were used to cool samples to the millikelvin range, and effects of the added elements were apparent in a wide temperature range. It is thus possible to detect very small quantities of trace elements by observing changes in relaxation functions, although the exact nature of the interactions

between muons and the defects remains unknown, despite the application of sophisticated quantum mechanical models. It was also found that muons are trapped by vacancies [9] and dislocations [130]. To our knowledge, heat-treatable alloys with varying heat treatments were not studied with µSR before our experiments at the RIKEN-RAL facility.

Some technical details about muon behaviour in Al follows. In a para-magnetic material such as Al[5], muons give information about local magnetic fields and how fast these are changing. The strength of magnetic fields created by atomic nuclei depends on the nuclear isotope. As seen in Table 3.1, Al nuclei set up much stronger fields than Mg and Si nuclei. If no nuclear spins are correlated, this means that there are stronger magnetic fields in the Al matrix than in solute-rich areas such as clusters and precipitates. The

Table 3.1: Nuclear magnetic dipole moments of relevant isotopes [15]. The nuclear magneton is $\mu_N = e\hbar/2m_p = 5.05078 \cdot 10^{-27}$ Am^2, where m_p is the proton mass.

Isotope	Abundance	Spin parity	Magnetic dipole moment
^{27}Al	100%	$5/2^+$	$3.6415069\mu_N$
^{24}Mg	78.99%	0^+	0
^{25}Mg	10.00%	$5/2^+$	$-0.85545\mu_N$
^{26}Mg	11.01%	0^+	0
^{28}Si	92.23%	0^+	0
^{29}Si	4.683%	$1/2^+$	$-0.55529\mu_N$
^{30}Si	3.087%	0^+	0

preferred muon site in Al is an interstitial position, in particular a tetrahedral site at temperatures above ≈ 15 K [131]. Attempts were made to estimate the dipolar width Δ in fcc Al from first principles, and determine the effect on Δ by replacing a few Al atoms by Mg or Si. The value for pure Al was calculated to $\Delta = 0.495$ µs^{-1}, which decreases with an increasing solute fraction. The value typically found in our Al alloys was $\Delta = 0.3$ µs^{-1}, while pure Al gave $\Delta = 0.1$ µs^{-1}, inconsistent with the trend found by the calculations. Conclusively, the simple approach of considering only uncorrelated nuclear dipole fields is not sufficient to describe the physics in our samples. We thus abandoned this approach and resorted to empirical determinations of the dipolar width, treating it as an adjustable parameter.

The simulation method described in section 3.3.4 was used to analyse trends in defect concentrations in papers 1 and 2. The papers contain plots

---

[5]Embarrassingly, it is mentioned as a diamagnetic material in paper 1, but the important thing is that Al is not (anti)ferromagnetic.

of the temperature variation of the four simulation parameters. We reasoned that the most important of these are the trapping rate ν_t, which should have a peak when muons are trapped by a specific defect. Our full interpretation of the observed peaks is discussed in section 4.4.

3.4 Positron annihilation spectroscopy (PAS)

3.4.1 The positron

The positron (e^+) is the antiparticle of the electron. It has the same mass, charge (although opposite) and spin. Apart from being a decay product of muons, it is most easily produced by inverse beta decay in a radioactive source. In the sodium chloride source used in our experiments, the nuclear decay looks like this:

$$^{22}\text{Na} \rightarrow e^+ + \gamma + \nu_e + {}^{22}\text{Ne}. \tag{3.13}$$

Unlike the positive muon, the positron has a lifetime which is highly dependent on its environment. This is because it is stable in vacuum, but annihilates with electrons once it has the chance. The most common annihilation process creates two gamma photons:

$$e^+ + e^- \rightarrow \gamma + \gamma. \tag{3.14}$$

3.4.2 Technique

Positron annihilation spectroscopy (PAS) comes in several forms. Information about a material can be gained from the properties of the photons produced by the positron–electron annihilation, such as their velocity difference, emission angles or lifetimes [132]. The technique we briefly used has the acronym PALS, where L stands for lifetime. A description of a measurement procedure follows and is depicted in Fig. 3.11.

- Positrons are generated by the radioactive decay shown in Eq. (3.13). The radioactive source is sandwiched between two samples of material, to cover all possible positron emission angles. The high-energy (1.27 MeV) photon produced in the decay is used as a "start signal".

- The positrons enter the samples and are thermalised by Bremsstrahlung and inelastic scattering. Diffusion and trapping start.

- Positrons annihilate with electrons at a rate proportional to the electron density at their site. Most often, two photons are produced, as in Eq. (3.14). These will have energies of 511 keV each.

- One of the annihilation photons is detected, giving the "stop signal". The positron lifetime is then the time between the two signals. This "stop" photon is rarely detected at the "start signal" detector because its energy is not sufficient for passing through a lead block put in front of it.
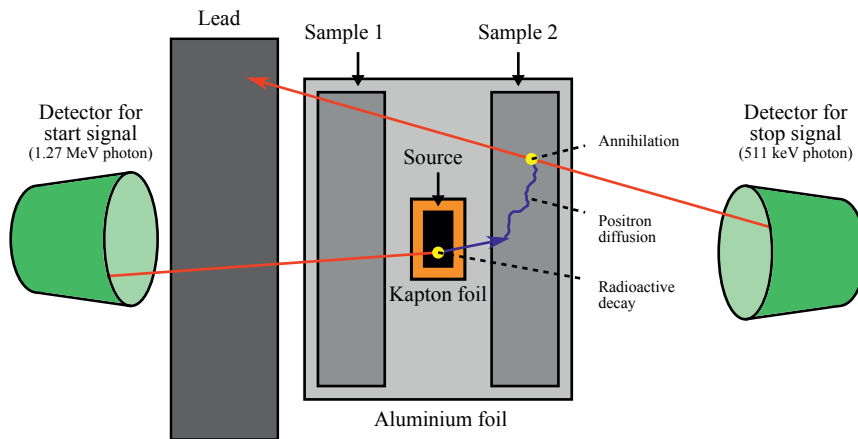

Figure 3.11: Positron annihilation lifetime spectrometer (PALS) setup.

You might wonder why positrons do not simply leave the material, like the positrons produced by muon decay in μSR, but the positrons produced by inverse beta decay are typically of much lower energies and thermalise instead. Kapton or aluminium foils surrounding the samples block low-energy photons related to positron–sample interactions. In the setup we used at Helmholtz-Zentrum Berlin [133], the detectors were scintillators coupled to sodium iodide light collectors and photomultiplier tubes. A scintillation detector generally gives a good time resolution and is therefore used for PALS, where lifetimes are measured.

3.4.3   What happens in the material

Positrons are trapped by nano-sized crystallographic defects, like e.g. vacancies. A trapping model similar to improved KT models for muon kinetics can be used, although we do not have to worry about spin precession in this case. The fraction of trapped positrons can thus be calculated analytically, e.g. with Eq. (3.9).

Annihilation, like radioactive decays, has a constant probability of happening at each point in time, making it a Poisson process. The annihilation

rate for an ensemble of positrons at a certain trapping site follows an exponential distribution with mean values $\lambda = 1/\tau$, where τ is the mean lifetime. The total measured spectrum will include contributions for all possible positron sites s with fractional occupancy I_s and annihilation rate λ_s:

$$S(t) = \sum_s I_s e^{-\lambda_s t}. \tag{3.15}$$

In *in situ* experiments, fitting the spectrum to a sum of several unknown components is infeasible due to low statistics. However, corrections for annihilation in the radioactive source and in bulk Al is possible if the relevant annihilation rates are known.

There has been many studies of clustering and precipitation in Al alloys with PAS [49, 134]. Several distinct clustering stages during NA and AA of Al–Mg–Si alloys have been identified [48], and results have also been used to estimate solute–vacancy bond energies [135].

3.5   Hardness and conductivity measurements

Mechanical strength is the most important desirable property of aluminium alloys, hence it must be quantified. Tensile stress tests are optimal for this as they quantify both strength and brittleness through the flow stress and yield stress. Measuring surface hardness by microindentation is an alternative method which is quicker and more flexible regarding sample size.

The Vickers hardness test uses a diamond pyramid as the indenter. Figure 3.12 shows a typical impression. The hardness H_{V} is estimated from the diameters of the impression of the material, d. It is given by the formula

$$H_{\mathrm{V}} = \frac{2F \cos\left(22^\circ\right)}{d^2}, \tag{3.16}$$

where F is the downward force in kg and 22° is the angle of the tip relative to the surface of the material. The diameters can be measured either manually or automatically, depending on the hardness tester.

A Matsuzawa DVK-1S machine was used in paper 3 to measure the hardness of Al–Mg–Si(–Cu) alloys with different NA time. This gave variations of ≈ 5 kg/mm^2, while the typical measurement error, averaged over 10 indentations, is ≈ 2 kg/mm^2. Paper 4 used the same method to document the decrease of strength with Ca content in Al–Mg–Si alloys, using a Struers DuraScan-70 machine.

Also measured in the work of paper 4, but not published, were conductivity measurements. Like hardness measurements, these are quick and
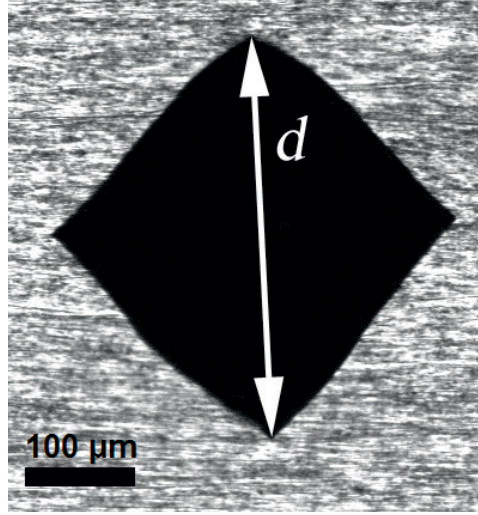
Figure 3.12: Impression by a Vickers hardness indenter on a naturally aged Al–Mg–Si sample. The two diagonals are equal if the material is sufficiently homogeneous.

easy to conduct and can be done *in situ* during NA. There are essentially two ways to measure conductivity of bulk materials. The method used for the Ca-containing alloys relies on eddy currents induced in the material by a rapidly changing magnetic field. The alternative four-contact method is more tedious, but ensures more accurate results. In both cases, it is very important to maintain a constant temperature and humidity near the sample to avoid systematic errors. Conductivity is mostly used to study clustering kinetics: elements in solid solution lower the conductivity, but when they form clusters or larger particles, areas with a lower solute content appear, which makes the conductivity recover towards the value for pure Al.

3.6   Techniques that were not used

With the many techniques used by my colleagues and sometimes referred to in this thesis, some explanations are appropriate. One important example is electron diffraction, which was used exclusively to tilt TEM specimens to the $\langle 001 \rangle_{Al}$ zone axes. In itself, diffraction is a powerful technique for structure determination, with a far better ability to accurately estimate lattice parameters than direct electron imaging. For large particles embedded in the Al matrix (e.g. dispersoids) it is used for finding orientation relationships [136]. This can also be done for coherent precipitates, but one then requires

a very small electron probe. The method of choice is nanobeam diffraction (NBD), which contrary to CBED uses a tiny, parallel electron beam. It was used together with corresponding NBD simulations and DFT calculations to find the structure of many (ordered) post-β'' phases [62, 64, 137].

Atom probe tomography (APT), also called 3-dimensional atom probe (3DAP), is an advanced analytical technique that was developed in the early 1980s [138]. Material is prepared in the shape of a thin needle by electro-polishing. It is placed in vacuum and cooled down, and an electric field or a laser is used to cut loose ("evaporate") atoms one by one from the specimen. As a result, the atoms are ionised, and fly trough an electric field until they hit a detector. The position and time of flight is calculated, which enables the determination of atomic species. When the entire needle is destroyed by the atom probe, it can be reconstructed to a 3D model on a computer. The advantage over TEM is the introduction of one more spatial dimension, and the disadvantage is a poorer spatial resolution. In addition, APT can not detect all atoms that hit the detector, but rather approximately half of them. Lattice planes can be visible in an APT volume, but the technique can not be used for structure determination of precipitates. It can however estimate the composition of a phase [63], and be used for statistical analysis of solute clusters [50–52]. In this way, the technique is complimentary to TEM.

Differential scanning calorimetry (DSC) is simple in principle: heat a sample with a constant rate of temperature increase, and measure how much heat goes into or out of the sample. This is very useful for studying phase transitions, and is in common use for heat-treatable alloys [139, 140]. A DSC apparatus has two chambers, one for the sample of interest and another for a reference sample. The reference is usually pure aluminium if Al alloys are studied. When heated to typical precipitation temperatures, the alloy will absorb less heat than pure Al, because an energy minimum is reached when solute atoms start forming metastable structures. Correspondingly, the alloy will absorb less heat when the precipitates dissolve. Figure 2.12 shows a typical DSC curve for an Al–Mg–Si alloy. The technique has been used to estimate the formation enthalpy of precipitate phases and investigate the kinetics of clustering during NA for various Al–Mg–Si alloys [46, 47, 141].

The last method I want to mention is a theoretical one, density functional theory (DFT). It solves the Schrödinger equation with some approximations to find the energy of a collection of atoms [142, 143]. Periodic boundary conditions can be applied, which makes DFT the most successful quantum mechanical approximation method for the case of periodic solids. Most DFT software for molecules and solids include relaxation algorithms that move the

nuclei in the structure slightly, calculate the wave functions of surrounding electrons, and check which configurations have the lowest energy, step by step. In this manner, one can e.g. check the relative stabilities of different precipitate structures, compare them with experimentally found structures and check how the unit cell dimensions are affected by chemical composition [65, 70, 77].

Part II

Papers

Paper 1

Probing defects in Al–Mg–Si alloys using muon spin relaxation

S. Wenner, R. Holmestad, K. Matsuda, K. Nishimura, T. Matsuzaki,
D. Tomono, F. L. Pratt and C. D. Marioara

Probing defects in Al-Mg-Si alloys using muon spin relaxation

Sigurd Wenner[*] and Randi Holmestad
Department of Physics, NTNU, Høgskoleringen 5, Trondheim NO-7491, Norway

Kenji Matsuda and Katsuhiko Nishimura
Department of Materials Science and Engineering, University of Toyama, Gofuku 3190, Toyama-shi, Toyama 930-8555, Japan

Teiichiro Matsuzaki and Dai Tomono
Advanced Meson Science Laboratory, RIKEN Nishina Center for Accelerator Based Science, RIKEN, Wako, Saitama 351-0198, Japan

Francis L. Pratt
ISIS Facility, Rutherford Appleton Laboratory, Chilton OX11 0QX, United Kingdom

Calin D. Marioara
Materials and Chemistry, SINTEF, Box 4760 Sluppen, Trondheim NO-7465, Norway

Muon spin methods are very sensitive to nanoscale defects such as trace elements and vacancies in metals. This sensitivity is required when investigating Al-Mg-Si alloys, a complicated system in which diffusion-controlled phase transformations are responsible for the most important hardening mechanisms. We present muon spin relaxation experiments conducted on Al-Mg-Si alloys at measurement temperatures in the range 20–300 K. Varying the alloy composition and heat treatment, we find differences in muon depolarization in several temperature regimes. This reflects differences in concentration of several types of muon-trapping defects. We identify free solute atom and vacancy regimes, and confirm that the concentration of these defects decreases when an alloy is annealed at low temperature. We further attribute one regime to Mg-Si vacancy clustering, a mechanism required for precipitation hardening during aging. After storage at room temperature, muon trapping in this regime is more pronounced for a Mg-rich alloy than a Mg-Si-balanced alloy.

I. INTRODUCTION

Muon spin methods have been used for probing the microscopic properties of a wide range of materials, including superconducting and magnetic materials,[1–3] biological molecules,[4] and semiconductors.[5,6] Most of the research activity using muons on aluminium and other pure metals took place in the late 1970s and early 1980s.[7–9] In nonmagnetic materials, polarized positive muons (μ^+) can be used as probes for atomic-scale magnetic fields. The methods have been proven very sensitive to point defects such as trace element atoms.[8,10] The property of muons known as *asymmetric decay* is central to how the measurements are conducted: Muons are unstable and decay to positrons, whose directions of motion tend to be parallel to the muon spin. The detection of these positrons enables us to follow the time evolution of the average muon polarization inside the material. In this paper, the acronym μSR refers to *muon spin relaxation*, with which no external magnetic field is applied.

Aluminium alloys containing Mg and Si as main alloying elements (6xxx series alloys) are used extensively as structural materials due to their formability, mechanical strength, and corrosion resistance. These alloys are heat-treatable, which means that their microstructure changes when thermal and mechanical treatment is applied to them. Typically, 6xxx alloys are given a solution heat treatment (SHT) before subsequent aging, to distribute the solute elements evenly in the Al matrix and to introduce a high concentration of

vacancies, which is necessary for later substitutional diffusion of the solute elements. A unique feature of Al-Mg-Si alloys is that room temperature (RT) storage between SHT and artificial aging (AA) at higher temperatures has a significant effect on the hardness of the material.[11,12] This effect is called *natural aging* (NA) and can degrade the mechanical properties of dense alloys (with solute content above 1%).[11,13] NA is caused by the clustering of solute atoms.[14,15] Upon aging above ≈150 °C, metastable phases with well-defined crystal structures precipitate in the Al matrix.[16] The processes of clustering and precipitation are very sensitive to parameters such as alloy composition, storage time, aging temperature, and heating/cooling rates.

We have applied μSR to samples of Al-Mg-Si alloys with various compositions and heat treatments. The evolution of the muon polarization is measured at a range of temperatures, as the trapping of muons by nanometer-sized defects is temperature dependent. This enables the estimation of properties of several types of defects as averaged over a macroscopic volume of the material under study. To our knowledge, measurements of this kind have not before been conducted on aluminium alloys.

This paper presents results from μSR studies of alloys with typical industrial Mg and Si content. Section II reviews the theoretical background of μSR and muon diffusion in nonmagnetic materials. Section III gives the experimental methodology as well as the compositions and heat treatments of the samples. In Sec. IV we explain how the experimental

data is treated and introduce the simulations used to estimate quantities associated with muon diffusion. The results of these estimations are presented in Sec. V, while Secs. VI and VII are dedicated to discussion and summary of the central findings.

II. THEORY OF μSR

When a spin-polarized high-energy muon enters a metallic solid, inelastic scattering processes quickly reduce its energy to a thermal level, while retaining the muon spin. In analogy with hydrogen atoms, muons occupy interstitial sites in metals. The magnetic field at the muon site causes Larmor precession of the muon spin. In the absence of an external field, the precession is induced exclusively by small ($\sim$1 mT) local magnetic fields inside the material. The dynamics of μSR can be decoupled into spin relaxation (depolarization) by these fields and muon diffusion.

An atomic nucleus sets up the dipole field[17]

$$\mathbf{B}(\mathbf{m},\mathbf{r}) = \frac{\mu_0}{4\pi r^3} \left[3(\mathbf{m} \cdot \hat{\mathbf{r}})\hat{\mathbf{r}} - \mathbf{m} \right], \qquad (1)$$

where $\mathbf{m}$ is the magnetic moment of the nucleus, $\hat{\mathbf{r}}$ is a unit vector pointing from the muon to the nucleus, and μ_0 is the electrical permittivity of vacuum. There are other sources to local magnetic field contributions inside metals, such as the quadrupole moment of nuclei and both core and conduction electrons.[17] Inside a diamagnetic material, the total field from electrons gives spin relaxation times longer than 100 μs, which is much greater than the lifetime of a muon.[17,18] The nuclear dipole moments are thus the greatest contributions.

A positive muon has an average lifetime of 2.197 μs. Its main decay channel produces one positron and two neutrinos through an asymmetric decay. The probability for the positron to be emitted at an angle θ from the muon spin is

$$p(\theta) = 1 + A\cos\theta, \qquad (2)$$

with A being the asymmetry of the decay, which depends on the energy of the emitted positron. In experiments, $A \approx 0.25$ is normally measured. In the present μSR experiments, muons are polarized antiparallel to their direction of motion. Two detectors are placed in the forward (parallel to the initial polarization) and backward direction, and the positron counts, N_{f} and N_{b}, are measured at a range of times t after muon implantation. From this we find the muon spin asymmetry $G(t)$, often expressed through the longitudinal *relaxation function* $g(t)$,

$$G(t) = Ag(t) = \frac{N_{\mathrm{f}} - \alpha N_{\mathrm{b}}}{N_{\mathrm{f}} + \alpha N_{\mathrm{b}}}. \qquad (3)$$

The parameter α compensates for differences in distance between the sample and the two detectors.

The Kubo-Toyabe (KT) model[19] gives a simple and often accurate picture of the dynamics of μSR. The model assumes a Gaussian distributed magnetic field at the muon site. Averaging over an ensemble of muons with an exponentially distributed lifetime, one obtains the static KT relaxation function,

$$g^{\mathrm{KT}}(t) = \tfrac{1}{3} + \tfrac{2}{3}(1 - \Delta^2 t^2)\exp\left(-\tfrac{1}{2}\Delta^2 t^2\right), \qquad (4)$$

where we have introduced the *dipolar width* $\Delta = \gamma_\mu B_{\mathrm{RMS}}$, a product of the gyromagnetic ratio of the muon $\gamma_\mu = 8.5168 \times 10^8$ T^{-1}s^{-1} and the root-mean-square magnetic field strength B_{RMS}. The effect of diffusion on $g(t)$ is an important one, as *motional narrowing*[17] of the field distribution decreases the depolarization rate. At temperatures above $\sim$1 K, the muon diffuses interstitially by a phonon-assisted tunneling process.[17] This is well described by the strong-collision model, in which muon jumps happen instantly and the magnetic field is uncorrelated between adjacent interstitial sites.[18] This leads to the dynamic KT relaxation function, computed by solving an integral equation.[20] Faster dynamics will shift the KT minimum to longer times.[21] In the limit of fast diffusion, this function can be approximated by

$$g^{\mathrm{DKT}}(t) \approx \exp\left(-\frac{2\Delta^2}{\nu}t\right), \qquad (5)$$

where ν is the muon hopping rate. In certain circumstances, Δ^2/ν is so small for freely diffusing muons that the depolarization becomes negligible.[10]

Trapping by lattice defects can prevent muons from diffusing, introducing another complication to the dynamics. The fraction of time a muon spends trapped inside the material, f_{t}, will greatly influence $g(t)$. We have derived this quantity from a two-state stochastic trapping-detrapping model. When averaged over the lifetime of a muon, the trapped time fraction becomes

$$f_{\mathrm{t}} = \frac{\nu_{\mathrm{t}}}{\nu_{\mathrm{t}} + \nu_{\mathrm{d}}} - \left(\frac{\nu_{\mathrm{t}}}{\nu_{\mathrm{t}} + \nu_{\mathrm{d}}} - p_0\right)\frac{\lambda}{\nu_{\mathrm{t}} + \nu_{\mathrm{d}} + \lambda}, \qquad (6)$$

where ν_{t}, ν_{d}, and λ are the (constant) trapping, detrapping, and decay rates, and p_0 is the fraction of initially trapped muons. From the theory of diffusion-controlled trapping, we have that ν_{t} is proportional to the concentration of muon-trapping defects,[22] while ν_{d} depends on how tightly the muon is bound to the defects. The equilibrium trapped time fraction (for muons of infinite lifetime) would be $\nu_{\mathrm{t}}/(\nu_{\mathrm{t}} + \nu_{\mathrm{d}})$.

Inside a material analyzed by μSR, the concentration of muons is extremely low at all times. Muons behave as light protons in Al, and are expected to have a negligible influence on the diffusion of vacancies and solute atoms during experiments of any duration. In nonmetallic materials, bound muon-electron systems (muonium) have been used as a model for hydrogen atoms with accompanying diffusion and bonding properties.[5,6,23]

III. EXPERIMENTAL

The μSR experiments were conducted at the RIKEN-RAL Muon Facility in Oxfordshire, UK.[24] Its pulsed muon beamline provides a high intensity which gives about 1 million positron counts per minute. Figure 1 shows a schematic of the muon spectrometer. Compensation coils surrounding the sample are used to counter the magnetic field of the Earth and the last quadrupole magnet in the muon beamline. The residual field is $\sim$5 μT, well below the magnitude of typical local fields in Al, $\sim$1000 μT. The annular forward and backward detector arrays each have a 25% solid angle coverage. For each sample, the α parameter in Eq. (3) was estimated by *muon spin rotation* experiments using external transversal fields of 2.0–3.0 mT.
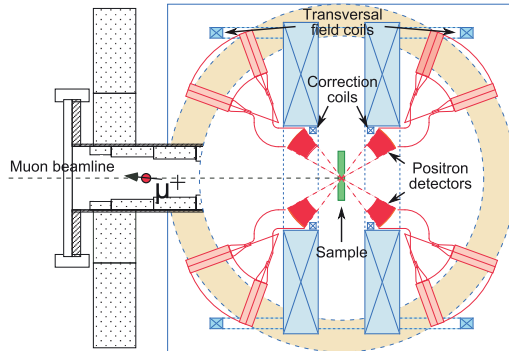
FIG. 1. (Color online) The experimental setup, showing the AR-GUS muon spectrometer and a spin-polarized muon beam entering from the left.

The samples used were of pure aluminium (99.99%) and three different ultrapure Al-Mg-Si alloys. Two of the alloys had an Mg/Si ratio of 2 and total atomic solute 1.6% and 1.0%, while the third alloy was Mg-Si balanced and contained a total of 1.4% solutes. Many industrial 6xxx alloys contain comparable amounts of Mg and Si, with Fe, Mn, Cu, and other elements added in smaller amounts. All samples were given a SHT at 575°C for 1 hour, ensuring an even distribution of solutes in solid solution. We quenched the samples in ice water before directly applying further heat treatments. Table I summarizes the conditions of the 11 samples used. Similar conditions have been studied extensively using various characterization methods such as atom probe tomography (APT),[25] positron annihilation spectroscopy (PAS),[26] and transmission electron microscopy (TEM).[27,28] Their microstructures are therefore well known.

The muon spin relaxation functions were obtained while keeping the samples at fixed temperatures with a helium

TABLE I. The conditions studied by temperature series μSR measurements. Composition (atomic fraction, remainder is Al) and heat treatment after SHT is shown. RT means room temperature; AQ denotes "as quenched."

Composition	Heat treatment		Short name
1.07% Mg, 0.53% Si	≈15 min @	RT	1.6-AQ
	15 days @	RT	1.6-15d
	163 days @	RT	1.6-163d
	1000 min @	70°C	1.6-70C
	1000 min @	100°C	1.6-100C
	1000 min @	200°C	1.6-200C
0.67% Mg, 0.33% Si	≈77 min @	RT	1.0-AQ
	1000 min @	70°C	1.0-70C
0.67% Mg, 0.77% Si	≈15 min @	RT	1.4B-AQ
	163 days @	RT	1.4B-163d
	1000 min @	70°C	1.4B-70C
0.01% trace elements	66 days @	RT	pure

cryostat. The samples were cooled down to 20 K (5 K for pure Al) and heated in steps up to 300 K. At each measurement temperature, 20–60 million positron counts were recorded.

IV. DATA ANALYSIS AND SIMULATIONS

The programs WIMDA[29] and MATLAB were used for μSR data analysis. The measurement error $\epsilon(t)$ in the relaxation functions was estimated by assuming that the number of detected muons in each time bin follow a Poisson distribution. To get an overview of the temperature dependence of the muon behavior, the experimental relaxation functions were fitted to a Gaussian,

$$G(t) = a \exp\left(-\tfrac{1}{2}\sigma^2 t^2\right) + b. \tag{7}$$

The parameter σ gives a good measure of the muon depolarization rate. Not all relaxation functions are well described by a Gaussian, but it gives a consistent fit using only one nonlinear parameter. When a KT fit is attempted, the Δ parameter has a temperature dependence very similar to that of σ.

To better understand the physics behind the experimental relaxation functions, we simulate the diffusion, trapping, spin precession, and decay of muons using a Monte Carlo (MC) algorithm. The algorithm simulates random muons one by one, and unavoidably produces relaxation functions with statistical fluctuations similar to those observed in experiments. Although slower than KT-related integral equation methods, a MC simulation is more flexible, gives better control of the applied approximations, and produces more readily interpretable results.

The preferred muon sites in Al are tetrahedral at temperatures above ≈15 K.[30] Only Al nuclei generate considerable dipole fields, about 40 times stronger than those of Mg and Si.[31] By using Eq. (1) to estimate the magnetic fields, we find that stationary muons in a perfect aluminium lattice give a dipolar width of $\Delta_{\text{dipol}} = 0.495$ μs^{-1}. The experimental data cannot be reproduced by fixing Δ to this value as it makes the muon depolarization too fast. There can be two reasons for this: The simple dipole fields of Eq. (1) are not sufficient to describe the magnetic fields experienced by the muons, or the environments at the muon sites are significantly different from interstitial sites in pure Al. We have therefore resorted to the simpler approach of using a Gaussian magnetic field with an adjustable dipolar width Δ, as in the KT model.

Muon diffusion in Al has been shown to be very fast, even at temperatures below 1 K.[8] We can therefore assume that motional narrowing makes the spin relaxation negligible for muons in a free (nontrapped) state. This makes the muon diffusion rate ν superfluous as a simulation parameter. Trapping and detrapping by defects is described by the parameters ν_t, ν_d, and p_0, all defined below Eq. (6). In certain temperature ranges, several types of defects may act as muon traps simultaneously. The simulations use only a single trap, which is assumed to capture the average trapping behavior in such situations. When including Δ, our parameter set corresponds to the set used in an improved KT model by Hatano *et al.*[21] for Al–0.047% Mg. The results from this model and our MC simulation converge to the same values if the precision used in both models is increased sufficiently. We have generated a database of simulated relaxation functions

by systematic variation of the four parameters. The decrease, recovery, and curvature of a relaxation function depends on all parameters in a complicated manner. Generally, higher values of Δ, ν_t, and p_0 make the depolarization faster, while a higher ν_d makes it slower.

The simulated functions are fitted to the experimental ones with a weighting function $\epsilon(t)^{-2}$. Because of the computational time the simulations require, the number of simulated relaxation functions have been limited to about 7000. The fitting parameters are thus varied with quite coarse steps. To account for this and increase the accuracy of the predicted physical quantities, we estimate the four parameters by weighted averages of all the simulated relaxation functions. The weights are given by E^{-2}, where E is the total error of fitting a simulated function to experimental data.

V. RESULTS

The temperature dependence on the shape of the muon spin relaxation functions is quite similar for all the alloy conditions. As expected, pure aluminium is unique in this respect. Figure 2 shows typical relaxation functions for pure Al and an RT stored alloy condition. Although error bars are not shown, the measurement error increases toward longer times. This is due to poor statistics: Only a few muons survive as long as 25 μs, which is over 10 times the average muon lifetime. What best quantifies the curve shapes is the Gaussian fitting parameter σ, which is plotted for all conditions and measurement temperatures in Fig. 3.

Pure aluminium always has the lowest value of σ. The most pronounced feature of its temperature variation is a peak centered at about 20 K. The alloys also have high values of σ close to this peak, with relaxation functions well described
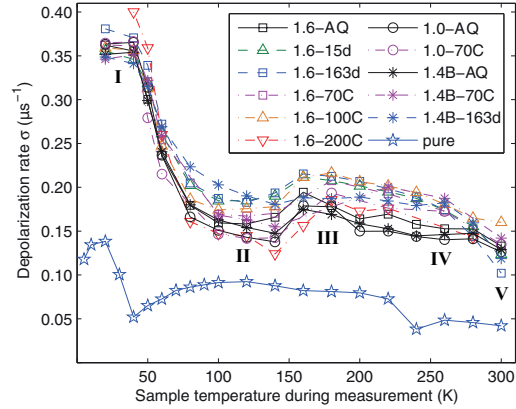
FIG. 3. (Color online) Muon depolarization rate in pure Al (99.99%) and Al-Mg-Si alloy conditions in Table I as a function of temperature. The fit errors are roughly as large as the markers.

by the static KT function [see Eq. (4)]. In the temperature range of this study, σ shows a behavior in Al-Mg-Si alloys remarkably similar to the behaviors in 99.98% pure Nb in the range 11–77 K[10] and Zn-doped GaAs in the range 50–700 K.[5] The peaks are not expected to reflect the same types of defects in these very different materials.

Roman numerals mark the main features of the alloy curves in Fig. 3. The following observations can be drawn about differences between alloy conditions in the different regions:

(1) The 1.0% solute alloy has a lower σ value than the 1.6% solute alloy in all regions except at point **I**.

(2) At point **I**, The σ values are most similar for all conditions. The greatest deviation is the value for 1.6-200C, which is higher than the average.

(3) At point **II**, σ is consistently ordered by heat treatment. From low to high values: as-quenched, 70–100 °C annealed, RT stored. The 200 °C annealed condition is the exception from this pattern. The minimum in σ is shifted to higher temperatures for the Mg-Si-balanced 1.4B conditions.

(4) Peak **III** is seen for all conditions except 1.4B-163d. It is shifted to higher temperatures for the annealed samples.

(5) The curves for the as-quenched conditions are lower than the others from 180 K to 260 K. These, as well as 1.4B-163d, have a high-temperature plateau at point **IV**.

(6) At point **V**, the RT stored conditions reach lower than all other conditions, while the order at point **II** is otherwise kept.

The best-fit relaxation functions simulated by the MC algorithm mostly lie within the measurement error of the experimental ones. To achieve this, a complicated temperature variation in the fitting parameters is required. Figures 4(a)–4(c) show the fitting parameters of 7 selected conditions for all measurement temperatures. We see that the temperature variation of σ in Fig. 3 is an effect of variations in all the parameters Δ, ν_t and ν_d. The least stable parameter is the fraction of initially trapped muons, p_0, which has the least effect on the relaxation function. Its variation is dominated by
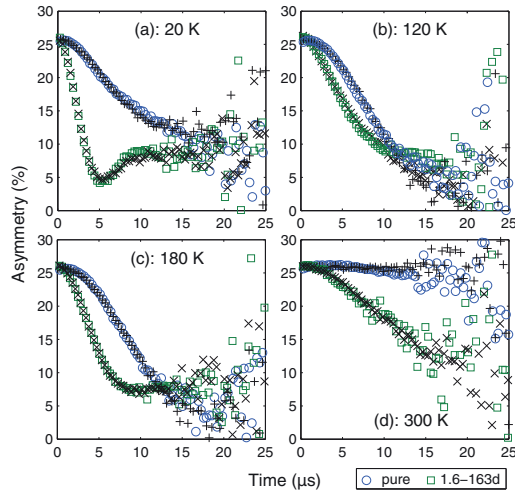

FIG. 2. (Color online) Experimental muon spin relaxation functions calculated from Eq. (3) at 4 selected temperatures for a room temperature stored alloy condition (1.6-163d) and pure Al. The best-fit simulated relaxation functions are shown as black crosses.

fluctuations around average values of $\approx 25\%$ for the alloys and $\approx 20\%$ for pure Al. It is not shown as it gives no additional information to help interpret the relaxation functions. Included in Fig. 4(d) is the estimated fraction of time a muon spends trapped in defects, f_t from Eq. (6).

The 1.6-200C condition is the only one with a high-temperature heat treatment, which allows phases to be precipitated in the matrix. It was investigated by TEM, and was found to contain β'' needles[32] (concentration: 69 000 μm^{-3}, average length: 13 nm), and β' needles[33] (concentration: 400 μm^{-3}, average length: 122 nm), giving a total precipitate volume fraction of 1.2%. The methodology used for this quantification is explained elsewhere.[27]

VI. DISCUSSION

Based on earlier studies, we have some conceptions about types and concentrations of defects in the alloy samples. Right after SHT, only point defects (single solute atoms and vacancies) are present, but we know that the clustering of solute atoms starts within minutes.[12,26] When the material is kept at temperatures between RT and 100 °C, a high concentration ($\sim 10^6$ μm^{-3}) of small clusters form[25,34] at a highly temperature-dependent rate. After 1000 minutes at 200 °C, most clusters are dissolved, and the microstructure consists of the much larger precipitates observed by TEM as well as a dilute solid solution ($\approx 0.4\%$) of Mg and Si atoms. Whether muons diffuse into Al-Mg-Si precipitates and how this affects muon spin relaxation is unknown, but the results from condition 1.6-200C are included for reference. The concentration of vacancies will decrease with storage/annealing time, but the rate of this decrease is unknown.

Most of the muon spin relaxation functions, some of which are shown in Fig. 2, have Gaussian-like shapes. No theory predicts this particular shape explicitly. It arises as a convolution of a constant function (fast diffusion) and a static KT function (trapping by defects). The significant depolarization (above $\sigma \approx 0.05$ μs^{-1}) observed at most temperatures give clear signs of muon trapping in both pure Al and the Al alloys. Simulations help to further clarify the nature of this trapping in the different temperature regimes. They show that increased trapping does not always cause an increase in σ; in fact it can also have the opposite effect. We have made no attempt to explain the temperature variation of Δ on the basis of the local magnetic fields at different trapping sites. The μSR temperature series results are discussed for three separate ranges of measurement temperatures.

A. Low temperature

The pure Al σ peak at 5–40 K has been observed earlier, for Al with 42 and 70 ppm Mn[35] and Al with 117 ppm Ag.[36] Its height was found to increase with the concentration of the trace elements, and its position along the temperature axis is influenced by the type of element. For Mn, the maximum is at 15 K, similar to what we measure in our sample with ≈ 100 ppm trace elements (possibly Fe, Ti, Zn, Cr, Mn, Cu, and Zr). The peak is concurrent with an increased trapping rate, explaining the connection to trace element concentration.

Considering the pure aluminium results, we find it reasonable to assume that muons are trapped by free solute atoms at **I** in the alloy curves of Fig. 3. Figure 4(c) further shows a high trapping rate in the as-quenched alloys at this point. Annealing at 70–100 °C reduces this rate, presumably via solute-solute bond formation. The trapping rate is also reduced by 15 days of RT storage, but increases again after 163 days. NA has been observed to give complicated long-time kinetics.[12] The most likely explanation to increased muon trapping by single solute atoms after long times is the dissolution of energetically unfavorable clusters.[25,34] The 1.6-200C condition has the least amount of atoms in solid solution, but shows signs of even more trapping than in the as-quenched conditions. It is unclear whether this is an effect of its precipitate phases or other defects. For all alloy conditions, the low-temperature trapping sites are characterized by a dipolar width of $\Delta \approx 0.37$ μs^{-1}.

B. Intermediate temperatures

The intermediate temperature σ peak at **III** is higher for conditions with more solute atoms and longer aging at temperatures between RT and 100 °C, suggesting that it is caused by solute clusters/vacancy-solute complexes. From the simulation parameters in Fig. 4, we see both an elevated value of Δ and low detrapping rates in this area. For the Mg-Si-balanced condition 1.4B-163d, the σ peak is near absent. In Fig. 4(c), we see that this coincides with a higher rate of detrapping. From APT studies, we know that this condition contains clusters that are less Mg-rich than the clusters in the 1.6 conditions.[25] A higher detrapping rate means that muons do not bind as tightly to the trapping sites, here assumed to be relatively Mg-poor clusters. This matter is subject to further study.

In light of the heat-treatment-consistent differences in σ and Δ in Figs. 3 and 4(a), we propose that the whole temperature region from **II** to **IV** is a joint trapping region for all possible configurations of Mg-Si-vacancy clusters. If this model is correct, it explains why the as-quenched conditions have an overall high trapping rate, as a high number of solute-vacancy and solute-solute pairs must form quickly to initiate the clustering process. The trapping sites have a dipolar width of $\Delta \approx 0.29$ μs^{-1} around peak **III**.

We have not found an explanation for the trapping peak reaching from 50 K to 240 K in the pure Al curves. Quantitative predictions are difficult for pure Al due to a slow muon depolarization, which makes the fitting parameters very sensitive to small variations in the relaxation functions. Regardless, wee see that the estimated trapping rate reaches the values of the alloy conditions within this range. The value of Δ stays roughly constant through all temperatures for pure Al, which means that the muon environment remains mostly unchanged.

C. High temperature

In an earlier experiment, we measured a decrease in σ with time when storing both pure Al and the 1.6% solute alloy at 300 K after quenching from SHT.[37] In pure Al, the only
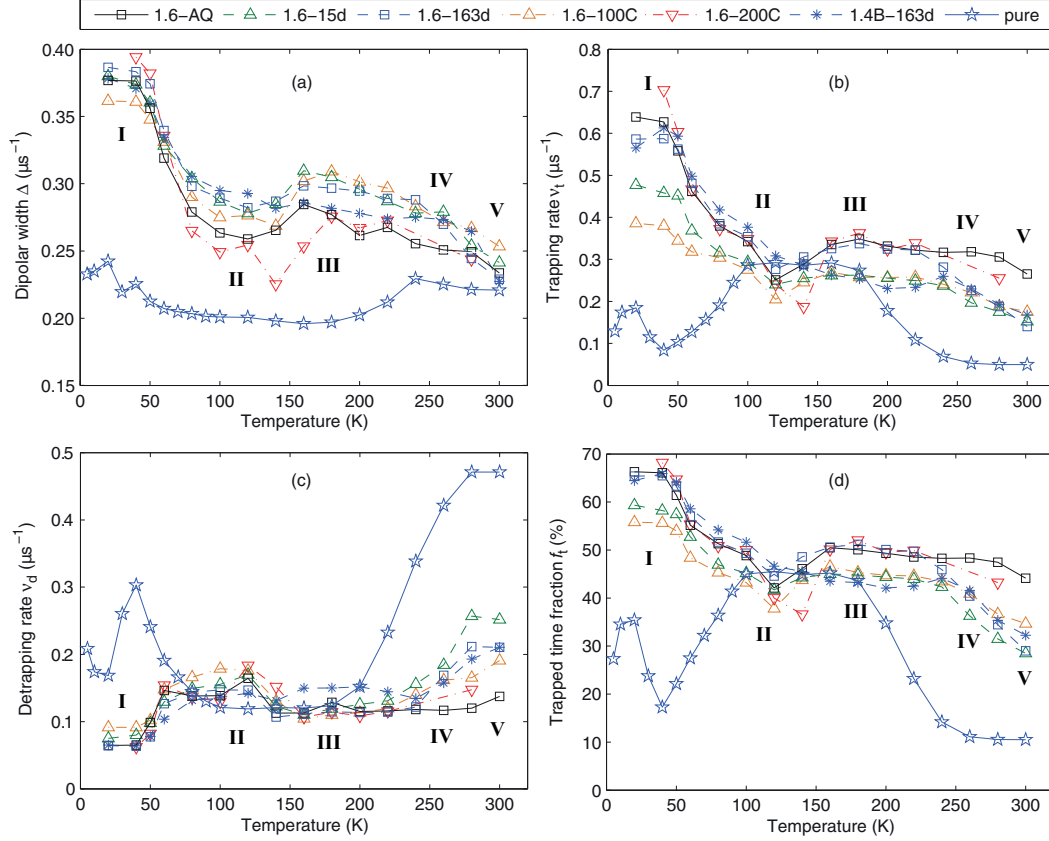
FIG. 4. (Color online) Temperature variation in the physical quantities obtained from fitting simulations to experimental relaxation functions. (a)–(c): Fitting parameters. (d): The fraction of time muons spend trapped, calculated from Eq. (6).

change during this storage is a decreasing concentration of vacancies. This decrease will lead to less muon trapping and a change in the depolarization rate. Vacancies are therefore assumed to trap muons near point **V**. In comparison with other types of defects, the concentration of vacancies is extremely low in all our conditions, and should only affect muons at such high temperatures, where the muon diffusion is fastest.

We suggest from the previous findings that vacancies are the dominant muon trapping defects in Al alloys near point **V**. This explains the high amount of trapping in the as-quenched samples in this region [see Figs. 4(b) and 4(d)], as these samples contain more vacancies than the RT stored and annealed conditions. The high-temperature annealed condition 1.6-200C has a surprisingly high degree of trapping at **V**, although it is expected to have the least amount of vacancies. One suggested explanation is that precipitate phases can contain vacancies trapped during the precipitation process, and that these vacancies can also act as muon traps.

VII. CONCLUSION

We have conducted muon spin relaxation experiments on Al-Mg-Si alloys of three different compositions, with the following heat treatments: as quenched from solution heat treatment, with room temperature storage to give way for solute clustering, and with annealing at 70–100 °C to accelerate this clustering process. In certain ranges of measurement temperatures, we have found systematic deviations in depolarization rates when varying the composition and heat treatment. These deviations can be interpreted as signatures of different defects that provide muon trapping sites. We observe muon trapping by solute atoms at 20–50 K and by vacancies around 300 K. There are also strong indications of influence on the muon depolarization by more extended defects such as Mg-Si(-vacancy) complexes and precipitate phases, which are formed during heat treatment. Results from our simulations suggest that muons are trapped by Mg-Si clusters at intermediate temperatures (100–250 K). A procedure for

quantification of such clusters would be valuable for our understanding of age hardening phenomena and for the ability to enhance alloy properties. Additional temperature series measurements will be conducted to further clarify the effects of solute clustering on muon depolarization in Al-Mg-Si alloys.

*sigurd.wenner@ntnu.no

[1] A. Lappas, K. Prassides, K. Vavekis, D. Arcon, R. Blinc, P. Cevc, A. Amato, R. Feyerherm, F. N. Gygax, and A. Schenck, Science **24**, 1799 (1995).

[2] C. Bernhard, J. L. Tallon, C. Niedermayer, T. Blasius, A. Golnik, E. Brücher, R. K. Kremer, D. R. Noakes, C. E. Stronach, and E. J. Ansaldo, Phys. Rev. B **59**, 14099 (1999).

[3] T. Lancaster, S. J. Blundell, D. Andreica, M. Janoschek, B. Roessli, S. N. Gvasaliya, K. Conder, E. Pomjakushina, M. L. Brooks, P. J. Baker, D. Prabhakaran, W. Hayes, and F. L. Pratt, Phys. Rev. Lett. **98**, 197203 (2007).

[4] K. Nagamine, F. L. Pratt, I. Watanabe, and E. Torikai, RIKEN Rev. **35**, 126 (2001).

[5] K. H. Chow, B. Hitti, R. F. Kiefl, R. L. Lichti, and T. L. Estle, Phys. Rev. Lett. **87**, 216403 (2001).

[6] R. L. Lichti, K. H. Chow, and S. F. J. Cox, Phys. Rev. Lett. **101**, 136403 (2008).

[7] W. Gauster, A. Flory, K. Lynn, W. Kossler, D. Parkin, C. Stronach, and W. Lankford, J. Nucl. Mater. **69–70**, 147 (1978).

[8] K. W. Kehr, D. Richter, J. M. Welter, O. Hartmann, E. Karlsson, L. O. Norlin, T. O. Niinikoski, and A. Yaouanc, Phys. Rev. B **26**, 567 (1982).

[9] E. Sato, T. Hatano, Y. Suzuki, M. Imafuku, M. Sunaga, M. Doyama, Y. Morozumi, T. Suzuki, and K. Nagamine, Hyperfine Interact. **17**, 203 (1984).

[10] C. Boekema, R. H. Heffner, R. L. Hutson, M. Leon, M. E. Schillaci, W. J. Kossler, M. Numan, and S. A. Dodds, Phys. Rev. B **26**, 2341 (1982).

[11] C. Marioara, S. Andersen, J. Jansen, and H. Zandbergen, Acta Mater. **51**, 789 (2003).

[12] S. Wenner, C. D. Marioara, S. J. Andersen, and R. Holmestad, Int. J. Mater. Res. **103**, 948 (2012).

[13] K. Yamada, T. Sato, and A. Kamio, Mater. Sci. Forum **331–337**, 669 (2000).

[14] I. Kovács, J. Lendvai, and E. Nagy, Acta Metall. **20**, 975 (1972).

[15] F. De Geuser, W. Lefebvre, and D. Blavette, Phil. Mag. Lett. **86**, 227 (2006).

[16] C. D. Marioara, S. J. Andersen, T. N. Stene, H. Hasting, J. Walmsley, A. T. J. Van Helvoort, and R. Holmestad, Phil. Mag. **87**, 3385 (2007).

[17] A. Yaouanc and P. D. De Réotier, *Muon Spin Rotation, Relaxation, and Resonance: Applications to Condensed Matter*, International Series of Monographs on Physics (Oxford University Press, 2011).

[18] R. S. Hayano, Y. J. Uemura, J. Imazato, N. Nishida, T. Yamazaki, and R. Kubo, Phys. Rev. B **20**, 850 (1979).

[19] R. Kubo and T. Toyabe, in *Magnetic Resonance and Relaxation*, edited by R. Blinc (North-Holland, Amsterdam, 1967), p. 810.

[20] E. Holzschuh and P. F. Meier, Phys. Rev. B **29**, 1129 (1984).

[21] T. Hatano, Y. Suzuki, M. Doyama, Y. J. Uemura, T. Yamazaki, and J. H. Brewer, Hyperfine Interact. **17**, 211 (1984).

[22] T. R. Waite, Phys. Rev. **107**, 463 (1957).

[23] I. Z. Machi, S. H. Connell, M. Dalton, M. J. Sithole, K. Bharuth-Ram, S. F. J. Cox, and C. Baines, Diam. Relat. Mater. **13**, 909 (2004).

[24] T. Matsuzaki, K. Ishida, K. Nagamine, I. Watanabe, G. H. Eaton, and W. G. Williams, Nucl. Instrum. Methods A **465**, 365 (2001).

[25] M. Torsæter, H. S. Hasting, W. Lefebvre, C. D. Marioara, J. C. Walmsley, S. J. Andersen, and R. Holmestad, J. Appl. Phys. **108**, 073527 (2010).

[26] J. Banhart, M. D. H. Lay, C. S. T. Chang, and A. J. Hill, Phys. Rev. B **83**, 014101 (2011).

[27] C. Marioara, S. Andersen, H. Zandbergen, and R. Holmestad, Metall. Mater. Trans. A **36**, 691 (2005).

[28] C. Marioara, H. Nordmark, S. Andersen, and R. Holmestad, J. Mater. Sci. **41**, 471 (2006).

[29] F. L. Pratt, Physica B: Condensed Matter **289–290**, 710 (2000).

[30] O. Hartmann, E. Karlsson, L. O. Norlin, T. O. Niinikoski, K. W. Kehr, D. Richter, J. M. Welter, A. Yaouanc, and J. Le Hericy, Phys. Rev. Lett. **44**, 337 (1980).

[31] WebElements: The Periodic Table on the Web, http://www.webelements.com.

[32] H. W. Zandbergen, S. J. Andersen, and J. Jansen, Science **277**, 1221 (1997).

[33] R. Vissers, M. van Huis, J. Jansen, H. Zandbergen, C. Marioara, and S. Andersen, Acta Mater. **55**, 3815 (2007).

[34] M. Torsæter, Ph.D. thesis, Norwegian University of Science and Technology, 2011.

[35] T. Niinikoski, O. Hartmann, E. Karlsson, L. Norlin, K. Kehr, D. Richter, J. Welter, J. Chappert, and A. Yaouanc, Physica B+C **108**, 879 (1981).

[36] O. Hartmann, E. Karlsson, B. Lindgren, E. Wäckelgård, D. Richter, R. Hempelmann, and J. M. Welter, Hyperfine Interact. **17**, 197 (1984).

[37] S. Wenner, K. Matsuda, K. Nishimura, J. Banhart, T. Matsuzaki, D. Tomono, F. L. Pratt, M. Liu, Y. Yan, C. D. Marioara, and R. Holmestad, in *13th International Conference on Aluminum Alloys*, edited by W. Heiland, A. D. Rollett, and W. Cassada (Wiley, 2012), pp. 37–42.

Paper 2

Muon kinetics in heat treated Al(–Mg)(–Si) alloys

S. Wenner, K. Nishimura, K. Matsuda, T. Matsuzaki, D. Tomono,
F. L. Pratt, C. D. Marioara and R. Holmestad

Muon kinetics in heat treated Al (–Mg)(–Si) alloys

Sigurd Wenner [a],*, Katsuhiko Nishimura [b], Kenji Matsuda [b], Teiichiro Matsuzaki [c], Dai Tomono [c], Francis L. Pratt [d], Calin D. Marioara [e], Randi Holmestad [a]

[a] *Department of Physics, NTNU, Høgskoleringen 5, NO-7491 Trondheim, Norway*
[b] *Department of Materials Science and Engineering, University of Toyama, Gofuku 3190, Toyama-shi, Toyama 930-8555, Japan*
[c] *Advanced Meson Science Laboratory, RIKEN Nishina Center for Accelerator Based Science, RIKEN, Wako, Saitama 351-0198, Japan*
[d] *ISIS Facility, Rutherford Appleton Laboratory, Chilton OX11 0QX, UK*
[e] *Materials and Chemistry, SINTEF, Box 4760 Sluppen, NO-7465 Trondheim, Norway*

Abstract

Al–Mg–Si alloys are heat-treatable and rely on precipitation hardening for their mechanical strength. We have employed the technique of muon spin relaxation to further our understanding of the complex precipitation sequence in this system. The muon trapping kinetics in a material reveals a presence of atom-sized defects, such as solute atoms (Mg and Si) and vacancies. By comparing the muon kinetics in pure Al, Al–Mg, Al–Si and Al–Mg–Si when held at different temperatures, we establish an interpretation of muon trapping peaks based on different types of defects. Al–Mg–Si samples have a unique muon trapping peak at temperatures around 200 K. This peak is highest for samples that have been annealed at 70–150 °C, which have microstructures dominated by a high density of clusters/Guinier–Preston zones. The muon trapping is explained by the presence in vacancies inside these structures. The vacancies disappear from the material when the clusters transform into more developed precipitates during aging.

1. Introduction

Muon spin methods are mainly used to probe magnetic properties of materials, but can also be used to study other phenomena as a consequence of their magnetic properties. A common example is solid-state diffusion in non-magnetic materials [1]. The techniques are similar to positron annihilation spectroscopy (PAS) in that unstable elementary particles are implanted in a material and decay, and their decay products are detected outside of the material. The spin precession of muons can be indirectly observed through the positrons they decay into. In a muon spin relaxation (μSR) experiment, muons enter the sample with their spin aligned antiparallel to their direction of motion. With no external field applied, the precession is caused by

magnetic fields set up by the atomic nuclei inside the material. In a non-magnetic metal like aluminium, these fields are randomly oriented, and polarized muons become depolarized ("relaxed") in a matter of microseconds.

Al–Mg–Si alloys constitute most of the worldwide aluminium market as they have good mechanical strength and are easily formable into end products [2]. An optimal heat treatment of alloys containing merely 1% solutes (Mg and Si) typically increases the hardness by a factor of 5 from pure aluminium. After the material is formed, an industrial hardening procedure consists of solution heat treatment (SHT), typically at 550 °C, some (unavoidable) storage at room temperature (RT) and artificial aging (AA), typically at 180 °C. The hardening during heat treatment is caused by precipitation of metastable phases through diffusional phase transitions. Going from low to high aging times/temperatures, the generic precipitation sequence for Al alloys is

* Corresponding author.
  E-mail address: sigurd.wenner@ntnu.no (S. Wenner).

SSSS → Solute clusters

    → Semi-coherent (hardening) precipitates

    → Incoherent (non-hardening) precipitates,   (1)

where SSSS is an acronym for supersaturated solid solution. In general, the precipitate phases grow larger and become fewer as we proceed through the sequence.

Al–Mg–Si alloys quenched from SHT are unstable at RT, and atomic clusters (with Mg and Si at Al-face-centred cubic (fcc) positions) form from the SSSS. The clusters in general are too small and coherent with the Al matrix to be observed by transmission electron microscopy (TEM). However, new experimental possibilities have sparked an interest in solute clustering the last decades, with techniques such as PAS [3,4], atom probe tomography (APT) [5–7] and differential scanning calorimetry (DSC) [8,9]. Several independentAPT studies [5,10] have shown that two kinds of solute clusters can form in Al–Mg–Si alloys. Cluster (1) (the "bad" cluster) forms during RT storage (of alloys with Mg + Si > 1% [10,11]), has a non-fixed composition and does not grow or develop during further heat treatment. Cluster (2) (the "good" cluster) forms during annealing at 70–150 °C directly after SHT [6] (and during RT storage of alloys with Mg + Si < 1% [10,11]), has an Mg/Si ratio close to 1 and can develop into hardening β'' precipitates.

The hardening Al–Mg–Si precipitates are all needle shaped, with their main growth/coherency direction along $\langle 0\,0\,1 \rangle_{Al}$. The most important of these is β'' [12,13]. At temperatures above 200 °C, Al–Mg–Si alloys over-age, transforming β'' to less coherent precipitates, which causes a drop in hardness. The thermal and mechanical treatments applied to alloys determine their progression through the precipitation sequence. Understanding the early steps, in particular the formation of Mg–Si (–vacancy) clusters, is essential, as the composition, concentration and size of these clusters influence the precipitate microstructure in finished products.

Muons undergo interstitial diffusion inside solids. In aluminium, they have been shown to be trapped by atoms in substitutional lattice positions and by vacancies [14,15], yielding a lower apparent muon diffusivity. In this work, we exploit this effect and identify the muon trapping behaviour of Mg and Si atoms as well as vacancies in different stages of heat treatment of aluminium alloys. Due to its industrial and scientific interest, we hereby study the ternary Al–Mg–Si system, and we include the binary Al–Mg and Al–Si alloys mainly to help isolate the ternary-specific features in the μSR data. The processes occurring in the binary subsystems are definitely still worth investigating in their own rights, seeing that they are used as alloys for many applications where high strength is not required [2]. No precipitation has been observed in annealed Al–Mg alloys, while diamond Si particles precipitate in the Al–Si system without increasing the hardness significantly [16]. These particles also form in over-aged Si-rich Al–Mg–Si

alloys [13]. Very dilute alloys have been probed with μSR before, and small additions of Si, Mg and Cu were found to greatly affect the muon kinetics [17]. Our previous work on the Al–Mg–Si system revealed the presence of a muon trapping peak corresponding to clustering/precipitation [18]. By analysing more conditions and including binary alloys, we aim to improve our understanding of the interactions between muons and precipitates in Al–Mg–Si alloys. The main goal of the current work is to establish a connection between muon trapping rates and the microstructure of materials as found from TEM and APT studies.

We will explore the theory of muons and their interactions with samples in greater detail in the next section. Sections 3 and 4 explain the procedures of the experiments and the analysis of μSR data. Results from various experiments on Al (–Mg)(–Si) alloys are presented in Section 5. Some mechanisms of muon trapping are proposed in the discussion part (Section 6), and are used to infer the behaviour of vacancies during heat treatment of Al alloys, leading up to the conclusions in Section 7.

2. Theory

Like electrons, muons are elementary particles in the lepton family. As in most muon spin research [19], we use positively charged muons, since the negatively charged variant has a material-dependent lifetime. The lifetime of a positive muon always has an average value of 2.197 μs. The muon decays into a positron and two neutrinos:

$$\mu^+ \rightarrow e^+ + \nu_e + \bar{\nu}_\mu \tag{2}$$

The direction of motion for the positron is asymmetric with respect to the muon spin, a fact which μSR measurements depend on [20]. The exact distribution for the emission angle with respect to the muon spin, θ, is

$$p(\theta) = 1 + A\cos\theta \tag{3}$$

where A is an asymmetry parameter dependent on the experimental set-up. Positrons are detected in the backward and forward directions with respect to the initial muon spin. From the positron counts N_b (backward) and N_f (forward), the muon spin asymmetry $G(t)$ is calculated:

Table 1
Compositions (columns) and heat treatments (rows) of the 16 samples used in the current μSR measurements. Conditions with ∗ were analysed in a previous publication [18] and are included here for comparisons in a broader context.

Composition (at.%), balance is Al	1.6% Mg$_2$Si	0.5% Mg	0.5% Si	0.01% Impurities
1. AQ	Yes∗ (2)	Yes	Yes	
2a. RT for ≈2 weeks	Yes∗	Yes	Yes	
2b. RT for >2 months	Yes∗			Yes∗
3a. 70/100/150 °C for 1000 min	Yes∗/ Yes∗/Yes			
3b. 200 °C for 1000 min	Yes∗	Yes	Yes	
3c. RT for 7d + 100 °C for 1000 min	Yes			

S. Wenner et al. / Acta Materialia 61 (2013) 6082–6092

$$G(t) = \frac{N_f - \alpha N_b}{N_f + \alpha N_b} \qquad (4)$$

where t is the time after muon implantation and the parameter α compensates for differences in distance between the sample and the two detectors. The asymmetry is often expressed through a normalized relaxation function $g(t) = G(t)/A$, with the property $g(0) = 1$.

Larmor precession of the muon spin in the local magnetic fields **B** can be calculated using matrix multiplication and trigonometric functions of ωt, where $\omega = \gamma_\mu \|\mathbf{B}\|$, with γ_μ being the gyromagnetic ratio of the muon. A muon in a static magnetic field has a trivial spin relaxation [21]. For an ensemble of interstitially diffusing muons, the magnetic field changes upon muon site transitions. An abrupt transition between uncorrelated fields is a good approximation, and is applied in the strong-collision model [21]. Even when this simplified model is used, the general problem of spin relaxation for muons with site-dependent diffusion rates is not analytically solvable. However, the relaxation function can be found by integral [22] or differential equations [23] for some specific cases.

An important feature of any model applied to Al alloys is the inclusion of muon trapping by defects. The concentration of a defect type and its binding energy with muons manifests itself in the measured relaxation function. The spin relaxation behaviour in aluminium has a much more complicated temperature variation than that of e.g. copper [24]. This is due to very fast muon diffusion and trapping by vacancies and trace elements, which are heavily temperature-dependent processes [25]. Our method for calculating relaxation functions is described in Section 4.

3. Experimental

Samples of pure Al (99.99%) and Al–Mg, Al–Si and Al–Mg–Si alloys were used in the μSR experiments. The material was cast and rolled to 1 mm sheets at the University of Toyama. The sample dimensions were 25 mm × 25 mm × 1 mm. All samples underwent a SHT of 1 h at 575 °C and subsequent quenching in ice water, before one of three heat treatment procedures was performed:

1. μSR measurement directly (approx. 15 min) after quenching, which we call as-quenched (AQ) conditions.
2. Some time, typically days/months of storage at RT before μSR measurements.
3. Annealing for 1000 min ($\approx$16 h) at some specified temperature before μSR measurements.

In the results section, samples are denoted based on their atomic (molar) fraction of solute, e.g. Al–0.5% Mg. The Al–Mg–Si alloy we used has 1.6% solute and twice as much Mg as Si, and is thus referred to through its semi-binary composition, Al–1.6% Mg$_2$Si. The annealing temperatures are always given in °C, while the sample temperatures during measurements are always in K. Table 1 displays all the conditions used in this work.

The μSR experiments were conducted at the RIKEN-RAL Muon Facility in Oxfordshire, UK [26]. We used the ARGUS muon spectrometer, which is equipped with a total of 192 positron detectors in annular forward and backward arrays, covering a 25% solid angle. A helium cryostat was used to control the temperature of the samples during the measurements. To capture the muon diffusion kinetics in a broad temperature region, we measured muon spin relaxation functions while heating stepwise from 20 to 300 K. Between 20 and 60 million positron detections (events) were recorded at 12–20 temperature points for all conditions.

Four of the samples, annealed at 150 °C and above, were prepared (as in e.g. [27]) for TEM investigations of the precipitate microstructure. Bright-field images recorded on film with a Philips LaB$_6$ CM30 transmission electron microscope were used for this analysis. The microscope was operated using an acceleration voltage of 150 kV.

4. Data analysis and simulations

Apart from direct visual comparison, our method of choice for interpreting relaxation functions is to compare them to a Monte Carlo simulation. An indeterministic simulation is appropriate, since diffusion, trapping/detrapping by defects, the magnetic field at muon sites and muon decay are all stochastic processes/variables. The magnetic field vectors are Gaussian distributed, with a standard deviation Δ/γ_μ, where Δ is the dipolar width, proportional to the strength of the magnetic field. An ensemble of 60 million muons are simulated, varying four parameters: the dipolar width Δ, the trapping/detrapping rates v_t and v_d, and the fraction of initially trapped muons p_0. In defect-free locations, the diffusion rate of muons is practically infinite in comparison to their depolarization rate [14,22], so our model neglects spin relaxation unless the muon is trapped. Temperature is not included explicitly in the simulations, but manifests itself in the thermodynamics, which is controlled through the fitting parameters v_t and v_d. The decay of a muon is calculated with Eq. (3). Forward/backward positrons are counted, and put into one of 2000 bins based on their lifetime, as in the experiments.

Simulated relaxation functions are fitted to the experimental ones by running through a database of fitting parameters and associated functions. Each experimental time bin has a calculated error $\epsilon(t)$ in spin relaxation (calculated by assuming the detected muons to follow a Poisson distribution). These errors are used as fitting weights, $w(t) = \epsilon(t)^{-2}$. Fitting parameters are estimated as an average over all the simulated relaxation functions, using the total fitting error as weight: $W_i = E_i^{-2}$ for simulated function i. This reduces the scatter in the results from simply using the parameters of a single best-fit simulated function. Similarly, the errors in the fitting parameters are estimated

from a weighted standard deviation. For tests of the fitting procedure, see Section 5.1.

It is desirable to predict the trapping sites for muons based on their binding energies to simple point defects. Due to restrictions in the software used for energy calculations, we use a hydrogen ion (a proton) as a crude model for a positive muon in Al. The hydrogen ion H^+ has the same charge as μ^+, and a nine times greater mass. Both tend to localize at interstitial sites in Al. In particular, muons prefer sites with tetrahedral symmetry at temperatures above ≈ 15 K [24]. Muons do not form muonium (a bound muon–electron system) in metals, and hydrogen stays ionic by analogy. For simplicity, we nonetheless refer to it by H below. To find the binding energy between H and solute atoms/vacancies, we employ the Vienna Ab Initio Simulations Package [28,29], which performs quantum mechanical energy calculations using density functional theory (DFT) [30,31]. The supercell of the model system consists of 216 Al atoms on an fcc lattice, where one atom is replaced by Mg, Si or a vacancy, and a H atom is introduced at a neighbouring interstitial site. The binding energy between H and a substitutional defect X is calculated as follows:

$$E(H - X) = E(215Al + H + X) - E(216Al + H)$$
$$- E(215Al + X) + E(216Al) \qquad (5)$$

For more computational details, we refer to the similar calculations in Ref. [11].

5. Results

5.1. Reproducibility of measurements

As a check of the consistency of our μSR measurements and of the fitting to simulated data, we have run two equal experiments on the Al–1.6% Mg$_2$Si alloy in an AQ condition. After quenching, the samples were prepared for the measurements, which required keeping them at RT for ≈ 15 min before cooling down to 20 K. The number of events measured and the number of temperature points were lower in the second run, leading to shorter storage at e.g. 300 K inside the spectrometer. As longer time at higher temperatures promotes atomic clustering, this creates minor differences in microstructure between the two conditions, but these are most likely smaller than the combined errors of experiment and fitting. Therefore, the differences in spin relaxation is bound to indicate the reproducibility/accuracy of zero-field μSR measurements as applied to Al alloys. Overlay plots of the relaxation functions for all measurement temperatures are presented in Fig. 1. The initial asymmetry (at time $t = 0$) is slightly different due to unavoidable differences in the experimental set-up. This effect is taken into account in the analysis. Otherwise, it is difficult to observe any differences in the relaxation functions by eye.

Fig. 2 shows the fitting parameters we obtain when comparing the data in Fig. 1 to simulated relaxation functions. The greatest deviations are in the fraction of initially trapped muons and the trapping rates, suggesting that these parameters cause the least variation in the relaxation functions when altered. The trapping rate is difficult to estimate at low temperatures because the relatively slow kinetics do not bring the system near an equilibrium before the muons decay. Regardless of this, we mainly use the trapping rate v_t to compare conditions in the further, as it is readily interpretable in terms of defect content. Figs. 1 and 2 shows that the reproducibility of the experiments is reasonable and that the error in v_t is estimated well.

In connection to this uncertainty analysis, we note that the 100 °C annealed and 15 days RT stored Al–1.6% Mg$_2$Si samples had incorrect fitting parameters (e.g. too low v_t) in a previous publication [18]. The cause of the errors was related to the experimental set-up, and has been corrected for in this paper.

5.2. Binary alloys and their relationship to Al and Al–Mg–Si

Six experiments with binary alloys were conducted, with Al–0.5% Mg and Al–0.5% Si in AQ, RT stored and annealed conditions. The trapping rates are shown separately for the two systems in Fig. 3. It becomes immediately obvious that Mg and Si atoms affect muons very differently. We note the following trapping rate characteristics for Al–Mg:

- Heat treatment does not change the muon behaviour much in Al–Mg alloys.
- There is a remarkable coincidence of Al–Mg and Al–Mg–Si at temperatures up to 120 K, despite a big difference in Mg content.
- RT stored and AQ samples have higher trapping rates than pure Al at temperatures of 240–300 K. This is not the case for the sample annealed at 200 °C.
- All Al–Mg conditions have a trapping peak at 160 K, for which we can currently provide no explanation.

Correspondingly, for Al–Si:

- The muon behaviour in annealed and RT stored samples is very similar to that in pure Al, excluding only the lowest temperatures.
- Only when measuring directly after quenching from SHT did we observe a significant difference at high temperatures. The extended peak from 100 to 250 K is similar to peaks previously observed in Al–Mg–Si for all kinds of heat treatments (see Ref. [18] and Figs. 5 and 6).

TEM images of the annealed conditions were obtained, and are presented in Fig. 4. Some dislocations are observed in both samples, with a slightly higher concentration in Al–Si. Diamond Si particles are also present in Al–Si. They
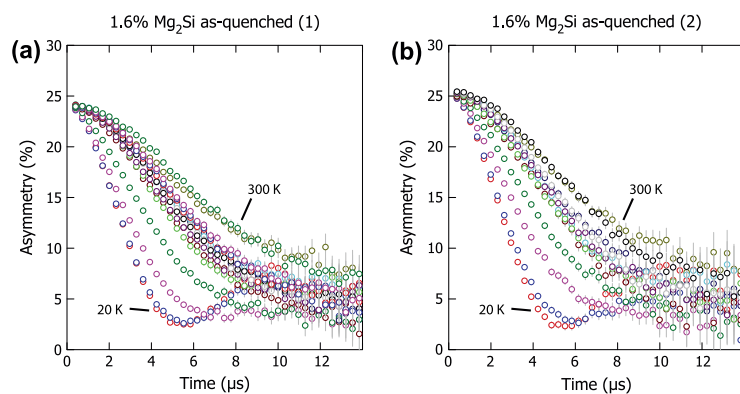
Fig. 1. Overlays of relaxation functions measured at temperatures from 20 to 300 K. Both samples come straight from quenching after SHT, and are compared to check the reproducibility of the μSR experiments. The sets of colours do not correspond to the same temperatures in both cases.
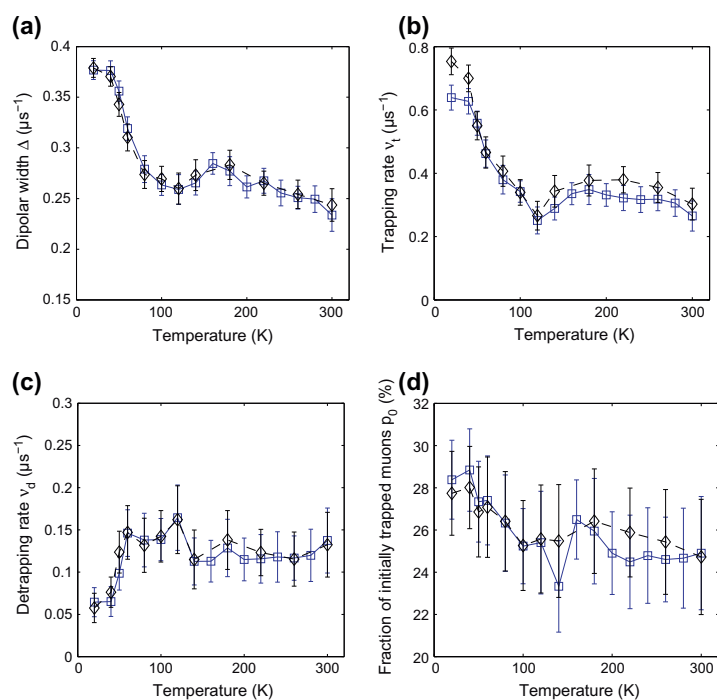

Fig. 2. Fitting parameters for the alloy with 1.6% Mg₂Si, directly after quenching from SHT. Two identical experiments. The first experiment (Fig. 1(a)) is indicated by squares connected by a solid blue line. (For interpretation of the references to colour in this figure legend, the reader is referred to the web version of this article.)

mainly have a plate morphology, with a typical size of 70 nm × 70 nm × 7 nm, seen both edge-on and as moiré patterns in Fig. 4(b). No particles are observed in Al–Mg.

5.3. Al–Mg–Si alloys with RT storage before annealing

Motivated by results from APT [6], we conducted μSR experiments on the ternary Al–1.6% Mg₂Si alloy annealed
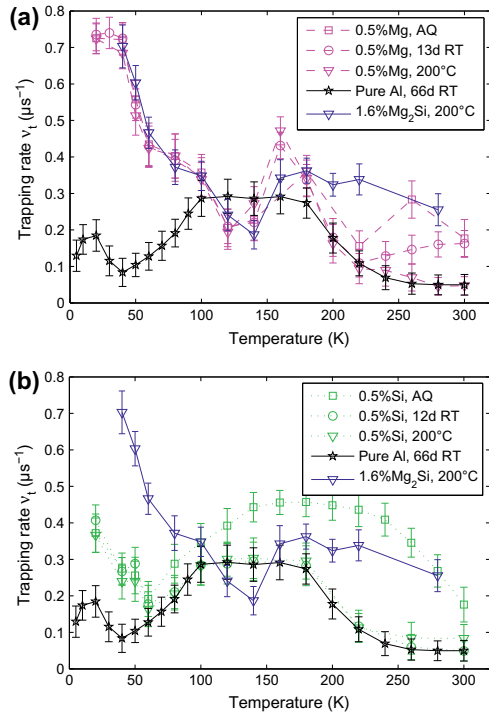
Fig. 3. Calculated trapping rates in binary alloys. (a) Al–Mg and (b) Al–Si, compared to pure Al and the Al–Mg–Si alloy. The samples are AQ, RT stored for approx. 2 weeks or annealed for 1000 min at 200 °C after SHT.

for 1000 min at 100 °C with and without RT storage between SHT and this annealing. Fig. 5 shows the calculated trapping rates of the two conditions, as well as a condition with 15 days of RT storage (and no annealing) for comparison. We see that the annealed samples follow each other until a temperature of 120 K is reached, after which the trapping is consistently lower in the sample with RT storage. The sample with only RT storage lies even lower in this region.

In addition to having a diminished high-temperature trapping peak, the exclusively RT stored sample also lies below the annealed samples at low measurement temperatures. This is observed for all AQ and RT stored samples, and is discussed in Section 6.1.

5.4. Influence of annealing temperature on trapping rates in Al–Mg–Si alloys

Adding to the conditions previously investigated [18], we have data from a set of Al–1.6% Mg₂Si alloys annealed for 1000 min at four different temperatures. Higher temperatures will bring the microstructure in the material further along the precipitation sequence in Eq. (1). The results of this study are shown as muon trapping rates in Fig. 6. Annealing

at 70, 100 and 150 °C gives a very similar muon behaviour, with the characteristic peak above 120 K higher than in the AQ and RT stored conditions, which are also shown in the figure. Annealing at 200 °C reduces the trapping rate to the AQ level. Since RT storage is equivalent to annealing the sample at ≈20 °C for a very long time, we see the biggest changes in the transitions 20 °C → 70 °C and 150 °C → 200 °C.

TEM images of the microstructure in the alloys annealed at 150 and 200 °C are shown in Fig. 7. The 150 °C annealed sample has a fine microstructure of β″ precipitates and their precursors (pre-β″ Guinier–Preston (GP) zones; see Ref. [32]). Annealing at 200 °C is seen to produce a coarser microstructure. As the alloy begins to over-age, the precipitate types change from β″ to larger β′ and other less coherent phases (see Ref. [27] for more detailed TEM studies of a similar alloy annealed at 200 °C). In some cases, clusters formed during annealing at 70–100 °C are also observable by TEM (see e.g. Ref. [33]). We have not attempted such analysis in this work, and refer instead to APT results on similar conditions when discussing low-temperature annealing in Section 6.

5.5. Calculations of muon binding energy

Binding energies between hydrogen and substitutional defects in Al–Mg–Si alloys were calculated as explained in Section 4, and are displayed in Table 2. H at an octahedral site in pure Al and H as a substitutional defect are included for completeness. The hydrogen ion H⁺ has a larger mass than a muon μ⁺, and thus different binding energies, but the numbers should follow a similar trend for muons. We see that substitutional and octahedral sites are very unfavourable for a hydrogen atom. The main result is that the binding energy of hydrogen/muons to substitutional defects is sorted as Si < Mg < vacancy.

Measuring binding energies using μSR is a challenge because of the complexity of the physics involved. Most regions of a typical Arrhenius plot do not look linear, meaning that simple Boltzmann kinetics is insufficient to describe the real situation. High-temperature tails create reasonably linear Arrhenius plots, as shown in Fig. 8, with a linear fit in the temperature range 200–300 K. The two selected conditions are Al–Mg and Al–Mg–Si alloys, only the last of which should have any solute clustering dynamics. The linear fit gives activation energies of 0.0199 eV (Al–0.5% Mg, 1000 min at 200 °C) and 0.0633 eV (Al–1.6% Mg₂Si, 163 days at RT). This can be interpreted as binding energies for a high-temperature muon trap, with seemingly very different natures in the two cases. The activation energy for the low-temperature peak (20–80 K) of the same Al–1.6% Mg₂Si condition was measured to 0.0069 eV. The low-temperature trap is thus considerably easier to escape from.
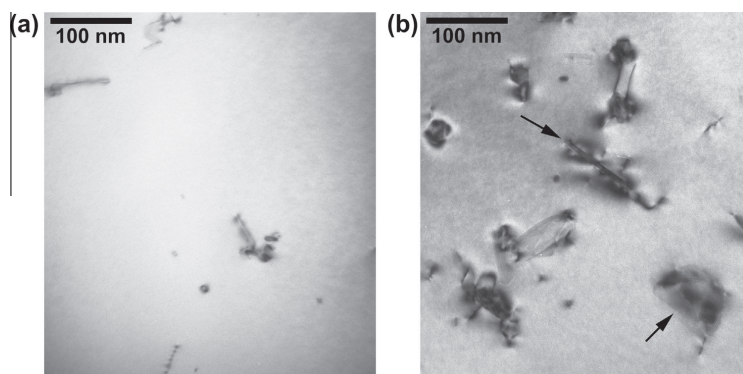
Fig. 4. TEM images of binary alloys annealed at 200 °C for 1000 min after SHT. (a) Al–0.5% Mg and (b) Al–0.5% Si. Both are viewed in the $[0\,0\,1]_{Al}$ direction. Two of several diamond Si particles are indicated by arrows in (b).
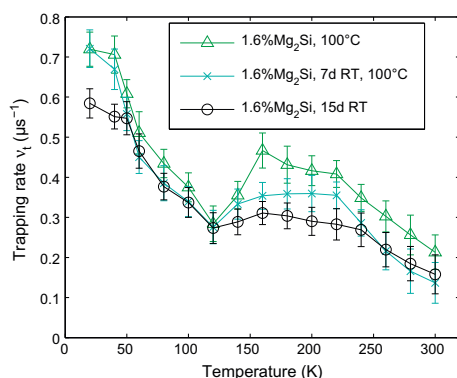

Fig. 5. Trapping rates of an annealed Al–1.6% Mg$_2$Si alloy, with and without 1 week of RT storage between SHT and the annealing. A sample with only 2 weeks of RT storage after SHT is included for comparison.
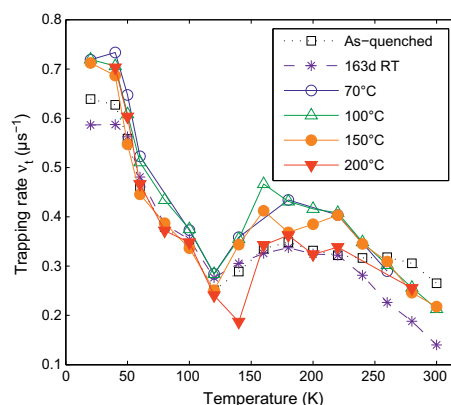

Fig. 6. Muon trapping rates in Al–1.6% Mg$_2$Si, annealed for 1000 min at different temperatures. Samples which are RT stored and AQ from SHT are included for comparison. See Fig. 5 for approximate error bars.

6. Discussion

6.1. Muon trapping in Al (−Mg)(−Si)

We focus here on the bonds formed between muons and various lattice defects in aluminium, which has been shown to greatly influence the measured muon spin relaxation functions.

At low temperatures, Al–Mg has a much higher trapping peak than Al–Si (Fig. 3), leading to a clear conclusion: Mg–μ^+ bonds are stronger than Si–μ^+ bonds. This is supported by the DFT results for hydrogen–solute bonds in Table 2, and can be qualitatively explained in terms of the lower number of valence electrons in Mg relative to both Al and Si [17]. The height of the low-temperature trapping peak is the same for Al–0.5% Mg and Al–1.6% Mg$_2$Si (roughly twice the amount of Mg atoms). It seems that the Mg–μ^+ trapping kinetics reach a point of satura-

tion at low concentrations of Mg. As-quenched Al–Si has a large trapping peak above 60 K, which disappears with any heat treatment, including storage at RT. Al–Mg has a radically different behaviour, losing its high-temperature muon trapping only after annealing. A simple explanation is that Al–Mg needs annealing to get rid of its vacancies, while they disappear from Al–Si during RT storage. Vacancies have certainly been found to diffuse slowly near Mg atoms [34]. The trapping site in AQ Al–Si can be small clusters of Si and vacancies, judging by the favourability of such bonds [35,36]. If this interpretation is correct, the vacancies leave the clusters and disappear from the material during weeks at RT. Large, incoherent diamond Si particles apparently have no effect on the muon behaviour, judging from the lack of differences in muon trapping rate between RT stored and annealed samples in Fig. 3(b).
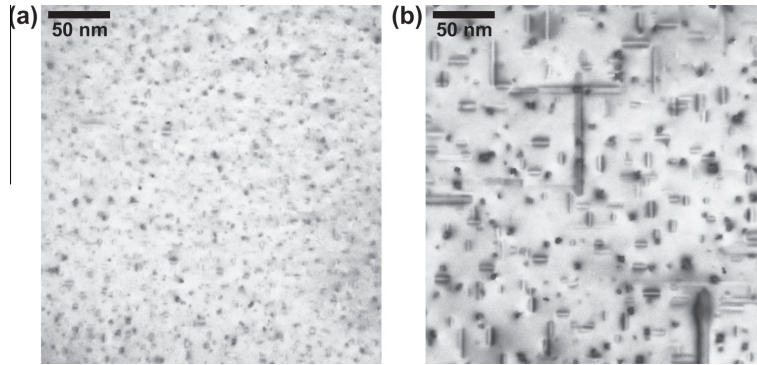
Fig. 7. TEM images of Al–1.6% Mg$_2$Si annealed for 1000 min at temperatures (a) 150 °C and (b) 200 °C after SHT. Both are viewed in the [0 0 1]$_{Al}$ direction, and the precipitates are aligned along $\langle 0 0 1 \rangle_{Al}$ directions.

Table 2
Binding energies between hydrogen and point defects in Al–Mg–Si alloys as calculated by DFT and Eq. (5). Tetr. and Oct. mean tetrahedral and octahedral interstitial sites, respectively. The energy of hydrogen at a tetrahedral site in pure Al is always used as a reference.

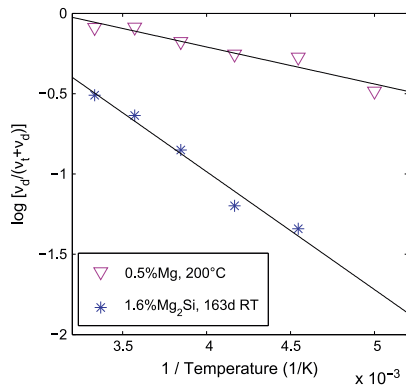| Hydrogen site	Energy (eV)
Tetr. next to Mg	−0.1298
Tetr. next to Si	−0.0318
Tetr. next to vacancy	−0.3109
Subst. (inside vacancy)	0.4965
Oct. in pure Al	0.2560

Fig. 8. Arrhenius plot showing the logarithm of the equilibrium fraction of free (detrapped) muons. The selected conditions are Al–0.5% Mg annealed at 200 °C for 1000 min and Al–1.6% Mg$_2$Si stored at room temperature for 163 days. Measurement temperatures are in the range 200–300 K.

Fig. 5 shows that there is less muon trapping at the previously identified "cluster trapping peak" [18] in annealed samples if they have been RT stored before the annealing.

According to APT findings, the sample with direct annealing has approx. 5 times more clusters than the sample with RT storage before the annealing [6]. It was shown that these are "good" clusters, being more compact (solute-rich) and having an Mg/Si ratio close to 1. The cluster sizes do not change between the two conditions. There should be no other differences between the conditions with and without RT storage, and what we observe with μSR is thus quite certainly caused by the composition, vacancy content and/or concentration of solute clusters.

The influence of microstructure on the μSR signal can be further deduced by the annealing temperature experiments on the Al–Mg–Si alloy (Fig. 6). The transition from a cluster-dominated microstructure (70 °C annealing) to a mixture of clusters and small, coherent precipitates causes no apparent difference in muon kinetics. However, annealing at 200 °C gives a lower trapping rate at measurement temperatures around 200 K. The annealing transforms some clusters/precipitates into larger, less coherent precipitates, some of which dissolve, thereby reducing the overall precipitate number density. The alloy conditions in the early stages of the precipitation sequence (Eq. (1)) are apparently the most efficient at trapping muons.

The insight gained from the experiments in this work is condensed in Fig. 9. Each nanosized defect in a material will give a "signature" in the muon trapping behaviour, which is characteristic of some kind of defect. The lower black line is what we expect the trapping rate to look like in 100% pure Al. Its inherent muon kinetics might include subtle effects of dislocations and grain boundaries. Trace/ impurity elements (brown line) and alloying elements (pink, dashed line), especially Mg (and Cu [17]), trap muons at low temperature. Trapping at temperatures close to 300 K (gray, dotted line) is observed in the non-annealed Al–0.5% Mg sample. As-quenched Al–Mg–Si samples also display elevated trapping in this region, and our previous in situ studies [15] show that this is also the case for AQ pure Al. A non-equilibrium (thermal) vacancy concentra-
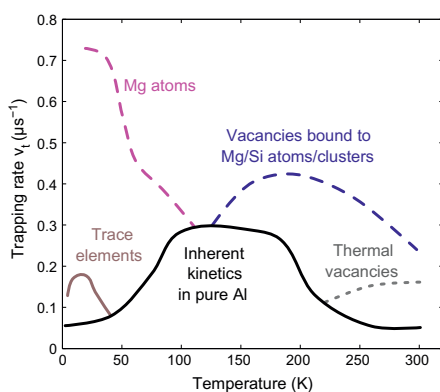
Fig. 9. Schematic of the signatures of defects on the muon trapping rate, as understood from Figs. 3, 5 and 6.

tion, introduced through SHT, is most likely responsible. The trapping peak around 200 K (blue, dashed line) was previously associated with clustering/precipitation [18]. It is the most interesting feature of the curves as it is observed exclusively in Al–Mg–Si samples and AQ Al–Si. We hypothesize that the trapping sites of this peak are vacancies in Mg/Si–rich environments – in particular, vacancies which are themselves trapped by clusters or precipitate phases. The muon trapping potential of such vacancies has not been investigated, but it is likely to be close to that of free vacancies in Al, given the much weaker muon (or hydrogen) interaction with Mg and Si atoms (see Table 2).

Figs. 5 and 6 show that AQ and RT stored Al–1.6% Mg$_2$Si samples have a reduced trapping rate at low temperatures as compared to Al–Mg and annealed Al–Mg–Si samples. Why Mg atoms should have a lower muon trapping potential in these conditions is not clear at this point, though it might be related to the change in solute atom distribution through clustering.

6.2. Vacancy behaviour during heat treatment

According to the calculated binding energies in Table 2, muons are preferentially located at interstitial sites next to a vacancy, though the concentration of vacancies is always very low compared to e.g. solute atoms. A high temperature is required to increase the muon diffusivity and break them loose from other defects so that they are able to find vacancies to bind to. Assuming the interpretation of the 200 K peak from the previous subsection (muon trapping by vacancies in solute-rich environments), we can draw some conclusions about the behaviour of vacancies in Al alloys.

Around 200 K, muons seem to have a strong bond with the Si–vacancy clusters formed after quenching from SHT (see Fig. 3(b)). After 12 days at RT, the trapping peak disappears, while it lasts indefinitely in Al–Mg–Si alloys, regardless of the heat treatment (Figs. 5 and 6). This means that, with the heat treatments done in this work, there are always some vacancies trapped in clusters and possibly early precipitate phases. The total number of vacancies inside Al–Mg–Si is then always greater than in pure Al, when the materials are treated equally. Fig. 10 shows the average trapping rate in the temperature interval 140–240 K for all Al–1.6% Mg$_2$Si conditions in Figs. 5 and 6. The typical microstructure for each condition is included, based on the current TEM analysis and previous analysis with TEM and APT of similar conditions [5,10,6,27,32]. The trapping maximum at an annealing temperature of 100 °C does not correspond directly to a maximum in any known microstructural parameter. In light of the preceding discussion, we nevertheless suggest that the vacancy concentration inside clusters/precipitates peaks at this point. It is possible that the ability of a precipitate to trap vacancies decreases when its coherency with Al decreases, and that it is also affected by the precipitate composition.

Although no current technique can probe the exact structure of nanoclusters, the good clusters might have a
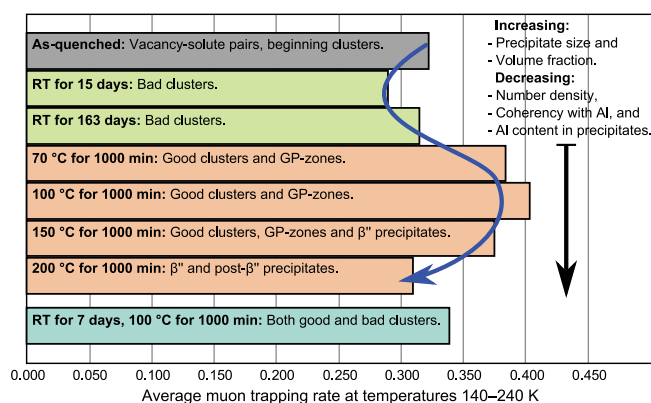

Fig. 10. Qualitative summary of the main trapping rate peaks of the Al–1.6% Mg$_2$Si samples in Figs. 5 and 6. The expected properties of the cluster/precipitate microstructure is given for each condition. GP zones are periodic solute-rich structures with Mg and Si atoms still at Al-fcc positions [32].

78

pre-β'' GP zone [32] structure at the moment they nucleate from the Al matrix. An indication of the presence of good and bad clusters is noted for each condition in Fig. 10, showing a good correspondence between good cluster content and muon trapping rate. Our interpretation is that muon-trapping vacancies reside in these clusters, which retain an Al-fcc structure. Once they transform into β'' and other phases, they lose their ability to contain vacancies, which lowers the muon trapping rate.

Diamond Si particles do not affect muon kinetics, and therefore do not trap vacancies. The equilibrium phase β in the Al–Mg–Si system, with the composition Mg_2Si, forms as big, incoherent cubes, similar to diamond Si. If β also does not trap vacancies, the blue peak in Fig. 9 should not be present in a sample containing only β. Such a very over-aged Al–1.6% Mg_2Si alloy should be studied in the future, as it could be an interesting test of our interpretation.

7. Conclusion

An extensive study on the muon behaviour in Al–Mg–Si, Al–Mg, Al–Si and pure aluminium has been conducted. Heat treatments were designed for the investigation of diffusion and clustering phenomena in different stages of the precipitation, which is crucial to the properties of commercial Al–Mg–Si alloys. We have shed light on some important findings regarding the muon trapping in the materials and its interpretation in terms of (sub-) nanometer-sized defect content. In particular, muons were found to prefer the company of Mg atoms over Si atoms, as was predicted by DFT calculations. The vacancy kinetics are surprisingly different in the two binary alloys. In Al–Si, Si–vacancy clusters form, but vacancies still leave the material faster in Al–Si than in Al–Mg. A characteristic peak in the muon trapping rate is seen in Al–Mg–Si in the temperature range 100–250 K, regardless of heat treatment. Since there are many steps of reasoning in our analysis of this peak, we summarize it here in a bottom-up order:

1. Annealing an Al–1.6% Mg_2Si alloy at 70–150 °C for 1000 min produces a fine microstructure of "good" (see Section 6.2) clusters and GP zones, with Mg and Si atoms retaining Al-fcc positions. This has been well established by numerous earlier APT and TEM investigations.
2. These structures trap a greater number of vacancies than bulk Al and precipitates with a non-fcc structure. This is the main hypothesis of this paper.
3. Muon–vacancy bonds have a high binding energy, as found by the current DFT calculations as well as μSR experiments on Al (–Mg)(–Si) alloys.
4. The trapping of muons by vacancies inside good clusters/GP zones occurs when the alloy sample is kept at temperatures in the range 100–250 K.

5. This trapping increases the muon depolarization rate. The steepness of the relaxation functions (Fig. 1) at the temperatures in question can thus be linked to the presence of good clusters/GP zones.

Two transitions are observed in the muon trapping rate when changing the annealing temperature: an increase between room temperature and 70 °C and a decrease between 150 and 200 °C. These transitions indicate the appearance of good clusters/GP zones, and their disappearance is associated with over-aging.

Muon spin relaxation has proved to be sensitive to very small concentrations of defects important for diffusional phase transformations. It is complementary to more established techniques such as TEM, APT and DSC, and has the potential to aid our understanding and development of aluminium alloys.

References

[1] Kubo R, Toyabe T. In: Blinc R, editor. Magnetic resonance and relaxation. Amsterdam: North-Holland; 1967. p. 810.
[2] Davis JR, editor. Aluminum and aluminum alloys. Materials Park, OH: ASM International; 1993.
[3] Ferragut R, Dupasquier A, Macchi CE, Somoza A, Lumley RN, Polmear IJ. Scripta Mater 2009;60(3):137–40.
[4] Banhart J, Lay MDH, Chang CST, Hill AJ. Phys Rev B 2011;83:014101.
[5] Serizawa A, Hirosawa S, Sato T. Metall Mater Trans A 2008;39:243–51.
[6] Torsæter M, Hasting HS, Lefebvre W, Marioara CD, Walmsley JC, Andersen SJ, et al. J Appl Phys 2010;108(7):073527.
[7] De Geuser F, Lefebvre W, Blavette D. Phil Mag Lett 2006;86(4):227–34.
[8] Zhen L, Kang S. Mater Lett 1998;37(6):349–53.
[9] Chang CST, Banhart J. Metall Mater Trans A 2011;42:1960–4.
[10] Torsæter M. PhD thesis. Norwegian University of Science and Technology; 2011.
[11] Martinsen FA, Ehlers FJH, Torsæter M, Holmestad R. Acta Mater 2012;60(17):6091–101.
[12] Zandbergen HW, Andersen SJ, Jansen J. Science 1997;277(5330):1221–5.
[13] Marioara CD, Andersen SJ, Zandbergen H, Holmestad R. Metall Mater Trans A 2005;36:691–702.
[14] Kehr KW, Richter D, Welter JM, Hartmann O, Karlsson E, Norlin LO, et al. Phys Rev B 1982;26:567–90.
[15] Wenner S, Matsuda K, Nishimura K, Banhart J, Matsuzaki T, Tomono D, et al. In: Heiland W, Rollett AD, Cassada W, editors. 13th International conference on aluminum alloys. Wiley; 2012. p. 37–42.
[16] Marioara CD, Andersen SJ, Birkeland A, Holmestad R. J Mater Sci 2008;43:4962–71.

[17] Doyama M, Hatano T, Natsui T, Suzuki Y, Uemura YJ, Yamazaki T, et al. Hyperfine Interact 1984;17:225–9.

[18] Wenner S, Holmestad R, Matsuda K, Nishimura K, Matsuzaki T, Tomono D, et al. Phys Rev B 2012;86:104201.

[19] Yaouanc A, De Réotier PD. Muon spin rotation, relaxation, and resonance: applications to condensed matter. Oxford: Oxford University Press; 2011.

[20] Garwin RL, Lederman LM, Weinrich M. Phys Rev 1957;105:1415–7.

[21] Hayano RS, Uemura YJ, Imazato J, Nishida N, Yamazaki T, Kubo R. Phys Rev B 1979;20:850–9.

[22] Boekema C, Heffner RH, Hutson RL, Leon M, Schillaci ME, Kossler WJ, et al. Phys Rev B 1982;26:2341–8.

[23] Borghini M, Niinikoski TO, Soulié JC, Hartmann O, Karlsson E, Norlin LO, et al. Phys Rev Lett 1978;40:1723–6.

[24] Hartmann O, Karlsson E, Norlin LO, Niinikoski TO, Kehr KW, Richter D, et al. Phys Rev Lett 1980;44:337–40.

[25] Schenck A. Muon spin rotation spectroscopy. Bristol: Adam Hilger; 1985.

[26] Matsuzaki T, Ishida K, Nagamine K, Watanabe I, Eaton GH, Williams WG. Nucl Instr Methods A 2001;465(2–3):365–83.

[27] Wenner S, Marioara CD, Andersen SJ, Holmestad R. Int J Mater Res 2012;103:948–54.

[28] Kresse G, Hafner J. Phys Rev B 1993;47:558–61.

[29] Kresse G, Furthmüller J. Comput Mater Sci 1996;6(1):15–50.

[30] Hohenberg P, Kohn W. Phys Rev 1964;136:B864–71.

[31] Kohn W, Sham LJ. Phys Rev 1965;140:A1133–8.

[32] Marioara CD, Andersen SJ, Jansen J, Zandbergen HW. Acta Mater 2001;49(2):321–8.

[33] Murayama M, Hono K. Acta Mater 1999;47(5):1537–48.

[34] Liu M, Yan Y, Liang Z, Chang CST, Banhart J. In: Heiland W, Rollett AD, Cassada W, editors. 13th International conference on aluminum alloys. Wiley; 2012. p. 1131–6.

[35] Kim SM, Buyers WJL, Martel P, Hood GM. J Phys F Metal Phys 1974;4(3):343.

[36] Hirosawa S, Nakamura F, Sato T. Mater Sci Forum 2007;561–565:283–6.

Paper 3

Effect of room temperature storage time on precipitation in Al–Mg–Si(–Cu) alloys with different Mg/Si ratios

S. Wenner, C. D. Marioara, S. J. Andersen and R. Holmestad

Sigurd Wenner[a], Calin Daniel Marioara[b], Sigmund Jarle Andersen[b], Randi Holmestad[a]
[a] Norwegian University of Science and Technology, Department of Physics, Trondheim, Norway
[b] SINTEF, Materials and Chemistry, Trondheim, Norway

Effect of room temperature storage time on precipitation in Al–Mg–Si(–Cu) alloys with different Mg/Si ratios

Paper presented at the first European Conference on Aluminium Alloys (ECAA), October 5–7, 2011, Bremen, Germany
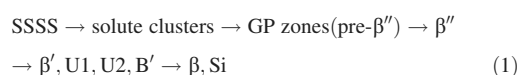
The effect of natural ageing time before artificial ageing has been investigated in four Al–Mg–Si(–Cu) alloys, with 0.4 % Mg + 0.8 % Si and 0.8 % Mg + 0.4 % Si, both with and without 0.14 at.% Cu. The precipitate microstructure was quantified by means of transmission electron microscopy. Varying the storage time before ageing for 170 min at 200 °C, we observe an initial hardness increase after minutes, a decrease after several hours and another increase after weeks. The hardness decrease was most pronounced in the Mg-rich Cu-free alloy, caused by a reduced precipitate volume fraction. Adding Cu produces finer microstructures, higher hardness and reduces the negative effect of natural ageing regardless of the Mg/Si ratio of the alloy. With 1 week storage, an increase in the fraction of the Cu-containing precipitates L and Q′ was observed in the Cu-containing Si-rich and Mg-rich alloys respectively.

Keywords: Al–Mg–Si; Precipitation; Natural ageing; Transmission electron microscopy; Hardness
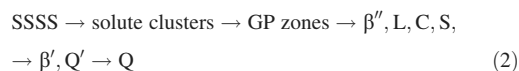
1. Introduction

The 6xxx series aluminium alloys, with magnesium and silicon as primary alloying elements, are widely used in the automotive industry and as structural materials. They acquire medium strength via the formation of metastable precipitate phases during heat treatment. During solution heat treatment (SHT) at a temperature between the solubility limit of the alloying elements and the eutectic temperature, a solid solution is created, where evenly distributed Mg and Si atoms occupy substitutional Al fcc lattice positions. After cooling to room temperature (RT), a highly unstable supersaturated solid solution (SSSS) is formed, retaining 1–3 at.% solutes in 6xxx alloys. Owing to the quenched-in vacancy supersaturation, solute atoms will diffuse and form clusters at RT. This is referred to as natural ageing (NA). Upon subsequent artificial ageing (AA) at medium temperatures (~170 °C), metastable precipitates will form with structures different from, but partially coherent with, the Al matrix. All metastable precipitates in the Al–Mg–Si(–Cu) system have needle/rod/lath/plate shapes with main growth directions parallel to $<001>_{Al}$, which also coincide with the full coherency direc-

tions. In Al–Mg–Si alloys, the precipitation sequence is: [1–3]

$$SSSS \rightarrow \text{solute clusters} \rightarrow \text{GP zones(pre-}\beta'') \rightarrow \beta''$$

$$\rightarrow \beta', U1, U2, B' \rightarrow \beta, Si \qquad (1)$$

The Guinier–Preston (GP) zones are in this alloy system needle-shaped agglomerations of solute atoms still occupying Al fcc lattice positions [4]. Si-rich alloys favour the formation of GP zones (pre-β''), which promote a better thermal stability as compared to Mg-rich alloys [5]. The needle-like β'' phase is fully coherent with the matrix and responsible for the peak hardness of Al–Mg–Si alloys [5, 6]. The later phases in the sequence are less coherent, up to the incoherent equilibrium phase β [7]. Upon over-ageing, a combination of U2 and β′ phases has been observed for alloys with Mg/Si ratios close to 1, while a combination of large U1 and small B′ phases has been observed for Si-rich alloys [7]. The formation of GP zones is prevented in Mg-rich alloys which achieve one main hardness peak due to the formation of β'' phase [5]. These alloys overage faster and produce coarse β′ microstructures [7].

Many industrial 6xxx alloys contain small amounts of copper as an additional alloying element. This is known to increase hardness due to the formation of several types of Cu-containing semi-coherent precipitate phases in the peak hardness condition, many of them with disordered structures [8]. The precipitation sequence for Al–Mg–Si–Cu alloys is:

$$SSSS \rightarrow \text{solute clusters} \rightarrow \text{GP zones} \rightarrow \beta'', L, C, S,$$

$$\rightarrow \beta', Q' \rightarrow Q \qquad (2)$$

Earlier studies comprising alloys with solute content (Mg + Si) = 1.3 at.% and 0.13 at.% Cu additions indicate that the types of metastable precipitates which are formed have a weaker dependency on the Mg/Si ratio [8] when compared to precipitates in corresponding Cu-free alloys [5, 7]. In 6xxx alloys, NA before AA can have both a positive and negative effect on hardness, depending on the alloy composition and the NA time [9, 10]. An addition of Cu has been found to reduce the negative effect [11–13]. In the case of the alloys used in the present study, which have a total solute amount above 1 at.%, RT storage between SHT and AA is expected to cause a decrease in hardness after AA [5, 14].

NA is a complicated and poorly understood phenomenon that may be ascribed to a number of competing nanoscale processes happening at different rates and with different effects on hardness and other measurable global quantities [15]. The processes have been attributed to the formation of different types of solute clusters [16]. This is known to affect the precipitation during subsequent AA [9]. The importance of NA comes from the fact that it cannot be completely avoided in industrial practice.

In this paper we present hardness and microstructure investigations of four different alloys as a function of NA time before artificial ageing. The alloys are Mg-rich and Si-rich both with and without Cu additions. The total solute amount is nearly equal in all alloys, and at a level that usually gives a negative effect on hardness during AA following NA [9]. Transmission electron microscopy (TEM) has been used to identify precipitate types and to characterise them according to average length, cross-section, number density and volume fraction. This is used to explain the features of the hardness curves obtained by varying RT storage time between SHT and AA.

2. Experimental procedure

Four ultra-pure alloys were used in the study, A2 and A11 having (Mg + Si) $\approx$ 1.3 at.% with respective Mg/Si ratios 0.5 and 2.0, and their Cu-containing equivalents A2Cu and A11Cu having 0.14 at.% Cu additions. The exact compositions, determined using X-ray microprobe measurements, are given in Table 1. Samples of each alloy were prepared from extruded bars with cross-section dimensions 1.8 mm $\times$ 24 mm. SHT was conducted in salt furnaces for 1 h at a temperature of $540 \pm 1\,°C$. The samples were quenched in $19 \pm 1\,°C$ water and stored at RT for variable time (< 5 s to 1 year). Subsequent AA was done in baths of silicon oil for 170 min at a temperature of $200 \pm 1\,°C$. This is known to produce a condition close to the peak-aged one for these alloys.

Hardness was measured both during NA and after AA. In this way the hardness increase due to the presumed atomic cluster formation taking place during RT storage was monitored, as well as the effect of these clusters on subsequent ageing. Before hardness measurements, samples were polished using a fine (P4000) grinding paper. All Vickers hardness measurements were conducted with a Matsuzawa DVK-1S using 100 μm s^{-1} loading speed for the diamond tip and 5 kg applied force for 15 ms. 10 indentations were made for each measurement.

TEM specimens were made from AA samples naturally aged for < 5 s (denoted AA) and 1 week (denoted NA + AA). These two conditions were chosen to compare the effect of no RT storage with a storage that gives a de-

crease in the hardness after the AA (negative effect of RT storage). Foils were polished to a thickness of 50–150 μm and punched into 3 mm discs. The discs were electropolished using a Struers Tenupol-5 and immediately cleaned in methanol and ethanol. TEM investigations were conducted using a Philips CM30 TEM operated at 150 kV. Due to the orientation and the coherency of the metastable phases with respect to the Al matrix, all TEM investigations were performed in a <001>$_{Al}$ type zone axis. TEM negatives were exposed, scanned and used for precipitate characterisation. A post-column Gatan parallel EELS system was used to measure the sample thickness where each negative was taken. After manually marking the precipitates on each negative, a Matlab script was used for computing the average precipitate cross-section area, length and number density. The product of these quantities gives the precipitate volume fraction. The length and number density were corrected for specimen tilt and the fraction of precipitates near the surface that were cut shorter during electropolishing using statistical considerations. A more detailed description of the methodology used can be found elsewhere [5]. The average characteristics of the precipitates (Table 2) were calculated from roughly 300 cross-sections, 1 000 lengths and 1 000 particle counts for each condition. The sample thickness at locations of the exposed negatives was in the range 30–110 nm. Precipitate types can be determined from high-resolution images of precipitates viewed in cross-section (along their main growth direction) due to the fact that their lengths are comparable to the thickness of the analysed TEM sample. Phases were identified based on their dimensions and/or the crystallographic orientations of their interfaces [8, 17]. Determining the type of a precipitate is evidently much harder when its main growth direction is perpendicular to the viewing direction, due to overlap with Al. Therefore, precipitates with similar cross-section areas in Table 2 have been assumed to have the same average length. Similar phase identifications have been performed in another study [7].

3. Results

Hardness results are given in Figs. 1 and 2, with logarithmic RT storage time axes. The hardness increases monotonically for all alloys during NA (Fig. 1). It is roughly doubled from short (~20 min) to long (~1 year) RT storage times. For storage times less than 10 hours, the slope is similar for all alloys, though after roughly 100 h the Cu-containing alloys are systematically stronger. A small drop in hardness of the Cu-free alloys is observed around 300 h.

Figure 2 shows the effect of various RT storage times (indicated in Fig. 1) on the hardness measured after AA for

Table 1. Compositions of the alloys used in the study, measured by X-ray microprobe. Statistical errors from 10 measurements on the same samples are given.

Alloy	Si (at.%)	Mg (at.%)	Cu (at.%)	Total (at.%)	Mg/Si (wt.%)
A2	0.802 ± 0.008	0.443 ± 0.004	0.003 ± 0.001	1.247 ± 0.009	0.478 ± 0.009
A11	0.399 ± 0.009	0.937 ± 0.014	0.003 ± 0.002	1.339 ± 0.016	2.032 ± 0.016
A2Cu	0.847 ± 0.010	0.539 ± 0.003	0.145 ± 0.004	1.531 ± 0.012	0.551 ± 0.010
A11Cu	0.419 ± 0.007	0.912 ± 0.007	0.135 ± 0.005	1.466 ± 0.011	1.884 ± 0.010

Table 2. Quantification of the precipitate phases in the eight conditions studied. (a) Artificially aged for 170 min at 200 °C within 5 s after the solution heat treatment. (b) Solution heat treated, stored at room temperature for 1 week and artificially aged for 170 min at 200 °C.

Condition	Precipitate	Cross-section (nm^2)	Length (nm)	Number density (1 000 μm^{-3})	Volume fraction (%)
A2 (AA)	β″	11.7 ± 0.3	39.3 ± 2.0	26.1 ± 1.6	1.19 ± 0.10
	Total			**26.1 ± 1.6**	**1.19 ± 0.10**
A11 (AA)	β″	17.9 ± 0.6	26.3 ± 2.2	22.2 ± 2.5	1.05 ± 0.15
	Over-aged (B′)	12.1 ± 0.8	26.3 ± 2.2	6.0 ± 0.6	0.19 ± 0.03
	Total			**28.3 ± 2.6**	**1.24 ± 0.15**
A2Cu (AA)	β″	7.5 ± 0.1	22.5 ± 1.0	40.7 ± 4.3	0.69 ± 0.08
	L	8.0 ± 1.4	67.9 ± 20.5	1.6 ± 0.2	0.08 ± 0.03
	Q′	10.9 ± 2.0	67.9 ± 20.5	1.3 ± 0.1	0.10 ± 0.04
	Disordered	6.8 ± 0.2	22.5 ± 1.0	22.0 ± 2.3	0.34 ± 0.04
	Total			**65.6 ± 4.8**	**1.20 ± 0.10**
A11Cu (AA)	β″	11.1 ± 0.3	17.0 ± 0.7	32.1 ± 3.4	0.60 ± 0.07
	L	12.7 ± 0.3	49.2 ± 8.9	1.4 ± 0.2	0.09 ± 0.03
	Q′	11.8 ± 1.5	49.2 ± 8.9	1.1 ± 0.1	0.06 ± 0.02
	Disordered	9.1 ± 0.6	17.0 ± 0.7	12.6 ± 1.3	0.20 ± 0.03
	Total			**47.2 ± 3.6**	**0.95 ± 0.08**

(a)

| Condition	Precipitate	Cross-section (nm^2)	Length (nm)	Number density (1 000 μm^{-3})	Volume fraction (%)
A2 (NA + AA)	β″	8.1 ± 0.2	37.8 ± 1.1	35.9 ± 3.8	1.10 ± 0.12
	Total			**35.9 ± 3.8**	**1.10 ± 0.12**
A11 (NA + AA)	β″	13.1 ± 0.6	20.7 ± 1.4	20.2 ± 2.1	0.55 ± 0.07
	Over-aged (β′)	27.7 ± 2.2	139.9 ± 18.6	0.7 ± 0.1	0.28 ± 0.05
	Total			**21.0 ± 2.1**	**0.83 ± 0.09**
A2Cu (NA + AA)	β″	7.2 ± 0.2	21.8 ± 1.1	22.7 ± 2.8	0.36 ± 0.05
	L	5.3 ± 0.3	65.6 ± 5.1	9.9 ± 1.2	0.35 ± 0.05
	Q′	7.7 ± 1.0	65.6 ± 5.1	1.2 ± 0.1	0.06 ± 0.01
	Disordered	6.8 ± 0.2	21.8 ± 1.1	27.4 ± 3.3	0.40 ± 0.05
	Total			**61.2 ± 4.5**	**1.17 ± 0.09**
A11Cu (NA + AA)	β″	10.9 ± 0.3	21.1 ± 1.3	24.0 ± 2.6	0.55 ± 0.07
	L	7.8 ± 1.4	39.4 ± 8.3	2.1 ± 0.2	0.06 ± 0.02
	Q′	12.2 ± 0.9	39.4 ± 8.3	4.0 ± 0.4	0.19 ± 0.05
	Disordered	9.5 ± 0.5	21.1 ± 1.3	14.7 ± 1.6	0.30 ± 0.04
	Total			**44.9 ± 3.0**	**1.11 ± 0.10**

(b)
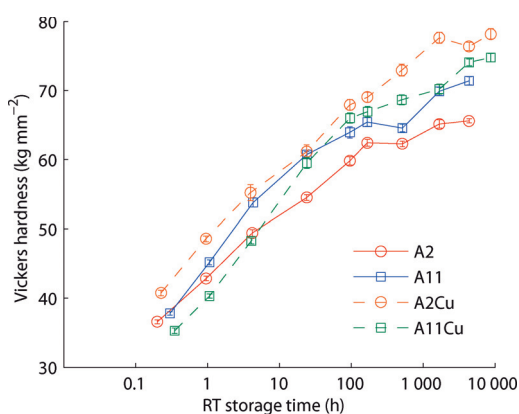
Fig. 1. Vickers hardness evolution during natural ageing (room temperature storage) for up to 1 year after solution heat treatment.

170 min at 200 °C. The key properties of the hardness curves are:
- The Cu-containing alloys clearly have a (10–20 %) higher strength than their Cu-free equivalents, for all investigated NA times.
- All four alloys display similar stages of variation in the AA hardness as function of RT storage time. The hardness curves are characterised by an initial increase corresponding to a few minutes of RT storage followed by a hardness decrease that lasts up to more than 100 h and then by a final hardness increase which may correspond to the small drop in NA hardness at about 300 h. At very long RT storage times (months) the hardness in AA samples seems to decrease again for the Cu-free alloys.
- The first (main) hardness drop is most pronounced in the Cu-free Mg-rich alloy (A11). The minimum hardness is achieved between 1 h and 200 h for this alloy.
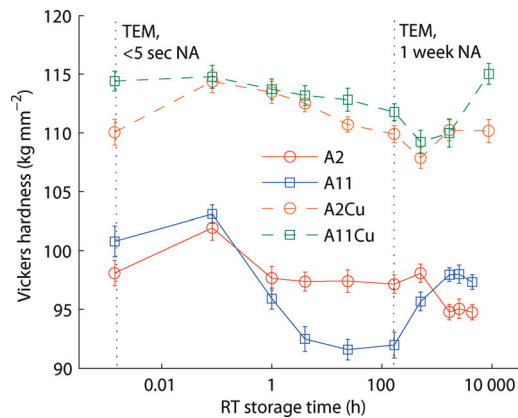
Fig. 2. Vickers hardness after a varying room temperature storage time (up to 1 year) and subsequent (fixed) artificial ageing for 170 min at 200 °C. The vertical dotted lines denote the conditions studied using transmission electron microscopy.

- In the case of the Cu-containing alloys, the effect of RT storage is weaker and less dependent on the Mg/Si ratio of the alloy. The main decrease and final increase in hardness occur after longer RT storage times. Specifically, the hardness of both alloys drops between 5 min and 500 h, and increases again after 500 h.

Figure 3 shows typical low magnification bright-field TEM images used for the microstructure quantification in each of the eight TEM conditions, corresponding to the four alloys kept for only seconds at RT and for 1 week at RT before given the final AA of 170 min at 200 °C. Figure 4 shows examples of phase identification, based on high magnification bright-field TEM images recorded from precipitates viewed in cross-section. The phases are quantified in Table 2. Figure 5 displays the absolute volume fraction of the precipitates. The following observations can be drawn:

- The large drop in hardness for the Mg-rich Cu-free alloy A11 after 1 week of RT storage correlates with a reduction in precipitate volume fraction and number density concomitant with microstructure over-ageing and formation of the β′ phase (see Fig. 5) that has a low hardening potential [7]. Although the microstructure becomes finer after 1 week RT storage for the Si-rich Cu-free alloy A2 (that should increase the hardness), the hardness is similar to the condition with very short RT storage.
- The Cu-containing alloys generally have a higher precipitate number density than the Cu-free alloys, corresponding with a higher overall hardness achieved (Fig. 2).
- The Cu-containing alloys have large fractions of disordered precipitates (see Fig. 5), many containing β″ unit cells (see Fig. 4), at both short and long RT storage times. However, after 1 week of RT storage a clear increase in the Cu-containing precipitates L and Q′ is observed in alloys A2Cu and A11Cu respectively (see Fig. 5).
- In general, Fig. 5 shows that the relative fraction of β″ phase is lower after 1 week RT storage as compared to very short storage for all four alloys. Also, the fraction of β″ is lower in the case of Cu-containing alloys.

4. Discussion

From the hardness curves in Figs. 1 and 2, it is evident that several competing processes occur during NA, with different effects on hardness and precipitation that take place during the subsequent AA. These have earlier been attributed to mono- and hetero-clustering of solute elements, also denoted "bad" and "good" clusters, respectively [16, 18, 19]. In the case of Cu-free alloys it has been shown that Mg–Si clustering is a slow process, while clusters that are either Si-rich or Mg-rich form faster. It can therefore be speculated that the initial hardness increase in the AA conditions (Fig. 2) corresponding to very short RT storage and the hardness decrease that follows is the result of mono-clustering, while the final hardness increase is the result of Mg–Si co-clustering. The temporary drop/stagnation in NA hardness (Fig. 1) at 300 h can be another effect of this last process. Recent atom probe tomography work using the A2 and A11 alloy compositions [14] has demonstrated the presence of large fractions of Si-rich clusters that form during NA in Si-rich alloys, and corresponding Mg-rich clusters in Mg-rich alloys. In the same work Mg–Si co-clustering was observed in pre-aged conditions regardless of the RT storage time. The lower sensitivity of the Cu-free Si-rich alloy A2 to the RT storage time could be connected to previous results [5] showing that Si-rich alloys are more stable during isothermal heat treatments by retaining fine microstructures of β″ phase. Indeed Fig. 5 shows that the relative fraction of this phase is highest in alloy A2. Marioara et al. [5] found that Mg-rich alloys overage faster and with a high volume fraction of the less coherent β′ phase, which is confirmed in this work. Interestingly, in all four alloys it seems the over-ageing process is accelerated when the NA time is increased. The fact that the Cu-free Mg-rich alloy A11 is more negatively influenced by RT storage may indicate that the Mg-rich clusters that form during short times of RT storage are more detrimental to nucleation during AA than the Si-rich clusters that form in alloy A2, which would explain the observation of fewer and larger precipitates. It should be noted that earlier differential scanning calorimetry (DSC) investigations show no variations in the peak associated with β″ formation with NA time for two (denser) Al–Mg–Si alloys [20].

Previous work has shown that when Cu is added to the Al–Mg–Si system the precipitation sequence changes and new phases form [8]. This effect is associated with a decrease in the fraction of β″ particles, which are no longer the only hardening precipitates in these alloys. Moreover, Cu-containing alloys produce higher precipitate number densities that usually lead to higher hardness. This development is also observed in the present work, and may provide a likely explanation for the overall superior hardness of A2Cu and A11Cu. An interesting feature of the Cu-containing alloys is that NA has a reduced effect on the AA hardness response, which hardly depends on the Mg/Si ratio of the alloy. This, together with the observation that an increasing fraction of Cu-containing precipitates is observed with 1 week of RT storage suggests that Cu is preventing the detrimental effect by being incorporated in "good" clusters that would have otherwise been "bad", regardless of alloy Mg/Si ratio.

This work has demonstrated that RT storage is a very important parameter that cannot be ignored in industrial pro-
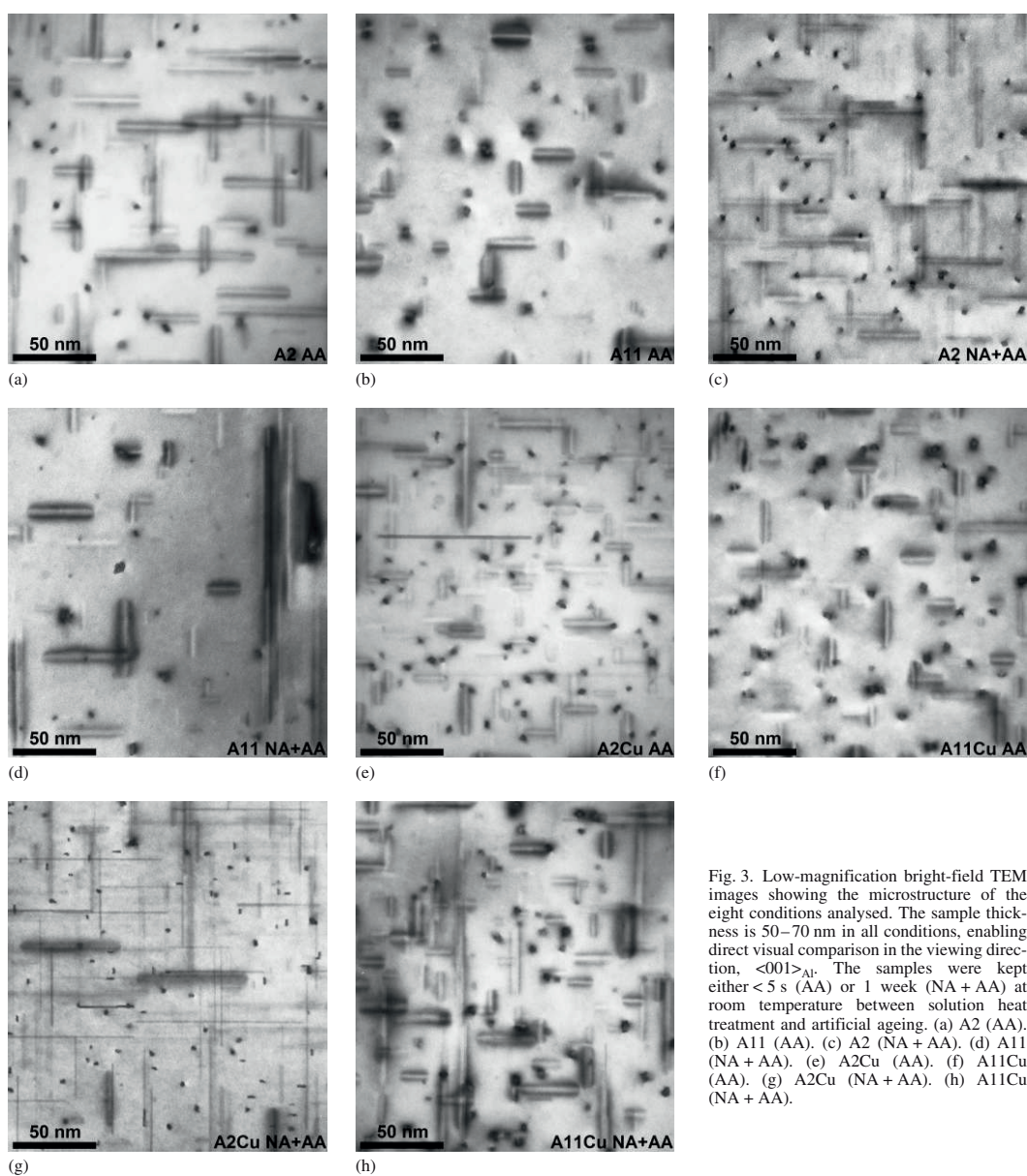
Fig. 3. Low-magnification bright-field TEM images showing the microstructure of the eight conditions analysed. The sample thickness is 50–70 nm in all conditions, enabling direct visual comparison in the viewing direction, $<001>_{Al}$. The samples were kept either < 5 s (AA) or 1 week (NA + AA) at room temperature between solution heat treatment and artificial ageing. (a) A2 (AA). (b) A11 (AA). (c) A2 (NA + AA). (d) A11 (NA + AA). (e) A2Cu (AA). (f) A11Cu (AA). (g) A2Cu (NA + AA). (h) A11Cu (NA + AA).

cedures or applications where increased control of precipitate microstructure and mechanical properties is required. Further work is needed in order to understand the processes that occur at the atomic level during the RT storage and how these early atomic clusters influence precipitation during the subsequent AA. For example, one intriguing observation in this work is the second hardness decrease at NA times corresponding to several months for the Cu-free alloys.

5. Conclusions

The effect of room temperature storage times of up to one year on hardness and precipitation after a subsequent AA has been analysed for four Al–Mg–Si(–Cu) alloys. Based on the hardness of the AA conditions, three main development stages are identified that correspond to an initial hardness increase during very short (seconds or minutes) RT storage, a hardness decrease during hours of RT storage
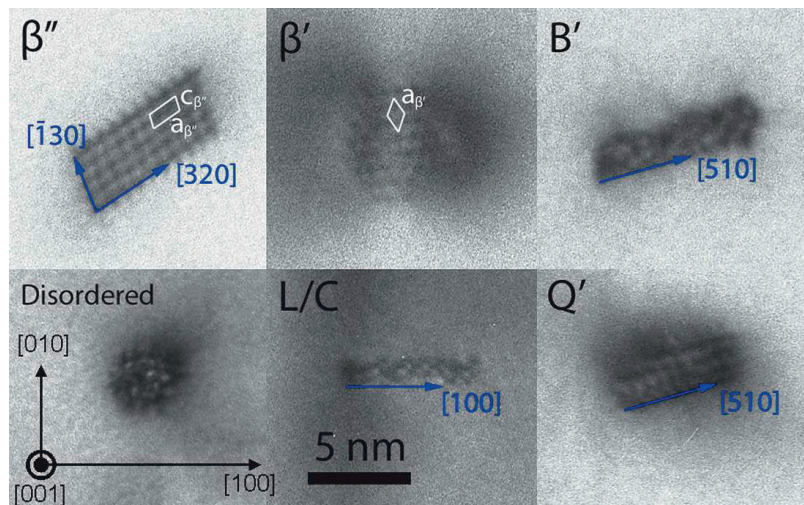
Fig. 4. Examples of precipitate phases observed in high-resolution bright-field TEM images and quantified by cross-sectional area and relative fraction. The arrows refer to directions in the Al lattice.
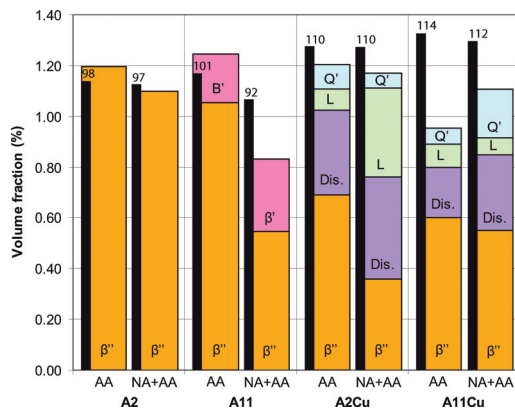

Fig. 5. Volume fractions of each precipitate type in each of the eight conditions analysed. Plotted from data in Table 2. The black columns show the hardness, with values in kg mm^{-2}.

The latter finding suggests that Cu is involved in the precipitation already during the formation of atomic clusters at RT.

References

[1] G.A. Edwards, K. Stiller, G.L. Dunlop, M.J. Couper: Mater. Sci. Forum 217–222 (1996) 713–718.
[2] K. Matsuda, Y. Sakaguchi, Y. Miyata, Y. Uetani, T. Sato, A. Kamio, S. Ikeno: J. Mater. Sci. 35 (2000) 179–189. DOI:10.1023/A:1004769305736
[3] S.J. Andersen, C.D. Marioara, A. Frøseth, R. Vissers, H.W. Zandbergen: Mater. Sci. Eng. A 390 (2005) 127. DOI:10.1016/j.msea.2004.09.019
[4] C.D. Marioara, S.J. Andersen, J. Jansen, H.W. Zandbergen: Acta Mater. 49/2 (2001) 321–328, ISSN 1359–6454.
[5] C.D. Marioara, S.J. Andersen, H.W. Zandbergen, R. Holmestad: Met. Mater. Trans. A 36 A (2005) 691–702, ISSN: 1073–5623.
[6] H.W. Zandbergen, S.J. Andersen, J. Jansen: Science 277 (1997) 1221. DOI:10.1126/science.277.5330.1221
[7] C.D. Marioara, H. Nordmark, S.J. Andersen, R. Holmestad: J. Mater. Sci. 41 (2006) 471–478, ISSN 1573–4803.
[8] C.D. Marioara, S.J. Andersen, T.N. Stene, H. Hasting, J.C. Walmsley, A.T.J. van Helvoort, R. Holmestad: Phil. Mag. 87 (2007) 3385–3413. DOI:10.1080/14786430701287377
[9] C.D. Marioara, S.J. Andersen, J. Jansen, H.W. Zandbergen: Acta Mater. 51 (2003) 789–796. DOI:10.1016/S1359-6454(02)00470-6
[10] C.S.T. Chang, I. Wieler, N. Wanderka, J. Banhart: Ultramicroscopy 109 (2009) 585–592. PMid:19162402; DOI:10.1016/j.ultramic.2008.12.002
[11] D.W. Pashley, J.W. Rhodes, A. Sendorek: J. Inst. Met. 94 (1966) 41.
[12] M. Murayama: Metal. Mater. Trans. A 32 (2001) 239. DOI:10.1007/s11661-001-0254-z
[13] J.E. Janse, L. Zhuang, J. Mooi, P. De Smet: Mater. Sci. Forum 396–402 (2002) 607–612.
[14] M. Torsæter, H.S. Hasting, W. Lefebvre, C.D. Marioara, J.C. Walmsley, S.J. Andersen, R. Holmestad: J. Appl. Phys. 108 (2010) 073527. DOI:10.1063/1.3481090
[15] J. Banhart, C.S.T. Chang, Z. Liang, N. Wanderka, M.D.H. Lay, A.J. Hill: Proc. 12th Intern. Conf. on Aluminium Alloys, Yokohama (2010) 381–388.

and a final hardness increase after 100–500 h at RT. There are indications that a fourth stage corresponding to a second hardness decrease is taking place at very long RT storage times (months) in the Si-rich Cu-free alloy A2. The negative effect of RT storage time is most pronounced in the case of the Mg-rich Cu-free alloy A11. Adding Cu reduces the negative effect and makes it less sensitive to the alloy Mg/Si ratio.

Microstructure investigations show that the hardness decrease during the negative effect is caused by a reduction in precipitate number density and/or a decrease in precipitate volume fraction. Moreover, the Cu-containing alloys produce higher precipitate number densities, which provide a likely explanation for the overall superior hardness of A2Cu and A11Cu. With increasing RT storage time, the relative fraction of β″ phase decreases while other precipitates form, such as β′ in A11 and the Cu-containing L and Q′ phases in the alloys A2Cu and A11Cu, respectively.

[16] A.K. Gupta, D.J. Lloyd: Met. Mater. Trans. A 30 (1999) 879–884.
[17] S. Gulbrandsen-Dahl, K.O. Pedersen, C.D. Marioara, M. Kolar, K. Marthinsen: Aluminium Alloys, Their Physical and Mechanical Properties, Wiley-VCH, Weinheim (2008) 1634–1640.
[18] G.A. Edwards, K. Stiller, G.L. Dunlop, M.J. Couper: Acta Mater. 46 (1998) 3893–3904.
    DOI:10.1016/S1359-6454(98)00059-7
[19] M. Murayama, K. Hono: Acta Mater. 47 (1999) 1537.
    DOI:10.1016/S1359-6454(99)00033-6
[20] L. Zhen, S.B. Kang: Mater. Lett. 37 (1998) 349–353.
    DOI:10.1016/S0167-577X(98)00118-9

Bibliography

Correspondence address

Mr. Sigurd Wenner
Department of Physics, NTNU,
Høgskoleringen 5, N-7491 Trondheim, Norway
Tel.: +47 73590730
Fax: +47 73597710
E-mail: sigurd.wenner@ntnu.no

You will find the article and additional material by entering the document number **MK110795** on our website at *www.ijmr.de*

How calcium prevents precipitation hardening in Al–Mg–Si alloys

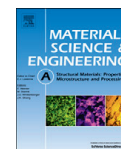S. Wenner, C. D. Marioara , S. J. Andersen and R. Holmestad

Paper 4

How calcium prevents precipitation hardening in Al–Mg–Si alloys

Sigurd Wenner [a],*, Calin D. Marioara [b], Sigmund J. Andersen [b], Randi Holmestad [a]

[a] Department of Physics, NTNU, Høgskoleringen 5, NO-7491 Trondheim, Norway
[b] Materials and Chemistry, SINTEF, Box 4760 Sluppen, NO-7465 Trondheim, Norway

ARTICLE INFO

ABSTRACT

We have investigated the effect on precipitate microstructure and hardness upon adding small amounts of Ca to a base Al–Mg–Si alloy. The main investigative techniques were transmission and scanning electron microscopy. We found that large Ca-containing particles with composition $CaAl_2Si_2$ form during the production stages of the alloy. The particles leave less Si available in solid solution for the nucleation of hardening precipitates, leading to a coarser microstructure consisting of less coherent precipitates. The resulting hardness decrease is measurable for alloys containing more than 60 at ppm of Ca.

© 2013 Elsevier B.V. All rights reserved.

1. Introduction

Recycled aluminium constitutes a steadily growing fraction of the global aluminium supply. In addition to avoiding disposing of scrap metal, an important reason for using recycled aluminium is the reduced production energy. In total, producing recycled aluminium has an energy cost of only a few percent of that of producing it from bauxite [1]. The main disadvantage of recycled material is the accidental introduction of trace elements, which can be both detrimental and beneficial for the properties of alloys.

The subject of this study is the age-hardenable 6*xxx* aluminium alloy series, where the main alloying elements are magnesium and silicon. 6*xxx* alloys constitute the largest share of produced aluminium alloys, and are heavily used for both architectural and automotive purposes [1]. Upon appropriate heat treatment, Mg and Si atoms cluster to form nano-sized metastable precipitates. These prevent the motion of dislocations when the material is under stress, and thus increase the strength of the material. The precipitates form in a sequence, starting with phases which are coherent with the Al matrix and ending in large, incoherent phases with the lowest bulk formation enthalpy. The precipitation sequence for the Al–Mg–Si system is [2–4]

$$SSSS \rightarrow Clusters \rightarrow GP-zones \rightarrow \beta'' \rightarrow \beta', U1, U2, B' \rightarrow \beta, Si. \quad (1)$$
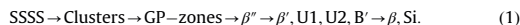
The metastable and fully coherent β'' is the main hardening phase. Like all the metastable phases, it is needle-shaped and has its main growth direction along $\langle 001 \rangle_{Al}$.

Calcium is a common impurity element in aluminium as it can be introduced at many steps during the production [5]. In Al–Mg–Si alloys, it is known to be detrimental to their mechanical strength [1,5], making control of the Ca content important both during primary production and recycling of alloys. A decrease in strength with Ca content signifies a change in precipitate microstructure, which is worth investigating due to the industrial relevance of Ca additions. Calcium is located underneath magnesium in the alkaline earth metal group in the periodic table of elements, which gives reason to believe that Ca atoms can replace Mg atoms in precipitate structures characteristic of the Al–Mg–Si system. By analogy, the replacement of Si by Ge was previously investigated. Al–Mg–Ge alloys contain precipitate types related to those in Al–Mg–Si, and small additions of Ge to Al–Mg–Si alloys have been found to promote nucleation [6].

In this paper we present a study of the microstructure in Al–Mg–Si alloys with different Ca content, from trace amounts to typical alloying amounts, and explain why Ca additions reduce the mechanical strength of this class of alloys. The main characterization technique was electron microscopy in its transmission and scanning variants (TEM and SEM). Details regarding the experimental procedures are given in the next section. Results of hardness measurements, microscopy and spectroscopy are found in Section 3 and discussed in Section 4, while Section 5 serves as a conclusion.

2. Experimental

The alloys chosen for this study are a subset of alloy compositions created for the investigation of trace element influences on

---

Table 1
Compositions of the samples (at%), measured by ICP-OES. Balance is Al.

Alloy	Mg	Si	Fe	Ca
LCa1	0.53	0.40	0.034	0.0019
LCa2	0.52	0.40	0.033	0.0060
LCa3	0.53	0.39	0.033	0.0727

precipitation. Having a total solute concentration of ≈ 1 at%, the base alloy is low-solute (lean) by industrial standards for 6xxx alloys. Its commercial counterpart is 6060, which has comparable Mg and Si content. The exact compositions of the three Ca-containing alloys were measured by inductively coupled plasma optical emission spectroscopy (ICP-OES), and are given in Table 1.

The material was extruded as cylindrical rods of cross-sectional diameter 20 mm. Solution heat treatment at 540 °C was carried out for 1 h, followed by quenching in room-tempered water. The rods were cut into 10 mm long samples and stored at room temperature for 4 h in total. Subsequently, the samples were heated at a rate of 200 °C/h to an artificial aging temperature of 185 °C and kept in the furnace for variable times (max. 24 h) before being quenched in water. Vickers hardness was measured for each aging time using a Struers DuraScan-70. The average hardness values were calculated based on 10 indentations with 5 kg force.

Slices were cut from the samples and polished down to a thickness of ≈ 100 μm. Discs from these slices with a diameter of 3 mm were further electropolished to TEM specimens with a Struers TenuPol-5, using a solution of 1/3 nitric acid and 2/3 methanol. The applied voltage was 20 V at a temperature of −25 °C. Bright-field TEM images of the precipitate microstructure were acquired using a LaB_6 Philips CM30 operated at 150 kV. A post-column Gatan parallel electron energy loss spectroscopy (EELS) system was used to estimate the thickness of the specimen at the points where images were taken. The specimens were imaged in the $\langle 001 \rangle_{Al}$ direction to enable measurement of precipitate length and cross-sectional area. The counting and measuring was conducted using an in-house algorithm. See [7] for details regarding the quantification procedure. Elemental analysis was conducted using an Oxford INCA energy-dispersive X-ray spectroscope (EDS) on a Jeol JEM-2010F field emission gun microscope operated at 200 kV.

The hardness measurement samples were also prepared for SEM imaging. They were polished to a roughness of 1 μm and further electropolished using a Struers Polectrol with the "A2" electrolyte (70% ethanol, 10% 2-butoxyethanol, 8% perchloric acid, 12% distilled water). The voltage was set to 30 V and the polishing time to merely 1 s to prevent too much preferential etching of the Al matrix. A Jeol JSM-840 with a tungsten filament was used for imaging. In a SEM, the intensity of backscattered electrons is dependent on the average atomic number per volume (Z-contrast). We therefore used a backscattered electron detector to detect Ca-containing particles and separate them from Fe-containing particles. In addition, EDS analysis was conducted using a Hitachi TM3000 tabletop SEM. X-ray diffraction (XRD) was done on SEM samples using a Siemens D5005 instrument.

3. Results

3.1. Hardness evolution and microstructure

The hardness evolution during artificial aging of the three alloys (Fig. 1) gives a rough overview of the precipitation kinetics. The overall shapes of the curves are conserved when Ca is added,
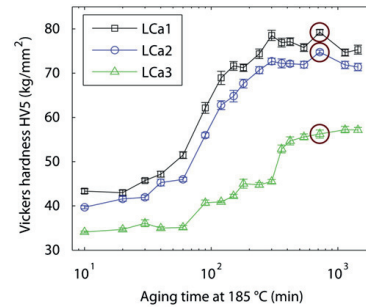

Fig. 1. Vickers hardness of samples with compositions shown in Table 1 during artificial aging at 185 °C. The conditions selected for TEM analysis are marked with circles, and correspond to 12 h aging.

but even small amounts (0.0060%=60 ppm) of Ca cause a measurable decrease in peak hardness. It is interesting to note that Ca also decreases the hardness in samples which have only been stored for 4 h at RT (no aging).

We selected the samples aged for 12 h for TEM analysis as these are roughly peak aged. Fig. 2 shows an overview of the precipitate microstructure in this condition for each of the alloys.

We take note of the following:

- The base alloy (LCa1) contains a homogenous microstructure of mostly β'' precipitates.
- The microstructure in LCa3 is dominated by β' and B′ precipitates, which is the characteristic of overaged materials. When compared to LCa1, there are fewer precipitates, which on average are longer and have larger cross-sections. Some inhomogeneity exists: certain areas have higher precipitate number densities and a larger fraction of small β'' precipitates (see Fig. 3(a) for an example).
- LCa2 and LCa3 contain elongated, μm−sized particles (referred to in the further as Ca-containing particles). These always appear thick although in a thin area of the TEM samples, and were thus less etched by the electropolishing than the Al matrix. An example particle is shown in Fig. 3(b).
- The reduced number density of precipitates in LCa2, which has only 60 ppm of Ca, can already be visually distinguished from that of LCa1 in Fig. 2.

The Ca-containing particles are too large and form with a too low number density to be suitable for TEM investigations, apart from EDS analysis. SEM imaging and composition determination of the particles are presented in Section 3.2.

Based on bright-field TEM images as those in Fig. 2, the average precipitate morphology and number density were measured for the three alloys, and are shown in Table 2. As observed in Fig. 2, the addition of 0.07 at% Ca has drastic effects, reducing the number density of precipitates by a factor of 8 and increasing their average volume by a factor of 6, resulting also in a smaller volume fraction.

3.2. Ca-containing particles

The large, elongated particles found in the LCa3-12 h condition by TEM were probed with EDS, and were found to contain Ca. Rounded iron-containing dispersoids of similar sizes were also found in all three alloys. EDS measurements of five particles gave the following quantified atomic fractions: (41.63 ± 0.19)% Al, (39.80 ± 0.48)% Si and (18.57 ± 0.31)% Ca. An estimated thickness
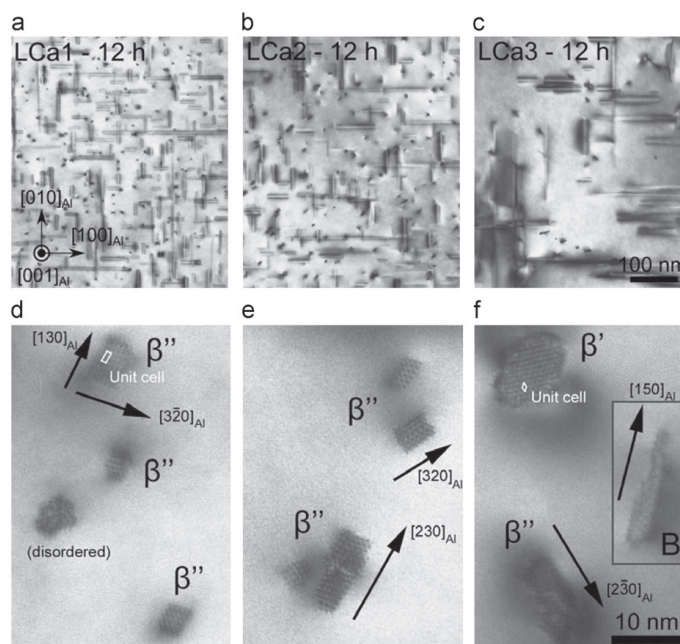
Fig. 2. Bright-field TEM images of the microstructure in the three studied alloys, aged for 12 h at 185 °C. The viewing directions are along ⟨001⟩$_{Al}$, and the thickness of the specimens are in the range 90–150 nm. Images (d–f) show typical precipitate types in the three alloys. (a) LCa1, (b) LCa2, (c) LCa3, (d) LCa1 high mag., (e) LCa2 high mag., and (f) LCa3 high mag.
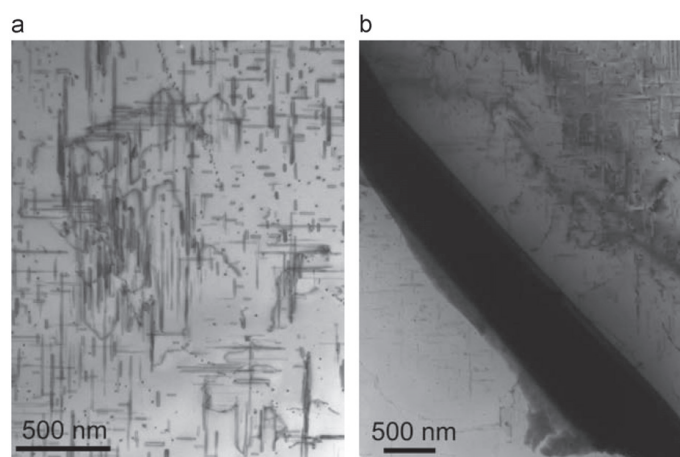

Fig. 3. Low-magnification bright-field TEM images of the LCa3-12 h condition, both oriented in a direction close to ⟨001⟩$_{Al}$. (a) Inhomogeneity: the top right and lower left corners have a fine, β''–dominated microstructure, while we otherwise see a coarser mixture of β'', β' and B′. (b) A Ca-containing particle embedded in the Al matrix. Note the precipitate-free zone on the right side of the particle.

of 100 nm and the same density as pure Al were used in the quantification.

Attempts to unambiguously identify the phase of the particles have failed for the following reasons: not being etched by the electrolyte, the particles were too thick for electron diffraction studies. An attempt was made to prepare a TEM sample using cold stage ion milling, but this removed or destroyed the Ca-containing particles while leaving Fe-containing phases intact. X-ray diffraction (XRD) of SEM samples was also attempted, with diffraction angles from $2\theta = 5°$ to $120°$ and a run time of 21 h. The XRD spectrum showed Al and AlFe/Al$_3$Fe phases, but no signs of any phase containing Ca. With such a small volume fraction and

possibilities for unknown orientation relationships with the Al matrix, the particles are apparently very difficult to detect by XRD.

By comparing the size and distribution of Ca-containing particles in LCa3-12 h and LCa3-RT (no aging) in the SEM, we found that the particles did not change during artificial aging, and must have been fully developed during earlier high-temperature treatments associated with casting, homogenization, extrusion and solution heat treatment. Fig. 4 displays the surface of the LCa3-10 min sample as viewed with backscattered electrons in a SEM. EDS maps were also obtained, showing the distribution of relevant elements close to the sample surface. The Ca-containing particles are plate-shaped, with a thickness of roughly 0.4 μm and typical extent of 10 μm. SEM images taken parallel to the extrusion direction enabled the measurement of the area fraction of the particles, which should be equal to their volume fraction. Measuring on images encompassing 422 particles, we found a volume fraction of $(0.29 \pm 0.03)\%$ (statistical error) in LCa3-10 min. A SEM sample with the extrusion direction perpendicular to the surface normal was also made. As shown in Fig. 5, the Ca-containing particles were found to be inhomogenously distributed and oriented along the extrusion direction.

3.3. Presence of Ca elsewhere

In addition to using EDS measurements in a TEM to probe the large particles in the LCa3-12 h sample, we also checked its hardening precipitates for traces of Ca. Three β'' and one B' were analyzed and did not contain measurable levels. See Fig. 6 for examples of EDS spectra from the precipitates, compared to a spectrum from a Ca-containing particle such as the one depicted in

Fig. 3(b). We also conducted an analytical scanning TEM (STEM) measurement with an EDS acquisition time of about 4 h. Fig. 7 shows the annular dark field (ADF) STEM image and elemental EDS maps. The image contains a low-angle grain boundary (GB) with GB precipitates, and hardening precipitates in two grains which are close to a $\langle 001 \rangle_{Al}$ orientation. No segregation of Ca at the grain boundary or in the hardening precipitates is visible. The concentration of Ca estimated from the EDS map is 0.05 at% in the whole image, which is around 70% of the total Ca concentration in the material. The precipitates on the grain boundary are most likely Mg–Si phases which have been etched by the electrolyte during sample preparation and are now oxidized and Mg-poor.

4. Discussion

Fig. 1 reveals that even 60 at ppm Ca (LCa2) has a measurable negative influence on the hardness. Previous investigations [5] show no effect on yield strength in a similar alloy when 59 at ppm

Table 2
Characterization of precipitate microstructure in the three alloys. The errors are all statistical except the error in specimen thickness, which is estimated to 10%.

Condition	Cross-section (nm^2)	Length (nm)	Number density (10^3 μm^{-3})	Volume fraction (%)
LCa1-12 h	17.32 ± 0.55	41.1 ± 1.8	11.5 ± 1.2	0.82 ± 0.10
LCa2-12 h	22.68 ± 0.86	58.5 ± 2.8	6.38 ± 0.68	0.85 ± 0.10
LCa3-12 h	35.8 ± 2.5	115 ± 12	1.48 ± 0.18	0.61 ± 0.11
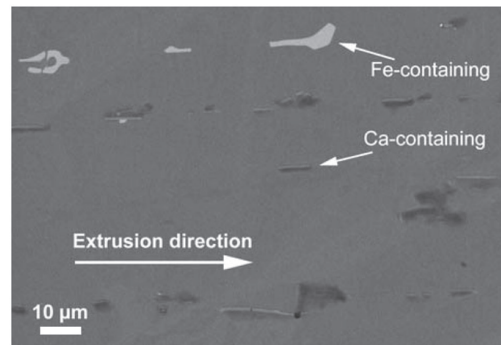
Fig. 5. Backscattered electron image of a sample with its surface normal perpendicular to the extrusion direction (condition LCa3-20 min). The acceleration voltage was 10 kV. The Ca-containing particles are inhomogenously distributed in the Al matrix and were deformed during the extrusion of the material.
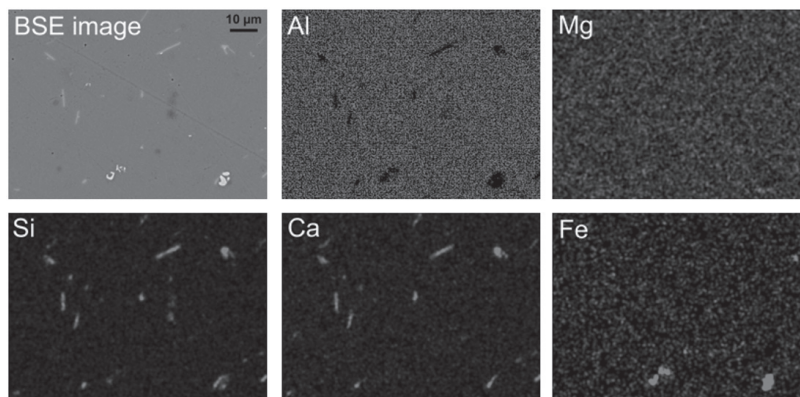

Fig. 4. A backscattered electron SEM image of condition LCa3-10 min, with corresponding elemental EDS maps. The acceleration voltage was 15 kV. The viewing direction is parallel with the extrusion direction. Ca- (and Si-) containing plate-shaped particles are easily distinguished from iron-containing constituent particles and dispersoids based on shape and backscattered electron contrast.

97

S. Wenner et al. / Materials Science & Engineering A 575 (2013) 241–247

245

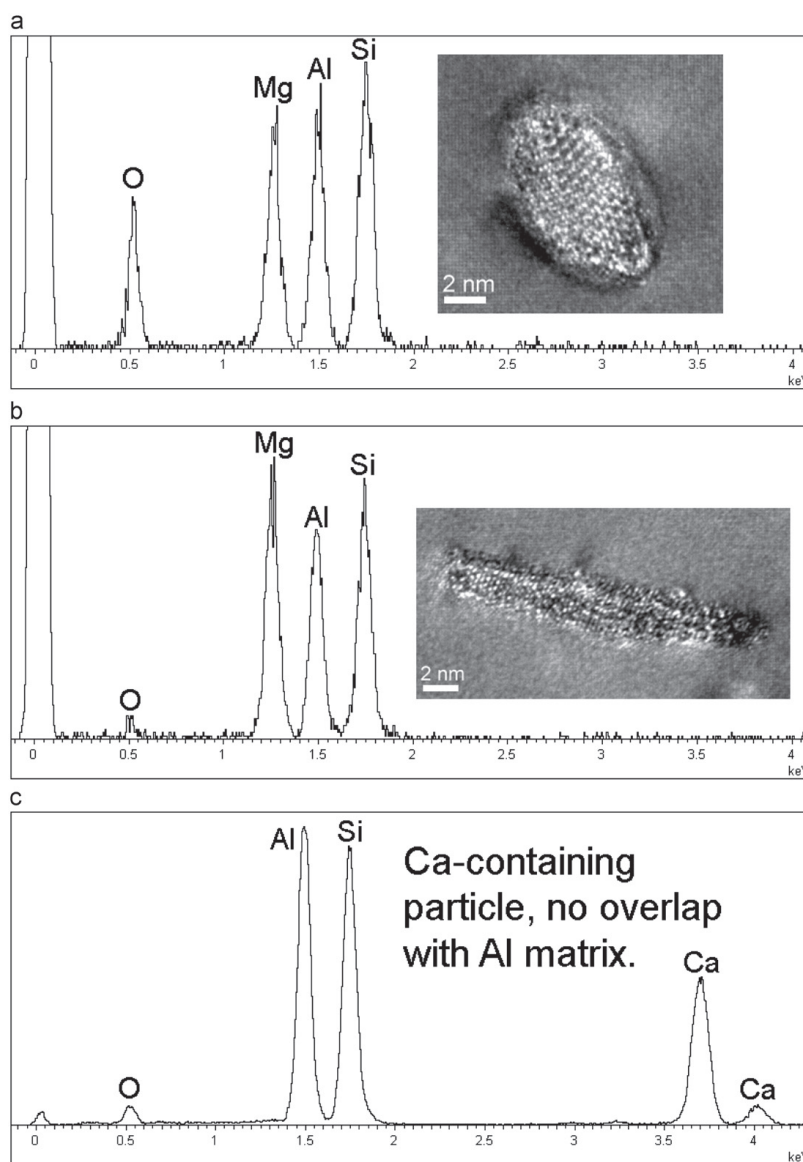**Fig. 6.** EDS spectra acquired by TEM, with the electron beam focused on two hardening precipitates (respective images included) and one Ca-containing particle. (a) A partially disordered β''. (b) A partially disordered B'. (c) A Ca-containing particle.

Ca is added, suggesting that concentrations below these values have little influence in practical applications. It is clear from the precipitate quantification found in Table 2 that the hardness decrease with Ca additions is caused by a coarsening of the precipitate microstructure along with a change in precipitate types and a slight volume fraction decrease. The microstructure observed in LCa3-12 h contains more precipitates that are associated with overaging than that of LCa1-12 h, judging from the

precipitation sequence in Eq. (1). The low hardness of LCa3 is produced by a mixture of β'' precipitates (also found in LCa1 and LCa2) with β' and B' precipitates. Previous studies [8,9] have shown that coarsening and apparent overaging can be a consequence of a reduced solute content and/or an increased Mg/Si ratio in the alloy.

The Si content available in the solid solution must be reduced through the formation of Ca-containing particles. EDS measurements
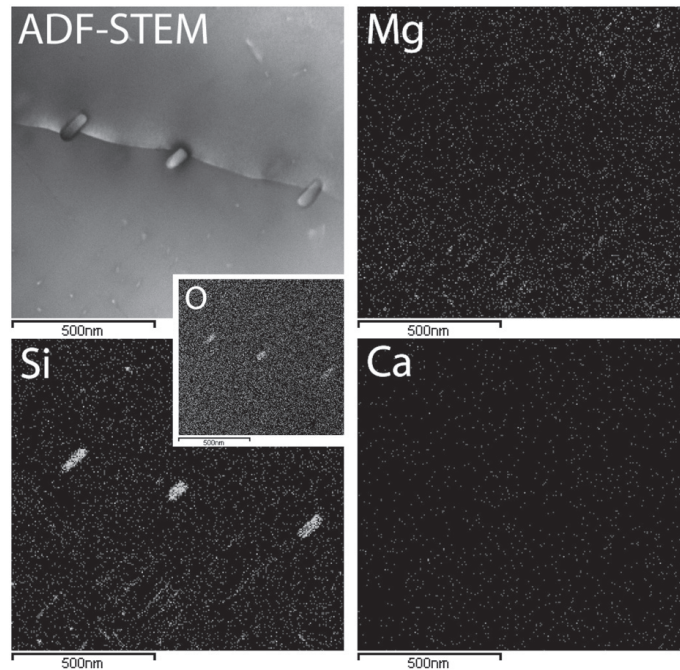
98

S. Wenner et al. / Materials Science & Engineering A 575 (2013) 241–247

Fig. 7. An annular dark-field scanning transmission electron microscopy image (ADF-STEM) and associated elemental energy-dispersive X-ray spectroscopy (EDS) maps, showing the concentration of the different elements around a grain boundary. Hardening precipitates are visible as needles along $\langle 001 \rangle_{Al}$ directions in the upper and lower parts of the Mg and Si maps. No segregation of Ca is visible.

on the particles gave the approximate ratios Ca:Al:Si = 1:2:2. This fits with the stable phase $CaAl_2Si_2$, which has a hexagonal structure with lattice parameters $a = 0.413$ nm, $c = 0.7145$ nm, and space group $P\bar{3}m1$ [10,11]. As pointed out in [12], the phase is isostructural to the overaged U1–$MgAl_2Si_2$ phase in the Al–Mg–Si alloy system, with Mg replaced by Ca. This replacement expands the unit cell by 3.3 vol%, which might make the phase incoherent with the Al lattice. In any case, the phase is seen grown as large particles, unaffected by typical aging temperatures, and is therefore probably stable outside the Al matrix. It is unlikely that the particles have any hardening potential in Al. As explained in Section 3.2, we did not succeed in obtaining diffraction data (electron or X-ray) from the phase, and cannot confirm the U1–Ca structure. From the compositional measurements, this is still the most probable structure candidate for the observed phase. An inhomogenous distribution of particles with composition $CaAl_2Si_2$ have also been found in Al–Si foundry alloys with 185 at ppm Ca additions [13].

Fig. 5 shows that the process of extrusion aligns the particles parallel to the extrusion direction. From SEM quantification, the volume fraction of the particles was estimated to 0.29% in the LCa3 samples. Using the number of Ca atoms per volume in the U1–Ca structure, we find that 61% of the Ca is inside the large particles. This leaves 0.03 at% Ca in solid solution, which seems reasonable given the EDS measurement of 0.05 at% in the small area of Fig. 7. The U1-Ca particles also need 23% of the Si in the alloy, which increases the solid solution Mg/Si (atomic) ratio from 1.35 to 1.75. Al–Fe–Si phases (seen in Fig. 4) also require some Si to form, lowering the effective Si content even further. By comparison, the Mg/Si ratio has been measured to 1.1 in β'' [14] (atom-probe tomography) and to 1.68 [15], 1.39 [16] and 1.69 [17] in β' (all with

EDS). With an increasing solid solution Mg/Si ratio as a function of Ca content, we can explain why the precipitate types change as Ca is added. The explanation also makes the reason for the inhomogeneity in the microstructure of LCa3 [see Fig. 3(a)] apparent. Far from a Ca-containing particle, more Si is available in solid solution, and an island of fine microstructure can appear during aging. The amount of Si in the bulk could not be directly measured using EDS due to local accumulations (possibly of silicon oxide on the TEM specimen surface).

5. Conclusions

We have measured the hardness evolution during artificial aging of a base Al–Mg–Si alloy with 0.0019, 0.0060 and 0.0727 at% Ca additions and studied the materials using TEM and SEM. After 12 h aging at 185 °C, the peak Vickers hardness of the alloys were 79, 75 and 56, respectively. The hardness decrease with the addition of small quantities of Ca stresses the importance of impurity removal during production of Al alloys. From a fine, homogenous microstructure of β'' needles, Ca additions cause a change to larger, less coherent β' and B' precipitates, lowering the mechanical strength. The change in microstructure is caused by a deficiency of Si. During casting, micrometer-sized particles with composition $CaAl_2Si_2$ form and absorb nearby Si, leading to larger and less coherent precipitates and a more inhomogenous microstructure. The large particles themselves are incoherent and have no hardening potential. Ca was not found to accumulate in hardening precipitates or along grain boundaries, but stays in solid solution if not included in the large particles.

Acknowledgments

References

[1] J.R. Davis (Ed.), Aluminum and Aluminum Alloys, ASM Specialty Handbook, ASM International, 1993.

[2] G.A. Edwards, K. Stiller, G.L. Dunlop, M.J. Couper, Mater. Sci. Forum 217–222 (1996) 713–718.

[3] K. Matsuda, Y. Sakaguchi, Y. Miyata, Y. Uetani, T. Sato, A. Kamio, S. Ikeno, J. Mater. Sci. 35 (2000) 179–189.

[4] S.J. Andersen, C.D. Marioara, A. Frøseth, R. Vissers, H.W. Zandbergen, Mater. Sci. Eng. A 390 (2005) 127–138.

[5] T. Furu, N. Telioui, C. Behrens, J. Hasenclever, P. Schaffer, Trace elements in aluminium alloys: their origin and impact on processability and product properties, in: 12th International Conference on Aluminum Alloys, The Japan Institute of Light Metals, 2010.

[6] R. Bjørge, C.D. Marioara, S.J. Andersen, R. Holmestad, Metall. Mater. Trans. A 41 (2010) 1907–1916.

[7] C. Marioara, H. Nordmark, S. Andersen, R. Holmestad, J. Mater. Sci. 41 (2006) 471–478, http://dx.doi.org/10.1007/s10853-005-2470-1.

[8] C.D. Marioara, S.J. Andersen, H. Zandbergen, R. Holmestad, Metall. Mater. Trans. A 36 (2005) 691–702, http://dx.doi.org/10.1007/s11661-005-0185-1.

[9] S. Wenner, C.D. Marioara, S.J. Andersen, R. Holmestad, Int. J. Mater. Res. 103 (2012) 948–954.

[10] E. Gladyshevskii, P. Kripyakevich, O. Bodak, Ukr. Fiz. Zh. 12 (1967) 447–453.

[11] Materials Science International Team, R. Schmid-Fetzer, Light Metal Systems. Part 1, Landolt-Börnstein—Group IV Physical Chemistry, vol. 11A1, Springer-Verlag, pp. 150–158.

[12] S. Andersen, C. Marioara, R. Vissers, A. Frøseth, H. Zandbergen, Mater. Sci. Eng. A 444 (2007) 157–169.

[13] T. Ludwig, P.L. Schaffer, L. Arnberg, Metal. Trans. A, submitted for publication, http://dx.doi.org/10.1007/s11661-013-1694-y.

[14] H.S. Hasting, A.G. Frøseth, S.J. Andersen, R. Vissers, J.C. Walmsley, C.D. Marioara, F. Danoix, W. Lefebvre, R. Holmestad, J. Appl. Phys. 106 (2009) 123527.

[15] K. Matsuda, S. Tada, S. Ikeno, in: T.H. Sanders, E.A. Starke (Eds.), Proceedings of the 4th International Conference on Aluminum Alloys, Georgia Institute of Technology, 1994, p. 605.

[16] C. Cayron, P.A. Buffat, Acta Mater. 48 (2000) 2639–2653.

[17] R. Vissers, M.A. van Huis, J. Jansen, H.W. Zandbergen, C.D. Marioara, S.J. Andersen, Acta Mater. 55 (2007) 3815–3823.

Aberration-corrected STEM–EELS studies of precipitates in an Al–Mg–Si–Cu–Ag alloy

S. Wenner, C. D. Marioara, Q. M. Ramasse,
D.-M. Kepaptsoglou, F. S. Hage and R. Holmestad

Paper 5

Atomic-resolution electron energy loss studies of precipitates in an Al–Mg–Si–Cu–Ag alloy

Sigurd Wenner,[a,*] Calin D. Marioara,[b] Quentin M. Ramasse,[c]
Despoina-Maria Kepaptsoglou,[c] Fredrik S. Hage[c] and Randi Holmestad[a]

[a]Department of Physics, NTNU, Høgskoleringen 5, Trondheim NO-7491, Norway
[b]Materials and Chemistry, SINTEF, Høgskoleringen 5, Trondheim NO-7491, Norway
[c]SuperSTEM Laboratory, STFC Daresbury Campus, Keckwick Lane, Daresbury WA4 4AD, UK

Aberration-corrected scanning transmission electron microscopy combined with electron energy loss spectroscopy has been used to determine the distribution of Cu and Ag atomic columns of precipitates in an Al–Mg–Si–Cu–Ag alloy. Cu columns were commonly part of C and Q′ phases, with the atomic columns having large projected separations. Columns containing Ag were more tightly spaced, in areas lacking repeating unit cells and at incoherent precipitate–host lattice interfaces. Cu-rich and Ag-rich areas were not found to intermix.
© 2013 Acta Materialia Inc. Published by Elsevier Ltd. All rights reserved.

Keywords: Aluminum alloys; Precipitation; Scanning transmission electron microscopy; Electron energy loss spectroscopy

Al–Mg–Si alloys are heat-treatable and exhibit a significant increase in strength upon nucleation and growth of hardening nanosized metastable phases. Detailed investigations of the precipitation sequence have been performed over the years, and the crystal structures of most metastable phases have been solved by means of quantitative transmission electron microscopy (TEM) combined with first-principles calculations [1,2]. When Cu is added to the alloys, the precipitation phases of the Al–Mg–Si system are suppressed [3], and new, Cu-containing phases such as C [4] and Q′ [5–7] form. Additionally, areas with no repeating unit cell become more common in the structure of the precipitates. One characteristic of all metastable precipitates in the Al–Mg–Si(–Cu) system is that they have one main coherency (and growth) direction, along $\langle 0\,0\,1\rangle_{Al}$. Consequently, they all are needle-, lath- or plate-shaped. Moreover, they contain a common network of Si columns along their main growth direction, with a projected near-hexagonal structure [8]. Atomic columns of Mg, Al and Cu occupy positions between these Si columns, all three having different preferred local atomic configurations and site symmetries. Small additions of

Cu to Al–Mg–Si alloys have been found to increase the mechanical strength [3], and additions of Ag have a similar effect [9]. The reason for this is that Cu and Ag promote precipitate nucleation, and create a microstructure of smaller precipitates with higher number density. Recent work has shown that Ag enters the (Cu-free) β' precipitate and replaces 1/3 of its Si atomic columns, creating its own local symmetries [10]. In this paper we reveal the different roles played by Cu and Ag atoms in metastable precipitates in Al–Mg–Si–Cu–Ag alloys.

High-angle annular dark-field scanning TEM (HAADF–STEM) has proven to be a very useful technique for investigating the structure of precipitates in Al alloys. This is due to the properties of high-angle scattered electrons: they are incoherent and form an easily interpretable image, as the contrast is generally unaffected by small changes in objective lens defocus and specimen thickness [11–13]. In addition, the scattered intensity (Rutherford and thermal diffuse scattering) from an atomic column increases with its atomic number Z. The development of C_s aberration correctors [14,15] has improved the technique by achieving spatial resolutions below 0.1 nm. These attributes make the identification of pure Cu ($Z = 29$) and Ag ($Z = 47$) atomic columns straightforward, and even enable the

* Corresponding author. Tel.: +47 93820647; fax: +47 73597710;
  e-mail: sigurd.wenner@ntnu.no

Table 1. Nominal composition of the studied alloy (at.%).

Mg	Si	Mn	Fe	Cu	Ag	Al
1.00	0.62	0.27	0.10	0.14	0.03	Balance

Si ($Z = 14$) columns to be distinguished from Al ($Z = 13$) and Mg ($Z = 12$) columns [10]. However, the technique has certain limitations: elements close in Z (such as Al and Mg), mixed atomic columns and columns with partial occupancies make it difficult to form atomic models of entire precipitates. On the other hand, electron energy loss spectroscopy (EELS) does not suffer from these limitations. This TEM technique is commonly used to extract compositional information and properties of the electronic structure from nanosized regions in materials. The combination of EELS and aberration-corrected STEM has been successfully used for atomic-resolution elemental mapping and electronic fine structure studies in, for example, metal oxides [16,17]. There have been few attempts to copy this success for the case of Al alloys. Al and its neighbours in the periodic table are not particularly suitable for EELS analysis because their L-edges overlap with the Al plasmon peaks, and their K-edges are of high energy and will thus give poor statistics. However, recent advances such as dual energy range EELS [18] make the Al–K, Mg–K and Si–K edges more available for analysis.

In this work metastable precipitates formed in an Al–Mg–Si–Cu–Ag alloy have been imaged by probe C_s-corrected HAADF–STEM and the distribution of Ag and Cu atomic columns has been analyzed by atomic-resolution EELS elemental mapping. These two elements were chosen since their edges Ag–$M_{4,5}$ at 367 eV and Cu–$L_{2,3}$ at 931 eV, combined with their high HAADF–STEM Z contrast, make them suitable for detailed analysis. This model system is thus used to emphasize the advantages of atomic-resolution EELS for precipitate structure determination.

The composition of the extruded profiles used in the study is given in Table 1. The elements Mn and Fe were added to form dispersoid particles that reduce the grain size of the material, and do not participate in precipitation of hardening phases. To achieve an over-aged microstructure composed of finely dispersed Cu-containing precipitates, the following heat treatment was applied: 30 min of solution heat treatment at 530 °C, quenching in water and storage for 4 h at room temperature, aging to peak hardness with 12 h of annealing at 155 °C and lastly over-aging for 21 days at 200 °C. The TEM specimen was prepared by mechanical polishing, dimpling and ion milling with energies from 4.0 keV down to 1.5 keV. To prevent carbon contamination, the specimen was baked in vacuum at approx. 135 °C for 6 h before loading in the microscope, and was given regular electron beam showers during microscopy. Tests were performed to ensure that the baking procedure does not alter the microstructure significantly.

HAADF–STEM and EELS spectrum imaging were performed using an aberration-corrected Nion UltraSTEM™ 100 at the SuperSTEM facility at Daresbury, UK. Its cold field emission gun electron source gives a native energy resolution of 0.35 eV, and the minimum expected probe size is 0.08 nm. A voltage of 100 kV was applied. The beam convergence angle was 30 mrad, the HAADF–STEM detector angles were 74–185 mrad

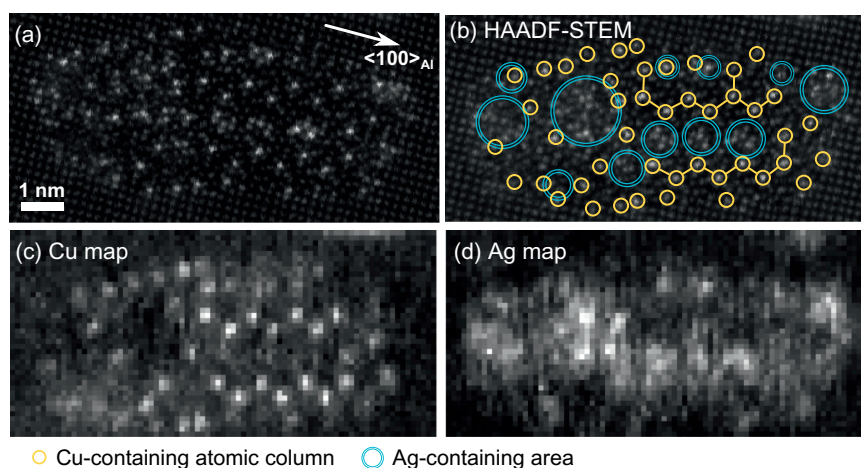○ Cu-containing atomic column   ○ Ag-containing area

Figure 1. (a and b) Raw HAADF–STEM images of a precipitate cross-section, taken respectively before and during the STEM–EELS acquisition. (c and d) EELS elemental maps of Cu and Ag. The location of Cu atomic columns and areas rich in Ag are marked in (b). Cu columns in a Q′ configuration are connected by lines.
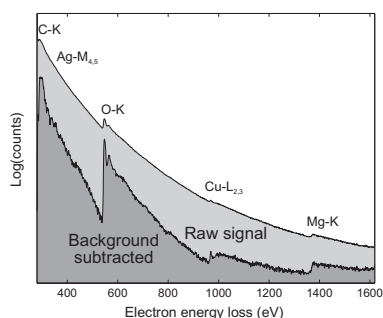
Figure 2. Accumulated EEL spectrum of the area in Figure 1, in the energy loss range 280–1620 eV. Note the logarithmic intensity axis. The lower curve is background subtracted (global power-law background) and scaled up for easier identification of the edges. The Ag–$M_{4,5}$ edge is still difficult to observe as it is blocked out by the C–K fine structure.

and the EELS collection angle was 31 mrad. A dispersion of 1.0 eV/channel was always used.

EEL spectra were acquired in the energy loss range 280–1620 eV. This includes the edges Ag–$M_{4,5}$ at 367 eV, Cu–$L_{2,3}$ at 931 eV and Mg–K at 1305 eV, but does not make any Al or Si edges available. The spectra were improved by means of principal-component analysis (PCA) using the software Hyperspy (previously EEL-SLab [19]). Consequently, the spectrum images were improved to the point that some atomic columns of Ag could be resolved, despite a very noisy starting point. The elemental maps were created in Gatan DigitalMicrograph by manual integration of EELS edges after power-law background subtraction.

The investigated specimen had a high number density of hardening precipitates, most of them plate-/lath-shaped. Two examples of such precipitates are given in Figures 1 and 3. All observed particles contained both Cu and Ag, and had some regions with no repeating unit cells, although structural units of the Q′ and C phases (marked with connected lines on Figs. 1b and 3b) were a common occurrence. The summed EEL spectrum from the full area of Figure 1 is shown in Figure 2. For both precipitates, clear Cu–L and Mg–K edges could be seen in the spectra, while the low total content of Ag makes the Ag–M edge barely visible. Due to the small probe size and the long acquisition time required for EELS, beam damage was observed in some datasets. The HAADF–STEM images from the two sets chosen for the present analysis revealed little to no damage.

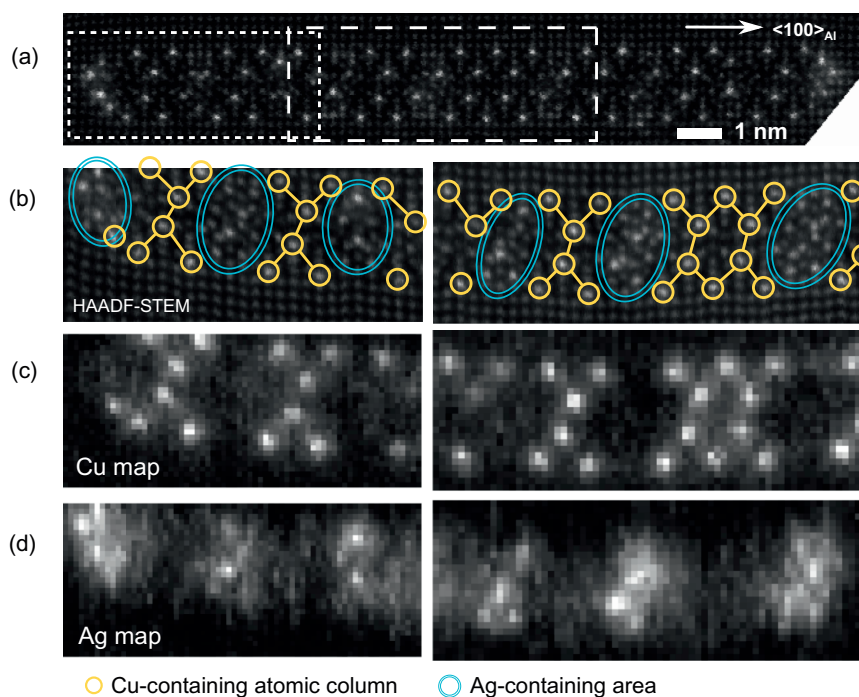**Figure 3.** (a and b) Raw HAADF–STEM images of a precipitate cross-section, taken respectively before and during the STEM–EELS acquisition. (c and d) EELS elemental maps of Cu and Ag from the two acquisition areas marked in (a). The skew in the images is caused by specimen drift. The location of Cu atomic columns and areas rich in Ag are marked in (b). Cu columns in a C configuration are connected by lines.

4   *S. Wenner et al. / Scripta Materialia xxx (2013) xxx–xxx*

There is a very good correspondence between bright spots in the HAADF–STEM images and those in the Cu maps, for both precipitates. This enabled identification of most Cu atomic columns. The precipitate in Figure 1 has two areas where Cu columns form a Q′ configuration, shown with connected lines. Most of the other Cu columns are located along coherent precipitate interfaces and are not related to any periodic structure. All Cu columns in Figure 3 form a C phase configuration, making the two figures representative of two types of precipitates observed in the specimen.

As opposed to the Cu maps, the Ag maps indicate a broader distribution, over many neighboring atomic columns and in compact areas, for both precipitates. Delocalization of M edges is a known issue [20], which can give an apparent intensity spread to neighboring columns. We see, however, certain clearly resolved Ag-containing columns quite close to each other in Figure 3d, with corresponding bright spots in the HAADF–STEM images (Fig. 3b). A variable Z contrast, and one merely comparable to that of Cu, indicates that Ag is mixed with other, lighter elements in its atomic columns. It is interesting that Ag-rich areas do not overlap with Cu atomic columns, with some exceptions in Figure 1. The different preferred configurations of neighboring atoms might explain the lack of mixed Ag/Cu columns in these precipitates. Ag seems to be interrupted the formation of ordered Al–Mg–Si–Cu precipitates, and instead creating Ag-rich areas with no repeating unit cells. Accumulations of Ag were commonly observed at incoherent precipitate–host lattice interfaces, e.g. the ends of the precipitate in Figure 3.

Although the Mg–K edge can be clearly seen in the EEL spectrum, the large pixel sizes used in the acquisitions and the short projected distance between Mg columns made it infeasible to distinguish individual Mg columns. The low Z contrast also made the distinction between the Mg and Al columns in HAADF–STEM images impossible. Due to these considerations, Mg elemental maps are not shown in this paper.

HAADF–STEM imaging combined with STEM–EELS mapping was used to investigate the distribution of Cu and Ag atomic columns in precipitates formed in an Al–Mg–Si–Cu–Ag alloy. Cu was found clearly localized in certain atomic columns, while Ag was spread with various occupancies in neighboring atomic columns. Most observed precipitates had regions consisting of structural units from the Q′ or C phases, of which shown two examples are shown here. Ag was seen to disrupt the formation of these ordered phases, and localize in Cu-free areas lacking repeating unit cells, which indicates that Ag forms its own local configurations inside the precipitates. While Cu was observed preferentially along coherent interfaces with the Al host lattice, Ag was localized at the narrow ends of precipitates, which have lower coherency with, and induce higher strain in, the host lattice. With the new possibilities of obtaining atomic-resolution compositional information from precipitate phases, the STEM–EELS technique will become an important tool for future Al alloy design.

[1] H.W. Zandbergen, S.J. Andersen, J. Jansen, Science 277 (1997) 1221–1225, http://dx.doi.org/10.1126/science.277.5330.1221.
[2] J.H. Chen, E. Costan, M.A. van Huis, Q. Xu, H.W. Zandbergen, Science 312 (2006) 416–419, http://dx.doi.org/10.1126/science.1124199.
[3] C.D. Marioara, S.J. Andersen, T.N. Stene, H. Hasting, J. Walmsley, A.T.J. Van Helvoort, R. Holmestad, Phil. Mag. 87 (2007) 3385–3413, http://dx.doi.org/10.1080/14786430701287377.
[4] M. Torsæter, F.J.H. Ehlers, C.D. Marioara, S.J. Andersen, R. Holmestad, Phil. Mag. 92 (2012) 3833–3856, http://dx.doi.org/10.1080/14786435.2012.693214.
[5] L. Arnberg, B. Aurivillius, Acta Chem. Scand. 34A (1980) 1–5.
[6] C. Wolverton, Acta Mater. 49 (2001) 3129–3142, http://dx.doi.org/10.1016/S1359-6454(01)00229-4.
[7] C. Ravi, C. Wolverton, Acta Mater. 52 (2004) 4213–4227, http://dx.doi.org/10.1016/j.actamat.2004.05.037.
[8] S. Andersen, C. Marioara, R. Vissers, A. Frøseth, H. Zandbergen, Mater. Sci. Eng. A 444 (2007) 157–169, http://dx.doi.org/10.1016/j.msea.2006.08.084.
[9] J. Kim, C.D. Marioara, R. Holmestad, E. Kobayashi, T. Sato, Mater. Sci. Eng. A 560 (2013) 154–162, http://dx.doi.org/10.1016/j.msea.2012.09.051.
[10] C.D. Marioara, J. Nakamura, K. Matsuda, S.J. Andersen, R. Holmestad, T. Sato, T. Kawabata, S. Ikeno, Phil. Mag. 92 (2012) 1149–1158, http://dx.doi.org/10.1080/14786435.2011.642319.
[11] P.D. Nellist, S.J. PennycookAdvances in Imaging and Electron Physics, vol. 113, Elsevier, 2000, pp. 147–203.
[12] T. Yamazaki, M. Kawasaki, K. Watanabe, I. Hashimoto, M. Shiojiri, Ultramicroscopy 92 (2002) 181–189, http://dx.doi.org/10.1016/S0304-3991(02)00131-6.
[13] H. Rose, Ultramicroscopy 110 (2010) 488–499, http://dx.doi.org/10.1016/j.ultramic.2009.10.003.
[14] P.E. Batson, N. Dellby, O.L. Krivanek, Nature 418 (2002) 617–620, http://dx.doi.org/10.1038/nature00972.
[15] K.W. Urban, C.-L. Jia, L. Houben, M. Lentzen, S.-B. Mi, K. Tillmann, Philos. Trans. Roy. Soc. A 367 (2009) 3735–3753, http://dx.doi.org/10.1098/rsta.2009.0134.
[16] H. Tan, S. Turner, E. Yücelen, J. Verbeeck, G. Van Tendeloo, Phys. Rev. Lett. 107 (2011) 107602, http://dx.doi.org/10.1103/PhysRevLett.107.107602.
[17] I. MacLaren, L.Q. Wang, B. Schaffer, Q.M. Ramasse, A.J. Craven, S.M. Selbach, N.A. Spaldin, S. Miao, K. Kalantari, I.M. Reaney, Adv. Funct. Mater. 23 (2013) 683–689, http://dx.doi.org/10.1002/adfm.201201835.
[18] A. Gubbens, M. Barfels, C. Trevor, R. Twesten, P. Mooney, P. Thomas, N. Menon, B. Kraus, C. Mao, B. McGinn, Ultramicroscopy 110 (2010) 962–970, http://dx.doi.org/10.1016/j.ultramic.2010.01.009.
[19] R. Arenal, F. de la Peña, O. Stéphan, M. Walls, M. Tencé, A. Loiseau, C. Colliex, Ultramicroscopy 109 (2008) 32–38, http://dx.doi.org/10.1016/j.ultramic.2008.07.005.
[20] M.D. Rossell, Q.M. Ramasse, S.D. Findlay, F. Rechberger, R. Erni, M. Niederberger, ACS Nano 6 (2012) 7077–7083, http://dx.doi.org/10.1021/nn3021212.

Part III

Concluding remarks

Chapter 4

Comments to the papers

The five papers included in the previous part present the scientific work done within the Ph.D. project. They all touch upon the subject of precipitation and early phase formation in Al–Mg–Si alloys. The following sections give brief discussions on the main topics to conclude the thesis.

4.1   Natural ageing

After quenching from SHT, Al–Mg–Si alloys display incomprehensibly complex kinetics. The closer one looks at the influence of natural ageing (NA) on microstructure, new stages of kinetics with unexpected effects pop up, which the studies of Banhart *et al.* [43] bear witness to. What happens in all the stages is difficult to figure out with any technique.

Paper 3 gives the hardness curves for four dense alloys. The after-AA hardness with variable NA time (Paper 3, Fig. 2) shows at least three stages of increase/decrease throughout a full year. This is a simple measure, but it captures beautifully some of the complexity of NA. Another study using Mg-Si-balanced alloys with varying total solute content was published by Martinsen *et al.* [44]. The hardness curves show that dense and lean alloys have similar kinetics stages, modified in time scale and rate of hardness increase/decrease. Linking the hardness curve to cluster microstructure is difficult because of the shortcomings of APT, and comparing TEM specimens of after-AA material can not tell the whole story. Changes in precipitate microstructure can definitely be seen when varying the NA time, but we are unable to probe the precipitate nucleation on the two kinds of solute clusters (see section 4.4). Diffusion in the solid state, which drives it all, is in my humble opinion one of the most difficult problems in physics. Numerical modelling through smart multi-scale simulations (maybe DFT coupled with

a kinetic Monte Carlo scheme) may provide the best insight in the matter of clustering and precipitate nucleation once we have the computational resources.

4.2 Trace elements

The central motivation for the Norwegian–Japanese Al–Mg–Si precipitation project was the topic of trace element inclusion during scrap metal recycling. The other Ph.D. candidate on the project, Takeshi Saito, has therefore worked exclusively on the effect of Cu and Zn additions on precipitation. It is vital to have an overview of which elements are good/bad for certain properties of alloys, and set reasonable limits on the maximum tolerance of unwanted elements. The four elements I have came across have the following effects when added to Al–Mg–Si alloys:

- **Copper:** This is a common addition element in commercial alloys. It is known to give a higher hardness at the cost of a higher susceptibility to corrosion. Cu was added to alloys of Mg/Si= 2 and Mg/Si= 0.5 in paper 3. It gave a hardness boost, and more interestingly, reduced the negative effect of NA regardless of the Mg/Si ratio. The reason is not yet clear, but judging from APT results on the same alloys [144], Cu helps create or stabilises Cluster(2), which later transforms into β''. Adding Cu gives some new phases to the alloy system (see section 2.6.5), but it is also present in disordered parts of otherwise pure Al–Mg–Si precipitates, and at their interfaces [145]. The same work found Cu to be incorporated in precipitates to a higher degree after deformation of the material. These precipitates typically nucleate along dislocations, which may act as high diffusivity paths for Cu, leading them into the precipitate structures. Cu columns are found in two configurations: either a triangular configuration with its three nearest neighbours at the same height (most common), or replacing a Si network column (less common) [145].

- **Calcium:** More a nuisance than anything else, Ca can enter the aluminium melt in many ways. A 6060-like composition with additions of Ca was studied in paper 4 to understand why this element degrades the strength of Al–Mg–Si alloys. The base alloy composition is the same as the one used in [145] and [146]. Already during preparation of TEM specimens, we noticed there was something strange in the etched surface of the Ca-added material. It turned out to be giant particles embedded in the matrix. These were later studied with EDS in both

STEM and SEM, and found to have the composition CaAl$_2$Si$_2$. Being included in the formula, Si was depleted from the matrix, which caused a coarser precipitate microstructure. Adding Ca to Si-containing Al alloys is therefore not a good idea, unless it is found to boost another property in materials where strength is not the biggest concern.

- **Zinc:** Recycling results in occasional mixing of alloy systems, such as Al–Zn–Mg ($7xxx$) alloys being mixed into a $6xxx$ alloy melt. The effect of Zn additions was investigated thoroughly in [146]. The hardness and microstructure were very weakly affected, despite Al–Zn–Mg being another system that relies on precipitation hardening for strength. In this system, plate-shaped precipitates form on $\{111\}_{Al}$ planes [7]. No such plates were observed by BF–TEM. Apparently, most of the Mg is stolen by Al–Mg–Si precipitates such as β''. But the densest alloy contained 1 wt.% Zn, and a lot of effort was spent on finding whether Zn accumulates somewhere. EDS mapping in STEM revealed a film of Zn on grain boundaries. This is typically seen in Cu-containing alloys and cause intergranular corrosion, which made us initiate corrosion testing. The alloy with most Zn was indeed found to corrode easily, and to the largest degree when age hardened. Zn may diffuse to grain boundaries during typical AA treatments. Aberration-corrected HAADF–STEM imaging was also conducted on precipitates. Although no great change in microstructure was observed, some Zn entered into precipitates. Single Zn-containing columns were seen in disordered areas, Zn was found in the Al matrix at precipitate interfaces, and Si3/Al sites in β'' were partially replaced by Zn. As far as we know, no advantages comes out of adding Zn to $6xxx$ alloys. Due to the poor corrosion resistance, this particular study can suggest a maximum of 0.1 wt.% of trace Zn to be kept.

- **Silver:** Being sought after by both electronics manufacturers and posh women, Ag is an expensive metal, and one that is rarely used in commercial alloying of Al [14]. However, it has an excellent solid solubility in Al, only second to that of Zn [14]. Al–Ag alloys are known to form GP-zones during heat treatment [147]. Ag also promotes clustering in $6xxx$ alloys [148] and constitutes the interface layers of the plate-shaped Ω phase in Al–Cu–Mg–Ag alloys [149]. With enough Ag, one can form the β'_{Ag} structure [105]. In paper 5, precipitates in an over-aged Al–Mg–Si–Cu–Ag alloy were investigated. The microstructure consisted of L and Q$'$ particles, which had also been the case if Ag were absent. The effect of Ag is the formation of disordered areas in-

side precipitates, where Ag is present in some atomic columns, often neighbouring each other. There is a high affinity for replacement of Si network columns with Ag, which can be barely seen in Fig. 2(d) in the paper. While Cu wants a triangular symmetry in its columns, Ag is more flexible with its nearby environment. It has been observed e.g. in Si network columns and at Al-fcc sites, which makes its behaviour more comparable to that of Zn. This configurational disagreement causes Cu and Ag to be present in different areas and not share atomic columns. The addition of Ag to Al–Mg–Si(–Cu) alloys leads to a small increase in mechanical strength [150].

These are only a few of the microalloying elements that have been tested experimentally and hypothesised to affect precipitation in Al–Mg–Si alloys [59]. There might still be undiscovered combinations that help the nucleation of known precipitate phases or contribute in forming yet undiscovered phases that strengthen Al–Mg–Si alloys or Al alloys in general. Investigating dense alloys with uncommon ratios of elements is the topic of a new project, see section 4.5.

4.3   Atomic-resolution elemental mapping in STEM

A new top notch microscope, JEOL JEM-ARM200F, was installed at the TEM Gemini Centre in 2013. It comprises both image and probe aberration correctors, DualEELS™ acquisition capabilities [151] and large solid angle EDS detectors, making it one of the best instruments for atomic-resolution elemental analysis in the World. Experiments such as the one described in paper 5 will be conducted regularly on this new instrument. Since STEM–EELS acquisitions take a lot of time (some minutes), they involve many problems, such as beam damage, carbon contamination, and too much drift during acquisition. This comes in addition to the difficulties of aligning and operating the microscope. It will nevertheless open some windows, and in particular make it possible to map the Si signal, which is one of the most troublesome elements due to its L-edge and K-edge being at very low and very high energy loss, respectively [100].

Including all relevant elements in the spectrum is not a problem when instead acquiring STEM–EDS spectrum images, which is the ideal method for measuring all elements except the very lightest ones. ED spectra are easier to analyse than EEL spectra and enables a quite accurate quantification of elemental composition. The downside is a slightly lower resolution and generally longer acquisition times than in STEM–EELS. The optimal configuration would be simultaneous HAADF–STEM, EELS and EDS acquisition,

so one has three datasets and can exploit their individual advantages during data analysis. The three techniques also suffer from electron delocalisation in different ways [152, 153], so such a combination can help to make clearer (and quantify) the effects of delocalisation on the obtained signals.

Atomic-resolution elemental mapping is a quite established technique for investigating e.g. ceramics [154, 155], but has not been used much for metallurgical applications. Paper 5 shows that the technique gives amazing results for precipitates in Al alloys once the challenges related to specimen contamination and microscope stability are overcome. Al–Mg–Si alloys are especially suited due to their needle-shaped precipitates with a homogenous structure through their main growth direction, which enables all atomic columns to be distinguished in the projected needle cross-section. The mapping of columns containing mostly one element, e.g. Cu and Mg were unambiguously identified in the EEL spectrum images. Columns with partial content, in this case of Ag, give a lower signal and are more difficult to map. Rigorous data analysis then becomes important, and PCA was shown in Fig. 3.7 to transform the Ag map from noisy clouds to a nice elemental map showing the position of several Ag-containing columns. With the good results obtained in these initial experiments, the trend is definitely about to change in the favour of more aberration corrected elemental mapping of precipitates in Al alloys.

4.4 Applicability of µSR and PAS to Al alloys

Papers 1 and 2 deal with µSR experiments on Al(–Mg)(–Si) alloys with various heat treatments. The goal of this project was to explore the possibilities of the technique and answer the following questions: What can the technique tell us about the material? What kinds of compositions and microstructural states are required to gain useful information? How does it compare to PAS? Does it help the interpretation of APT/TEM/DSC/XRD data? Can it give us information of interest to the industry? While I can not state with rigor that all questions have been answered to a satisfactory degree, we have laid a foundation that can aid future experiments in discovering properties of materials. A big part of the challenge was understanding the technique itself, how muons behave and how to model this numerically.

The starting motivation was that we wanted to find out something about the vacancy kinetics during low-temperature annealing (e.g. NA) after quenching from SHT. We found quite early that muons are trapped by vacancies at temperatures around RT (300 K). This is proven most conclusively by *in situ* NA studies of pure Al and 1.6% Mg_2Si, both in which the muon

diffusivity increases with time after quenching from SHT [133]. During NA, vacancies are gradually annealed out of the material. The conclusion is an inverse correlation between vacancy content and muon diffusivity, which implies that vacancies attract muons. Although PAS is also sensitive to vacancies, it is more difficult to separate between the different contributions with this technique, and the signal quickly becomes mixed with that of beginning clusters. Therefore, µSR is most sensitive to low vacancy concentrations in Al alloys, unparalleled by any other experimental method. The problem is that we have been unable to answer the sometimes posed question "but how many vacancies are there, exactly?". Quantification requires a more accurate knowledge of muon kinetics than we have at present, specifically a way to predict the muon diffusivity in pure (vacancy-free) aluminium. Muons simply move too fast in such a material, and we are unable to measure it in a way that makes the number distinguishable from infinity. On a side note, µSR is not unique for the ability to probe vacancies. A great accomplishment in solid state science belongs to Simmons and Baluffi, who heated a pure aluminium sample while measuring the physical extension and the lattice parameter with XRD [156]. The deficit in volume change caused by lattice expansion had to be a volume change caused by an increased vacancy concentration. Unfortunately, they were only able to estimate the concentration for temperatures equal to and above typical SHT temperatures for $6xxx$ alloys.

The dense 1.6% Mg_2Si alloy was our base alloy, on which different heat treatment times and temperatures were attempted. Other compositions were also tested, as well as binary 0.5% Si and 0.5% Mg alloys and pure Al. These enabled us to separate the contributions of different muon trapping sites to the total trapping rate. For instance, we determined that Mg atoms in solution provide the most important trapping site at low temperatures (around 30 K). Figure 9 in paper 2 shows an overview of defect contributions.

Al–Mg–Si alloys have a muon trapping peak around 180 K that is not observed in e.g. Al–Mg. Due to its dependence on heat treatment, we associated it with clustering in paper 1. More experiments were conducted, comparing RT stored samples with samples annealed at higher temperatures. According to APT studies [51], Cluster(1) nucleates during RT storage while Cluster(2) is formed during annealing at e.g. 70–100 °C. In light of this and an apparent dependence of Cluster(2) content on muon trapping, we claim in paper 2 that this "good" cluster is an effective muon trapping site. Serizawa *et al.* [51] found that Cluster(2) has a specific (partially ordered) structure. We found a high muon trapping rate in conditions annealed at 70–150 °C, and at the higher end of this temperature range, developed needle-like GP-

zones are clearly visible in a TEM. Since the "cluster trapping peak" appears at quite a high sample temperature (about 180 K), it means the relevant defect is dilute, but has a strong bond with muons. The most probable trapping site is vacancies inside Cluster(2), since solute atoms at fcc positions have a poor trapping potential. Our conclusion is that the "bad" Cluster(1) is disordered while the "good" Cluster(2) has an ordered structure (perhaps resembling that of β'') and is stabilised by absorbing vacancies. In this way, vacancies are caught inside the material until it is aged sufficiently and phases formed later in the precipitation sequence start to dominate. We recently probed a microstructure containing only the stable β phase, and the muon behaviour is very similar to that in annealed Al–Mg, thus devoid of a cluster trapping peak. Research where the alloy composition and heat treatment is varied further from our investigated conditions may help to confirm and elaborate on our conclusion. Specifically, it would be interesting to study Al–Mg–Ge and Al–Mg–Si–Cu alloys with μSR, to probe the early phase formation and identify the differences in kinetics that strongly alters the precipitate microstructures in these systems from that of Al–Mg–Si alloys [40, 157].

It has become clear that positrons are also trapped by solute clusters [48]. *In situ* PAS studies show several clustering stages, and it is easier to probe the early kinetics after quenching with this technique. This might change if a μSR sample holder with the ability to rapidly cool a sample down from SHT temperatures is developed. Confirming our conclusions from μSR with PAS proves difficult. Positron lifetimes can in principle be calculated based on the environment around a positron, but finding the exact nature of clusters is difficult due to a complicated early microstructure with a mixture of many defects that act as positron trapping sites. There is no paper regarding PAS included in this thesis, but a study comparing *in situ* μSR and PALS was published in the conference proceedings for ICAA13 [133]. The paper shows the muon spin relaxation rate and positron lifetime as a function of NA time after quenching. As with μSR, the greatest challenge with PAS is interpreting the measured data. With higher *in situ* data capture rates (better statistics) and a good model for the kinetics of positrons and muons, a greater understanding of early precipitation may be achieved with a similar scheme.

4.5   Personal future plans

My personal plans after graduation involves continuation at the TEM Gemini Centre as a postdoctoral researcher in a FRINATEK project, fully fun-

ded by The Research Council of Norway. The project concerns relations between the precipitation in Al–Mg–Si ($6xxx$), Al–Cu–Mg ($2xxx$) and Al–Zn–Mg ($7xxx$) alloys, and what happens when their alloy compositions are mixed. Specifically, we are interested in the formation enthalpy of the different phases, and which phases will win the battle for solutes. Can e.g. the β'' needles along $\langle 001 \rangle_{\mathrm{Al}}$ (from the $6xxx$ system) coexist with the η' plates along $\{111\}_{\mathrm{Al}}$ planes (from the $7xxx$ system)? How will this influence the mechanical properties? Can the phases of the different systems grow together into joint particles? The $6xxx$ system, to which this thesis is dedicated, is the most complicated of the three, with the highest number of phases and the strangest clustering behaviour, making my work during the previous years a good starting point for this study.

Bibliography

[1] Polmear, I. J., *Light Alloys: Metallurgy of the Light Metals*, Metallurgy and Materials Science Series, Arnold, 1995.

[2] Miller, W. S. et al., Mater. Sci. Eng. A **280** (2000) 37 .

[3] Mukhopadhyay, P., ISRN Metallurgy **2012** (2012).

[4] Polmear, I. J., Mater. Forum **28** (2004).

[5] Dwyer, C., Weyland, M., Chang, L. Y., and Muddle, B. C., Appl. Phys. Lett. **98** (2011) 201909.

[6] Bjørge, R., Andersen, S. J., Marioara, C. D., Etheridge, J., and Holmestad, R., Philos. Mag. **92** (2012) 3983.

[7] Marioara, C. D., Lefebvre, W., Andersen, S. J., and Friis, J., Journal of Materials Science **48** (2013) 3638.

[8] Kehr, K. W. et al., Phys. Rev. B **26** (1982) 567.

[9] Doyama, M. et al., Hyperfine Interactions **17** (1984) 225.

[10] Blundell, S. J., Contemporary Physics **40** (1999) 175.

[11] Wöhler, F., Annalen der Physik und Chemie **11** (1827) 146.

[12] Kittel, C., *Introduction to Solid State Physics*, Wiley, 2004.

[13] Omar, M. A., *Elementary Solid State Physics*, Pearson Education, 1999.

[14] Davis, J. R., editor, *Aluminum and Aluminum Alloys*, ASM Specialty Handbook, ASM International, 1993.

[15] Webelements: the periodic table on the web, http://www.webelements.com.

[16] Trond Furu, private communication.

[17] U.S. Geological Survey, *Minerals Yearbook — Aluminium*, U.S. Geological Survey, 2013.

[18] Görner, H., *Removal of dissolved elements in aluminium by filtration*, PhD thesis, Norwegian University of Science and Technology, Depart-

ment of Materials science and engineering, 2009.

[19] Guthrie, R. I. L. and Nilmani, M., *Impurity Sources and Control – General Principles of Melt Treatment*, The Minerals, Metals & Materials Society, 1993.

[20] Engh, T. A., *Principles of Metal Refining*, Oxford university press, 1992.

[21] Ali, S., Apelian, D., and Mutharasan, R., Canadian Metallurgical Quarterly **24** (1985) 311.

[22] Sigworth, G. K. and Engh, T. A., Metall. Mater. Trans. **28A** (1997) 1281.

[23] Verhoeven, J. D., *Fundamentals of Physical Metallurgy*, John Wiley & Sons, Inc., 1975.

[24] Porter, D. A. and Easterling, K. E., *Phase Transformations in Metals and Alloys*, Chapman & Hall, 2nd edition, 1992.

[25] Hirth, J. P. and Lothe, J., *Theory of dislocations*, John Wiley & sons, 1982.

[26] Buehler, M. J., Hartmaier, A., Duchaineau, M. A., Abraham, F. R., and Gao, H. J., Acta Mechanica Sinica **21** (2005) 103.

[27] Teichmann, K., Marioara, C. D., Andersen, S. J., and Marthinsen, K., Metall. Mater. Trans. A **43** (2012) 4006.

[28] Troeger, L. P. and Jr, E. A. S., Mater. Sci. Eng. A **293** (2000) 19.

[29] Mohanty, P. S. and Gruzleski, J. E., Acta Metall. Mater. **43** (1995) 2001.

[30] Teichmann, K., Marioara, C. D., Andersen, S. J., and Marthinsen, K., Mater. Charact. **75** (2013) 1 .

[31] Wilm, A., Metallurgie **8** (1911) 225.

[32] Duparc, O. H., Zeitschrift für Metallkunde **96** (2005) 398.

[33] Merica, P. D., Waltenberg, R. G., and Scott, H., Scientific Papers of the Bureau of Standards **15** (1919) 271.

[34] Key to metals – The World's most comprehensive metals database, http://www.keytometals.com.

[35] Edwards, G. A., Stiller, K., Dunlop, G. L., and Couper, M. J., Mater. Sci. Forum **217–222** (1996) 713.

[36] Matsuda, K. et al., J. Mater. Sci. **35** (2000) 179.

[37] Andersen, S. J., Marioara, C. D., Frøseth, A., Vissers, R., and Zandbergen, H. W., Mater. Sci. Eng. A **390** (2005) 127 .

[38] Matsuda, K., Ikeno, S., Uetani, Y., and Sato, T., Metall. Mater. Trans. A **32** (2001) 1293.

[39] Chakrabarti, D. and Laughlin, D. E., Progress in Materials Science **49** (2004) 389 .

[40] Marioara, C. D. et al., Philos. Mag. **87** (2007) 3385.

[41] Kovarik, L., Miller, M. K., Court, S., and Mills, M. J., Acta Mater. **54** (2006) 1731 .

[42] Bourgeois, L., Dwyer, C., Weyland, M., Nie, J.-F., and Muddle, B. C., Acta Mater. **59** (2011) 7043 .

[43] Banhart, J. et al., The kinetics of natural ageing in 6000 alloys - a multi-method approach, in *Proceedings of the 12th International Conference on Aluminium Alloys*, pages 381–388, 2010.

[44] Martinsen, F. A., Ehlers, F. J. H., Torsæter, M., and Holmestad, R., Acta Mater. **60** (2012) 6091.

[45] Seyedrezai, H., Grebennikov, D., Mascher, P., and Zurob, H. S., Mater. Sci. Eng. A **525** (2009) 186 .

[46] Kim, J., Kobayashi, E., and Sato, T., Mater. Trans. **52** (2011) 906.

[47] Chang, C. S. T. and Banhart, J., Metall. Mater. Trans. A **42** (2011) 1960.

[48] Banhart, J., Lay, M. D. H., Chang, C. S. T., and Hill, A. J., Phys. Rev. B **83** (2011) 014101.

[49] Seyedrezai, H., Early stages of ageing in Al-Mg-Si alloys, Master's thesis, 2007.

[50] De Geuser, F., Lefebvre, W., and Blavette, D., Philos. Mag. Lett. **86** (2006) 227.

[51] Serizawa, A., Hirosawa, S., and Sato, T., Metall. Mater. Trans. A **39** (2008) 243.

[52] Torsæter, M. et al., J. Appl. Phys. **108** (2010) 073527.

[53] Preston, G., Philos. Mag. **26** (1938) 855.

[54] Marioara, C. D., Andersen, S. J., Jansen, J., and Zandbergen, H. W., Acta Mater. **49** (2001) 321.

[55] van Huis, M. A., Chen, J. H., Zandbergen, H. W., and Sluiter, M. H. F., Acta Mater. **54** (2006) 2945 .

[56] Murayama, M. and Hono, K., Acta Mater. **47** (1999) 1537.

[57] Marioara, C., Andersen, S., Jansen, J., and Zandbergen, H., Acta Mater. **51** (2003) 789.

[58] Chang, C., Wieler, I., Wanderka, N., and Banhart, J., Ultramicroscopy **109** (2009) 585 .

[59] Sato, T., Hirosawa, S., Hirose, K., and Maeguchi, T., Metall. Mater. Trans. A **34** (2003) 2745.

[60] Edwards, G. A., Stiller, K., and Dunlop, G. L., Appl. Surf. Sci. **76-77** (1994) 219.

[61] Andersen, S. J., Met. Mater. Sci. **26A** (1995) 1931.

[62] Zandbergen, H. W., Andersen, S. J., and Jansen, J., Science **277** (1997) 1221.

[63] Hasting, H. S. et al., J. Appl. Phys. **106** (2009) 123527.

[64] Vissers, R. et al., Acta Mater. **55** (2007) 3815.

[65] Ravi, C. and Wolverton, C., Acta Mater. **52** (2004) 4213.

[66] Frøseth, A. G., Høier, R., Derlet, P. M., Andersen, S. J., and Marioara, C. D., Phys. Rev. B **67** (2003) 224106.

[67] Sagalowicz, L., Lapasset, G., and Hug, G., Philos. Mag. Lett. **74** (1996) 57.

[68] Andersen, S., Marioara, C., Vissers, R., Frøseth, A., and Zandbergen, H., Mater. Sci. Eng. A **444** (2007) 157 .

[69] Ehlers, F. J. H., Wenner, S., Andersen, S., Marioara, C. D., and Holmestad, R., The role of the Si network to the stabilization of hardening precipitates in the Al–Mg–Si(–Cu) alloy system, in *13th International Conference on Aluminum Alloys*, edited by Heiland, W., Rollett, A. D., and Cassada, W., pages 279–284, Wiley, 2012.

[70] Ehlers, F. J. H., Wenner, S., Andersen, S. J., Marioara, C. D., and Holmestad, R., Phase stabilization principle and precipitate-host lattice influences for Al–Mg–Si–Cu alloy precipitates, (submitted to Acta Mater.).

[71] Chen, J. H., Costan, E., van Huis, M. A., Xu, Q., and Zandbergen, H. W., Science **312** (2006) 416.

[72] Derlet, P. M., Andersen, S. J., Marioara, C. D., and Frøseth, A., J. Phys.: Condens. Mat. **14** (2002) 4011.

[73] Andersen, S. J. et al., Acta Mater. **46** (1998) 3283 .

[74] Dumolt, S. D., Laughlin, D. E., and Williams, J. C., Scripta Metall. **18** (1984) 1347 .

[75] Jacobs, M. H., Philos. Mag. **26** (1972) 1.

[76] Cayron, C., Sagalowicz, L., Beffort, O., and Buffat, P. A., Philos.

Mag. A **79** (1999) 2833.

[77] Torsæter, M., Ehlers, F. J. H., Marioara, C. D., Andersen, S. J., and Holmestad, R., Philos. Mag. **92** (2012) 3833.

[78] Sagalowicz, L., Hug, G., Bechet, D., Sainfor, P., and Lapasset, G., A study of the structural precipitation in the Al-Mg-Si-Cu system, in *4th International Conference on Aluminium Alloys*, edited by Sanders, T. H. and Starke, E. A., pages 636–643, 1994.

[79] Arnberg, L. and Aurivillius, B., Acta Chem. Scand. **34A** (1980) 1.

[80] Wolverton, C., Acta Mater. **49** (2001) 3129 .

[81] Nordström, A., TEM studies of the equilibrium phase in Al-Mg-Si(-Cu) alloys, Master's thesis, 2006.

[82] Marioara, C. D., Andersen, S. J., Birkeland, A., and Holmestad, R., J. Mater. Sci. **43** (2008) 4962.

[83] Ratke, L. and Voorhees, P. W., *Growth and Coarsening: Ostwald Ripening in Material Processing*, Engineering Materials and Processes, Springer, 2002.

[84] Liu, M., unpublished results.

[85] Granholt, J. D. D. A., Precipitate structure changes during overaging in an Al-Mg-Si alloy, Master's thesis, 2012.

[86] Egerton, R. F., Reports on Progress in Physics **72** (2009) 016502.

[87] Hetherington, C., Materials Today **7** (2004) 50 .

[88] Batson, P. E., Dellby, N., and Krivanek, O. L., Nature **418** (2002) 617.

[89] Urban, K. W. et al., Philos. T. R. Soc. A **367** (2009) 3735.

[90] Williams, D. and Carter, C., *Transmission Electron Microscopy: A Textbook for Materials Science*, Cambridge library collection, Springer, 2009.

[91] Humphreys, C. J., Rep. Prog. Phys. **42** (1979) 1825.

[92] Rose, H., Ultramicroscopy **110** (2010) 488 .

[93] Yamazaki, T., Kawasaki, M., Watanabe, K., Hashimoto, I., and Shiojiri, M., Ultramicroscopy **92** (2002) 181 .

[94] Ayer, R., Journal of Electron Microscopy Technique **13** (1989) 16.

[95] Nellist, P. D. and Pennycook, S. J., The principles and interpretation of annular dark-field Z-contrast imaging, in *Advances in Imaging and Electron Physics*, edited by Kazan, B., Mulvey, T., and Hawkes, P., volume 113, pages 147–203, Elsevier, 2000.

[96] Pennycook, S. J., Structure determination through Z-contrast microscopy, in *Microscopy, Spectroscopy, Holography and Crystallography with Electrons*, edited by Peter W. Hawkes, Pier Georgio Merli, G. C. and Vittori-Antisari, M., volume 123 of *Advances in Imaging and Electron Physics*, pages 173 – 206, Elsevier, 2002.

[97] Deininger, C., Necker, G., and Mayer, J., Ultramicroscopy **54** (1994) 15.

[98] Kimoto, K., Kothleitner, G., Grogger, W., Matsui, Y., and Hofer, F., Micron **36** (2005) 185 .

[99] Stockli, T., Bonard, J. M., Stadelmann, P.-A., and Châtelain, A., Zeitschrift für Physik D **40** (1997) 425.

[100] Ahn, C. C. and Krivanek, O. L., *EELS Atlas*, Arizona State University and Gatan Inc., Tempe, AZ, 1983.

[101] Malis, T., Cheng, S. C., and Egerton, R. F., J. Elec. Microsc. Tech. **8** (1988) 193.

[102] Bjerkaas, H., *Characterisation and Plasticity in Extruded Al-Mg-Si Profiles engaging In-situ EBSD*, PhD thesis, Norwegian University of Science and Technology, Department of Materials science and engineering, 2007.

[103] Reimer, L. and Kohl, H., *Transmission Electron Microscopy – Physics of Image Formation*, Springer, 2008.

[104] Marioara, C. D., Andersen, S. J., Zandbergen, H., and Holmestad, R., Metall. Mater. Trans. A **36** (2005) 691, 10.1007/s11661-005-0185-1.

[105] Marioara, C. D. et al., Philos. Mag. **92** (2012) 1149.

[106] Bjørge, R. et al., J. Phys. Conf. Ser. **371** (2012) 012015.

[107] Goodhew, P. and Bleloch, A., Materials World **11** (2003) 23 .

[108] Williams Lefebvre, private communication.

[109] Keenan, M. R. and Kotula, P. G., Microscopy and Microanalysis **10** (2004) 874.

[110] Arenal, R. et al., Ultramicroscopy **109** (2008) 32 .

[111] Goldstein, J. et al., *Scanning Electron Microscopy and X-ray Microanalysis*, Springer, 3rd ed. edition, 2003.

[112] Echlin, P., *Handbook of Sample Preparation for Scanning Electron Microscopy and X-Ray Microanalysis*, Spinger, 2009.

[113] Yamazaki, T., Hyperfine Interactions **6** (1979) 115.

[114] Gladisch, M. et al., Hyperfine Interactions **6** (1979) 109.

[115] Borghini, M. et al., Phys. Rev. Lett. **40** (1978) 1723.

[116] Boekema, C. et al., Phys. Rev. B **26** (1982) 2341.

[117] Nagamine, K., Pratt, F. L., Watanabe, I., and Torikai, E., RIKEN Review **35** (2001) 126.

[118] Lichti, R. L., Chow, K. H., and Cox, S. F. J., Phys. Rev. Lett. **101** (2008) 136403.

[119] Saragi, T. P. et al., Organic Electronics **14** (2013) 62 .

[120] Garwin, R. L., Lederman, L. M., and Weinrich, M., Phys. Rev. **105** (1957) 1415.

[121] Yaouanc, A. and De Réotier, P. D., *Muon Spin Rotation, Relaxation, and Resonance: Applications to Condensed Matter*, International Series of Monographs on Physics, Oxford University Press, 2011.

[122] Coughlan, G., Dodd, J., and Gripaios, B., *The Ideas of Particle Physics: An Introduction for Scientists*, Cambridge University Press, 2006.

[123] Webber, D. M. et al., Phys. Rev. Lett. **106** (2011) 041803.

[124] Hayano, R. S. et al., Phys. Rev. B **20** (1979) 850.

[125] van der Vaart, A. W., *Asymptotic Statistics*, Cambridge Series in Statistical and Probabilistic Mathematics, Cambridge University Press, 2000.

[126] Kubo, R. and Toyabe, T., in *Magnetic Resonance and Relaxation*, edited by Blinc, R., page 810, North-Holland, Amsterdam, 1967.

[127] Holzschuh, E. and Meier, P. F., Phys. Rev. B **29** (1984) 1129.

[128] Matsuzaki, T. et al., Nuclear Instruments and Methods A **465** (2001) 365.

[129] Isis – about isis, http://www.isis.stfc.ac.uk/about-isis/.

[130] Doyama, M., Nakai, R., and Yamamoto, R., Hyperfine Interactions **17** (1984) 231.

[131] Hartmann, O. et al., Phys. Rev. Lett. **44** (1980) 337.

[132] Prochazka, I., Materials structure **8** (2001) 55.

[133] Wenner, S. et al., Muon spin relaxation and positron annihilation spectroscopy studies of natural ageing in Al–Mg–Si alloys, in *13th International Conference on Aluminum Alloys*, edited by Heiland, W., Rollett, A. D., and Cassada, W., pages 37–42, Wiley, 2012.

[134] Dlubek, G., Mater. Sci. Forum **13–14** (1987) 11.

[135] Ferragut, R. et al., Scripta Mater. **60** (2009) 137.

[136] Li, Y. J. and Arnberg, L., Acta Mater. **51** (2003) 3415 .

[137] Jansen, J., Tang, D., Zandbergen, H. W., and Schenk, H., Acta Cryst. **A54** (1998) 91.

[138] Miller, M. K. and Kenik, E. A., Microscopy and Microanalysis **10** (2004) 336.

[139] Varschavsky, A. and Donoso, E., Journal of Thermal Analysis and Calorimetry **74** (2003) 41.

[140] De Moor, E., Föjer, C., Penning, J., Clarke, A. J., and Speer, J. G., Phys. Rev. B **82** (2010) 104210.

[141] Zhen, L. and Kang, S. B., Materials Letters **37** (1998) 349.

[142] Hohenberg, P. and Kohn, W., Phys. Rev. **136** (1964) B864.

[143] Kohn, W. and Sham, L. J., Phys. Rev. **140** (1965) A1133.

[144] Torsæter, M., *Quantitative studies of clustering and precipitation in Al–Mg–Si(–Cu) alloys*, PhD thesis, Norwegian University of Science and Technology, Department of Physics, 2011.

[145] Saito, T. et al., Metall. Mater. Trans. A **44** (2013) 4124.

[146] Saito, T. et al., The effect of zn on precipitation in Al-Mg-Si alloys, (submitted to Philos. Mag.).

[147] Alexander, K. B., Legoues, F. K., Aaronson, H. I., and Laughlin, D. E., Acta Metall. **32** (1984) 2241.

[148] Kim, J., Tezuka, H., Kobayashi, E., and Sato, T., Korean J. Mater. Res. **22** (2012) 31.

[149] Hutchinson, C. R., Fan, X., Pennycook, S. J., and Shiflet, G. J., Acta Mater. **49** (2001) 2827 .

[150] Kim, J., Marioara, C. D., Holmestad, R., Kobayashi, E., and Sato, T., Mater. Sci. Eng. A **560** (2013) 154 .

[151] Gubbens, A. et al., Ultramicroscopy **110** (2010) 962 .

[152] Rossell, M. D. et al., ACS Nano **6** (2012) 7077.

[153] Suenaga, K., Okazaki, T., Okunishi, E., and Matsumura, S., Nature Photonics **6** (2012) 545.

[154] Tan, H., Turner, S., Yücelen, E., Verbeeck, J., and Van Tendeloo, G., Phys. Rev. Lett. **107** (2011) 107602.

[155] MacLaren, I. et al., Adv. Funct. Mater. **23** (2013) 683.

[156] Simmons, R. O. and Balluffi, R. W., Phys. Rev. **117** (1960) 52.

[157] Bjørge, R., Marioara, C. D., Andersen, S. J., and Holmestad, R., Metall. Mater. Trans. A **41** (2010) 1907.